Holographic Revivals

Memoria de Tesis Doctoral realizada por

Emilia da Silva di Tommaso

y presentada ante el Departamento de Física Teórica
de la Universidad Autónoma de Madrid
para la obtención del Título de Doctor en Física Teórica

Tesis Doctoral dirigida por la Dra. **Esperanza López Manzanares,**
Investigador Científico del Instituto de Física Teórica UAM/CSIC

Departamento de Física Teórica
Universidad Autónoma de Madrid

Instituto de Física Teórica
UAM/CSIC

Marzo 2017

Resumen

En esta tesis hemos estudiado holográficamente la dinámica de fuera de equilibrio de tres sistemas de teoría cuántica de campos a acoplo fuerte.

En dos de ellos, la teora cuántica vivía en un espacio compacto de 1+1 y 2+1 dimensiones, respectivamente. Para modelizar holográficamente estos sistemas, hemos estudiado la formación de agujeros negros clásicos en dos espacios asintóticamente AdS, en 2+1 y 3+1 dimensiones respectivamente, acoplados a un campo escalar sin masa. El observable que monitorizamos en ambas dimensiones fue la entropía de entrelazamiento holográfica. Cuando el campo escalar sin masa tiene suficiente energía forma directamente un agujero negro, cuando la disminuimos, se producen oscilaciones en la geometría. El resultado principal de esta parte de la tesis, consiste en haber relacionado estas oscilaciones, con reconstrucciones parciales del estado inicial en la teoría cuántica dual. En algunos casos específicos, conseguimos relacionar el patrón de esta reconstrucción de estados con el modelo de propagación de entrelazamiento cuántico propuesto por Cardy y Calabrese en [1]. Además, conseguimos simular numéricamente la evolución de la métrica, en el sistema gravitatorio asintóticamente AdS_4, más allá de la primera aparición del horizonte aparente, llegando incluso a ver la formación del agujero negro con toda la masa disponible en el sistema. Este resultado, junto a las diferencias destacables que encontramos entre perfiles del campo escalar anchos y estrechos, nos permitió identificar procesos distintos de aproximación al equilibrio en la teoría cuántica dual. Por otro lado, la identificación de las magnitudes t_{rev}, el tiempo al que la EE recuperaba su valor inicial, y t_{deph}, el tiempo al que la EE alcanzaba su valor térmico, posiblitó relacionar la fenomenología que encontramos holográficamente con algunos sistemas cuánticos conocidos. Además, el haber trabajado dos sistemas similares en dimensionalidades distintas, nos abrió la puerta a realizar una

comparación de las distintas formas de aproximación al equilibrio en estos dos casos, permitiéndonos relacionar algunos aspectos con el distinto grupo de simetrías de las teorías conformes en 1+1 y 2+1 dimensiones.

El tercer sistema que estudiamos holográficamente en esta tesis, fue un sistema de campos cuánticos a acoplo fuerte con un "mass gap", que vivía en un espacio no compacto de 1+1 dimensiones. Para modelizar gravitatoriamente este sistema, utilizamos un espacio-tiempo asintóticamente AdS_3, acoplado a un campo escalar sin masa, y con una pared rígida. La presencia de esta pared en el sistema, nos permitió obtener fácilmente reconstrucciones del estado inicial en la teoría dual. Además, posibilitó la modelización de nuevos "quenches" en la teoría dual con los que observamos un intercambio de energía entre el campo escalar sin masa y la pared rígida, manteniéndose la energía total del sistema constante. El estudio de estos "quenches", nos llevó a realizar una comparación cualitativa con el modelo de Schwinger masivo estudiado en [2]. Usando esta comparación, conseguimos relacionar cualitativamente determinadas métricas concretas con estados específicos de la teoría cuántica dual.

Contents

Chapter 1

Introduction

The study of the out of equilibrium dynamics of quantum system is a very interesting topic where, still, open questions are posed both from the experimental and the theoretical framework. In this thesis our aim is to try to give a step forward in this understanding by using the AdS/CFT correspondence [3].

From a classical perspective, interest in this topic mainly started with the seminal work of Fermi, Pasta and Ulam (FPU) on the dynamics of a one-dimensional anharmonic chain [4]. Fermi expected that the non linearities of the system were going to be enough to reach an statistical behavior at long times. But this was not what they found. What they found was the starting point of two new branches of classical dynamics: integrability and chaos.

Even after this work and on generic grounds, we may intuitively expect that, for isolated quantum systems, a fast approach to ergodic behavior should be found. However, a rich variety of situations where this is not the the case are known [5]. For example, from the theoretical perspective, it was shown in [6] how conservation laws of integrable theories constrain the final state to be different from that prescribed by the canonical ensemble. In some other systems, metastable intermediary states which retain memory of the initial excitation were found, and are usually called pre-thermalization plateaux in the literature [7, 8]. A statistical derivation for these states by using a generalized Gibbs ensemble have been studied in [9, 6, 10, 11, 12].

Among all this phenomenology we find in out of equilibrium systems, we are mainly interested in revivals: sometimes a system, initially out of equilibrium, evolves towards an apparently decohered state which, after some time, shows a partial (or total) reconstruction. Usually, when a revival occurs it does not happen isolated, it

repeats itself with or without decay [13, 14, 15, 16]. The holographic reproduction of revivals under different circumstances is the main result of this thesis.

A particular case of these revivals was studied in [2] with tensor network procedures. Although this kind of techniques have usually been applied to the study of ground states properties [17], recently they have also been used to describe real time evolution. This gave us the possibility of making a qualitative comparison with our holographic results by using the model studied in [2], where an analysis of the massive Schwinger response to a quench was addressed, and, at low energies, revivals were found.

The AdS/CFT correspondence, which is the method we used to model some of these out of equilibrium phenomena, relates a classical gravity theory with a QFT at large N and strong coupling [3, 18]. We know that a black hole in an asymptotically AdS spacetime represents a thermal state in the corresponding QFT, therefore, it is natural to propose the dynamical formation of a black hole as dual to the equilibration process in the QFT theory [19, 20]. However, in this thesis we originally tried to build holographic models whose out of equilibrium dynamics departs from a fast approach to ergodic behavior. We managed to find these geometries and we studied them in two cases: a CFT living in two spacetimes with different dimensionality ($S^2 \times R$ and $S \times R$) [21, 22], and a QFT with a mass gap living in $R_{(1,1)}$ [23].

To model the isolated quantum systems in $S^2 \times R$ and $S \times R$, we basically used the gravity model described in [24] and analyzed it in $3+1$ and, also, $2+1$ dimensions. This model involves a massless scalar field coupled to Einstein gravity with negative cosmological constant. A very interesting feature of this system is that, for certain initial conditions, there is a periodic regime where the scalar field bounces back and forth between the origin and the boundary before forming a horizon. We will propose that, under some constrains, these bounces are dual to revivals in the QFT. However, the landscape of solutions is much richer [25, 26, 27, 28, 29, 30, 31, 32, 33, 34], and, for example, we studied some regular solutions which seem to be stable and never collapse to a black hole [31, 32, 33]. All this landscape (which mainly depends on the initial conditions) is related in this thesis to the variety of relaxation process that are observed in quantum isolated systems.

To model a non compact gapped system in $1+1$ dimensions, we had to modify

the previous system following [35, 36], where an infrared hard wall was introduced in the geometry to model the gap. In our analysis, we realized that a mass could be assigned to this wall affecting the infrared physics of the dual theory. This mass, allowed us to have, in the dual side, a whole new family of QFT among which we holographically moved performing a quench in the hamiltonian. Besides, we qualitatively compared our holographical results, with the ones obtained with tensor network methods in [2], where the massive Schwinger model was studied.

The holographic observable that we monitored in our gravity setups is the entanglement entropy S_A of a region A in the QFT space. It was conjectured in [37], and recently put on firmer grounds in [38, 39, 40], to be given by the area of a minimal surface γ_A which extends into the bulk and is homologous to A:

$$S_A = \frac{\text{Area}(\gamma_A)}{4G_N} \tag{1.1}$$

For non-static backgrounds, as is our case, the condition of minimal surface has to be replaced by that of an extremal one [41]. However, we will see how in the hard wall model we were forced to replace this standard condition to compute the EE by a slightly modified one.

This thesis is organized in the following way. Chapter 2 is a basic introduction to the AdS/CFT correspondence focusing on explaining the items that are used in the following sections. Chapter 3 is also an introductory part but in this case to the entanglement entropy, the main observable we will use during this thesis. In this chapter we will explain some very basic concepts in the framework of quantum mechanics, and then we will move to an explanation of the results obtained by Cardy and Calabrese in [1] about propagation of entanglement after a quench. To finish with this chapter the holographic way of computing the EE is explained in detail. With the next two chapters starts the presentation of new results which were obtained during the realization of this thesis. Chapter 4 is an analysis of the holographic models of isolated quantum systems living in a sphere $S^2 \times R$ and a circle $S^1 \times R$. In the first section of this chapter, these two cases are studied and compared for different initial conditions, the second section is a QFT interpretation of these dynamics which is mainly supported by the last section, where an analysis of the EE results is given. Chapter 5 shows the results obtained for the other holographic model we studied, namely, an infinite spacetime in $1+1$ dimensions with a mass gap. As before, the first section is an explanation of the hard wall geometry while the next one is an

analysis of the two main observables we use in this chapter (the correlation length, defined through the EE, and the mass gap). In the third section we explain how to perform a quench acting in the hard wall and how it affects the system evolution. In the last chapter, the connection with the Schwinger model of [2] allowed us to develop the QFT interpretation of these gravitational dynamics.

Chapter 2

AdS/CFT

The AdS/CFT duality is an equivalence, under some conditions, between a gravitational theory in $d+1$ dimensions and a quantum gauge theory without gravity in d dimensions. Polyakov had already suggested this idea in [42, 43]. But it was not until the work of Juan Maldacena [3] in the string theory context, that the AdS/CFT correspondence was stablished. Some months after this work, an explicit way to compute observables on this new correspondence was presented in [18, 44]. This was almost twenty years ago, and, since then, AdS/CFT has evolved in many different directions. Here, we will focus on its more phenomenological aspects rather than in its string theory origin. We will present the tools this duality give us and, by using them, we will arrive, in the following sections, to deep connections between the geometry of spacetime and quantum entanglement.

What makes this duality something really important and useful is the theories it connects and they way it does it. In one of its limits, roughly speaking, this duality clames:

Large N and Strongly coupled D dimensional field theory

=

Classical gravitational theory in D+1 dimensional AdS spacetime

Where we connect a QFT at strong coupling and large N, with a classical gravitational theory that we solve by finding solutions to the Einstein equations. This is the approach we take in this thesis: we use the AdS/CFT duality to map a QFT problem that we do not how to solve, to a classical gravity problem that we can solve. Besides, by making this connection, we managed to understand new theoretical features of how the duality works.

Although we are not going to work on it in this thesis, it is important to comment

that the reverse limit, the one where the gravity is quantum and the QFT is at weak coupling, offers a way to define and compute observables in a Quantum Theory of Gravity.

In the original works the duality was studied in a very specific case where the connection was done between N=4 SU(N) Yang Mills living in a 4 dimensional spacetime, and a specific string theory model living in an $AdS_5 \times S^5$ spacetime. The analogous limit of the one we have just posed, would be:

$$\begin{gathered}\text{Large } \lambda = g_{YM}^2 N \text{ limit of the N=4 SYM (for } N \to \infty) \\ = \\ \text{Classical type IIB supergravity living in } AdS_5 \times S^5\end{gathered}$$

Notice that by performing a Kaluza Klein reduction on the compact S^5 we obtain a particular case of the previous general statement of the duality.
This QFT, besides being supersymmetric, is also a conformal field theory. This is a very important statement that, in fact, gives name to the duality: while AdS stands for Anti de Sitter spacetime, CFT refers to the symmetries of the QFT.[1]

In this set up E. Witten made a proposal for the partition functions of both theories: they should coincide in all limits, namely $Z_{string} = Z_{gauge}$. Besides, in the limit stated above we can approximate Z_{string} by $e^{-I_{SUGRA}}$:

$$e^{-I_{SUGRA}} \approx Z_{string} = Z_{gauge} = e^{-W} \tag{2.1}$$

Where, as corresponds with the limit where the QFT is at strong coupling and large N, we have approximated the string theory partition function with the supergravity one. In this formula, W is the generating functional for connected Green's functions in the gauge theory.

The extra dimension that we have in the gravity side is called the holographic direction and, in the QFT side, represents the running of some scale that in this thesis we relate with entanglement. See Figure(2.1) for a schematic picture of the understanding of this extra dimension in the QFT spacetime.

[1] It can be shown that the global symmetries of both theories coincide.

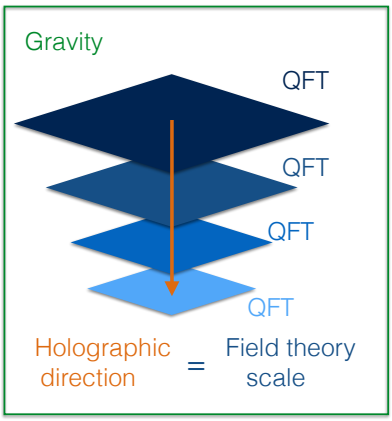

Figure 2.1: Schematic view of the holographic direction in the QFT side.

2.1 AdS spacetime

Let us define the AdS_{p+2} spacetime as the hyperboloid[45]:

$$x_0^2 + x_{p+2}^2 - \sum_{i=1}^{p+1} x_i^2 = R^2 \tag{2.2}$$

in a flat spacetime of dimension $(p+3)$ and a metric with two timelike directions:

$$ds^2 = -dx_0^2 - dx_{p+2}^2 + \sum_{i=1}^{p+1} x_i^2 \tag{2.3}$$

Notice that, by construction, this spacetime has the isometry $SO(2, p+1)$ and is isotropic and homogeneous. To obtain its metric we just have to solve Eq(2.2) and plug the result in the metric of the total spacetime (Eq(2.3)). We can do it by setting:

$$x_0 = R\cosh\rho\cos\tau; \qquad x_{p+2} = R\cosh\rho\sin\tau; \qquad x_i = R\sinh\Omega_i\rho \tag{2.4}$$

where $i = 1, \ldots, p+1$ and $\sum_i \Omega_i^2 = 1$. Then, we have to substitute in Eq(2.3), obtaining the result:

$$ds^2 = R^2(-\cosh^2\rho d\tau^2 + d\rho^2 + \sinh^2\rho d\Omega_p^2) \tag{2.5}$$

We still have to set the intervals in which the coordinates (ρ, τ) are defined. The first natural choice would be to set the coordinates in a way that they cover the whole hyperboloid just once. These are called **global coordinates** and correspond to choose $0 \leq \rho$ and $0 \leq \tau < 2\pi$. Nevertheless, notice that this hyperboloid has the topology of $S^1 \times R^{p+1}$, where S^1 represents closed timelike curves in the τ direction. To avoid

this and to obtain a causal spacetime we can unwrap S^1 by taking $\tau \in R$ without any identification. This defines the universal covering of the hyperboloid which has no closed timelike curves. In this thesis when we refer to the AdS_{p+2} spacetime we will be always referring to its universal covering.

In the AdS/CFT correspondence the conformal boundary of the AdS space is the

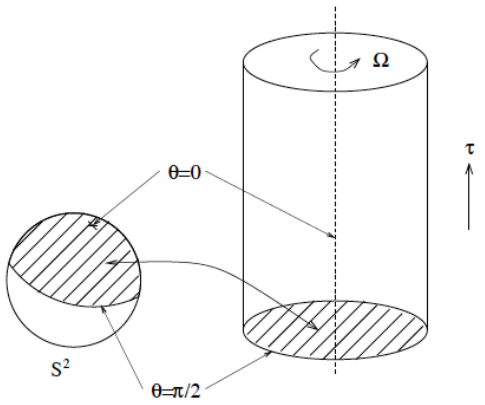

Figure 2.2: Conformal mapping from AdS_3 to half of the Einstein static universe with topology $R \times S^2$. Extracted from [3].

spacetime where the QFT lives. In the last chapter, the fact that the QFT will be living in a compact space rather than in an infinite one, will be crucial. Therefore, to see explicitly the topology of the conformal boundary, we make a change of coordinates where we introduce only one new coordinate θ , that is related with the old coordinate ρ , by $\tan\theta = \sinh\rho$ where $0 \leq \theta \leq \pi/2$. After this change the metric takes the form:

$$ds^2 = \frac{R^2}{\cos^2\theta}\left(-d\tau^2 + d\theta^2 + \sin^2\theta d{\Omega_p}^2\right) \tag{2.6}$$

By doing a conformal rescaling (in Figure(2.2) we show a scheme of this mapping) we obtain:

$$ds^2 = -d\tau^2 + d\theta^2 + \sin^2\theta d{\Omega_p}^2 \tag{2.7}$$

Which is half of the metric of the Einstein static universe (half because $0 \leq \theta < \pi/2$ and not $0 \leq \theta < \pi$). The boundary of this space is placed at $\theta \to \pi/2$ and its topology is $S^p \times R$ where R is the timelike direction. Therefore, the topology of the QFT spacetime is $S^p \times R$, namely, the quantum theory lives in a sphere of p dimensions and evolves in time.

Many applications of the AdS/CFT correspondence, and in particular the one that we use in this thesis, do not deal with pure AdS spacetime but with spacetimes that are **asymptotically AdS**. An spacetime is asymtotically AdS if we can conformally compactify it into a region which has the boundary structure of one half of the Einstein static universe.

Notice that, as the boundary extends in the timelike direction τ (this is clearly seen in Figure(2.2)), when we put a particle, or a field, in this spacetime, we need to specify a boundary condition on $R\times S^p$ at $\theta = \pi/2$ to define properly the Cauchy problem.

Besides the global coordinates, we can also define a set of coordinates $(u, t, \vec{x})$, where $u > 0$ and $\vec{x} \in R^p$, that cover only half of the hyperboloid. As before we have to

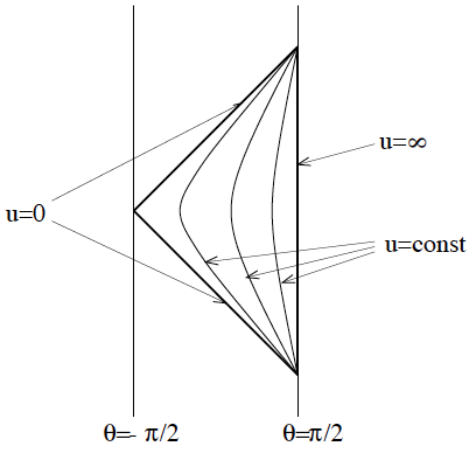

Figure 2.3: In this scheme we can see the relation in AdS_2 between the global coordinate θ and the Poincare coordiante u. Notice that the region covered by Poincare coordinates is half of the region covered by global coordinates. Extracted from [3].

solve Eq(2.2), the result is:

$$\begin{aligned} x_0 &= \frac{1}{2u}\left(1 + u^2\left(R^2 + \vec{x}^2 - t^2\right)\right), \qquad & x_{p+2} &= Rut \\ x_{p+1} &= \frac{1}{2u}\left(1 - u^2\left(R^2 - \vec{x}^2 + t^2\right)\right), \qquad & x_i &= Rux_i \end{aligned} \tag{2.8}$$

And if we substitute in the metric of the spacetime that contains the hyperboloid, we obtain another form of the metric of AdS:

$$ds^2 = R^2\left(\frac{du^2}{u^2} + u^2\left(-dt^2 + d\vec{x}\right)\right) \tag{2.9}$$

These are called **Poincaré coordinates**. In Figure(2.3) and for the case $p = 0$, namely AdS_2, we explicitly see how this coordinates do not cover the whole hyperboloid.
Notice that the conformal boundary for the Poincaré patch of AdS_{n+2} has the topology of $\mathcal{R}^p$ (see Eq(2.9)). Namely, when we work in these coordinates, the dual QFT lives in a non compact spacetime.

2.2 Field-operator correspondence

In a CFT there is no scale and, therefore, neither asymptotic states nor a S-matrix. That is why the field-operator correspondence we are going to explain is so powerful, because in this kind of theories the natural objects to consider are operators.
This correspondence between fields in the AdS spacetime and operators in the QFT side, states that each field propagating on AdS spacetime is in a one to one correspondence with an operator in the field theory. Besides, there is a relation between the mass of this field and the scaling dimensions of the operator in the quantum theory[45].

Although we may need some notions of string theory, let us try to give some intuition about this relation using a particular case:
In N=4 SYM there is a deformation by a marginal operator that changes the value of the coupling constant. In the AdS/CFT duality the coupling constant of the QFT is related to the string coupling, whose value is also connected to the expectation value of the dilaton (the scalar field that appears in the supergravity action). This expectation value is determined by the boundary condition for the dilaton at the boundary of AdS. Therefore, a deformation by a marginal operator in the QFT implies a change in the boundary value of the scalar field. This is the expected result the field-operator correspondence would have given us.
Let us pose this in formulas. We call the corresponding marginal operator O and, for simplicity, we consider that this operator was not present in the original lagrangian[2]. The deformation that we just described would correspond to add to this lagrangian the term $\int d^4x\phi_0(\vec{x})O(\vec{x})$. From the previous discussion we know that this deformation changes the value of the scalar field at the boundary of the AdS spacetime, namely $\phi(\vec{x},z)|_{z=0} = \phi_0(\vec{x})$. At this point we could propose the following relation:

$$\langle e^{\int d^4x\phi_o(x)O(x)}\rangle_{CFT} = Z_{string}\left(\phi(\vec{x},z)|_{z=0} = \phi_0(\vec{x})\right) \tag{2.10}$$

[2]If we consider that O was actually present in the original lagrangian, we just have to set $\phi_0(\vec{x})$ as the total coefficient of the operator.

Notice that this is just a way of rewriting Formula(2.1) in a particular case, where we make explicit the relation between a scalar field propagating in AdS spacetime and a marginal operator in the CFT. As before, the right hand side is the partition function of the string theory, where $\phi_0(\vec{x})$ is an arbitrary function that has been chosen as a boundary condition for the scalar field.
What the field-operator correspondence tell us is that this equality is a general result for all fields propagating in AdS. A very important consequence of this formula is that with it, we know how to calculate correlations functions of O: we just have to take functional derivatives with respect to ϕ_0 and then set $\phi_0 = 0$ in the right side part of the previous equation (using the SUGRA approximation).

With the previous discussion, we have given an heuristic origin to the field-operator correspondence. Nevertheless, we can still give more intuition about it if we work with a particular example where we can see, explicitly, the relation between the mass of the propagating field and the dimension of the corresponding operator in the CFT. To do it, let us take example as an example a massive scalar field propagating in AdS_{d+1}. The wave equation for the field is:

$$\left(\Delta - m^2\right)\phi = 0 \tag{2.11}$$

There are two independent solutions, namely two modes, that behave differently in the boundary of AdS. One of them goes like $\phi \sim z^{d-\Delta}$ and the other like $\phi \sim z^{\Delta}$, where

$$\Delta = \frac{d}{2} + \sqrt{\frac{d^2}{4} + R^2 m^2} \tag{2.12}$$

Therefore, the one that is proportional to z^{Δ} is always normalizable and the other one, that goes with $z^{d-\Delta}$, may or may not be normalizable depending on the value of the mass. Although the computation is not going to be reproduced here, it is important to know that, while the value of the normalizable mode of the scalar field at the boundary gives the expectation value of the corresponding operator, the non normalizable mode acts as a source.

To show the relation between the mass of the scalar field and the dimension of the operator, we will focus on the non normalizable mode. To avoid its divergence at the boundary (that in these coordinates is at $z = 0$), we have to introduce a cutoff ϵ by redefining the boundary condition on the field in the right hand side of Eq(2.10).

Explicitly, we have to change the previous equality by :

$$\langle e^{\int d^4x \phi_o(x) O(x)} \rangle_{CFT} = Z_{string} \left(\lim_{\epsilon \to 0} \left(\phi(\vec{x}, \epsilon) = \epsilon^{d-\Delta} \phi_0(\vec{x}) \right) \right) \tag{2.13}$$

Notice that as $\phi(\vec{x}, t)$ is dimensionless and ϵ has dimensions of length, ϕ_0 has dimensions of length$^{\Delta - d}$. With this information and the exponent of the right hand side of the last equation, we see that the operator O has dimension Δ. As Δ depends on the mass m of the scalar field, we have found the kind of relation we were expecting.

2.3 Thermal State and Black Holes

Although we have not said it explicitly, in the AdS/CFT correspondece a state in the QFT side is mapped to a particular geometry in the gravity part[3]. Pure AdS space, the spacetime described in the previous section, corresponds to the vacuum of the CFT. In this section we will study AdS black holes. The dual state of this kind of geometries is a thermal state [46][4].

First, let us explain some features of these geometries. The metric is given by[47]:

$$ds^2 = -V_\kappa(r) dt^2 + \frac{dr^2}{V_\kappa(r)} + \frac{r^2}{l^2} dK_{n-1}^2 \tag{2.14}$$

where the dimension of the spacetime is $n+1$, l is the AdS curvature length related to the cosmological constant, dK_n is:

$$dK_n^2 = \frac{d\chi^2}{1 - \kappa\chi^2} + \chi^2 d\Omega_{n-1}^2 \tag{2.15}$$

And V_κ is defined as a function of the parameter κ and μ (which is a constant that depends on the black hole mass):

$$V_\kappa = \kappa - \frac{\mu}{r^{n-2}} + \frac{r^2}{l^2} \tag{2.16}$$

In the AdS case κ can take the three values[5] $(-1, 0, 1)$. The metric obtained with the value $\kappa = 1$, reduces to the usual Schwarzschild solution when we take the limit

[3] In the time dependent case a geometry corresponds to a state and its whole time evolution.

[4] This is not actually true, only eternal large black holes, that will be defined in the following, are dual to thermal states.

[5] Notice that for the case $\kappa = 1$, dK_n is the metric of Minkowski spacetime in spherical coordinates, for $\kappa = (1, -1)$ we respectively have the line element for the unit sphere and hyperboloid:

$$\begin{array}{llll} dK_n(\kappa = 1) = d\phi^2 + \sin^2\phi d\Omega_{n-1}^2, & \phi \in [0, \pi), & \chi = \sin\phi \\ dK_n(\kappa = -1) = d\psi^2 + \sinh^2\psi d\Omega_{n-1}^2, & \psi \in [0, \infty), & \chi = \sinh\psi \end{array} \tag{2.17}$$

where the cosmological constant vanishes (equivalently $l \to \infty$). As in that case, the horizon is the sphere S^{n-1}. Notice that, if we set the mass of the BH to zero ($\mu = 0$), this choice of κ is equivalent to the description of pure AdS in global coordinates. In fact, as in that case, the $\kappa = 1$ geometry covers asymptotically the whole hyperboloid and the topology of the conformal boundary is, as expected, $R \times S^{n-1}$.

The largest root of the potential $V(r)$, that we denote by r_+, gives us the position of the event horizon. To compute its temperature we follow the standard procedure [48] where, first, we go to the Euclidean metric by defining $\tau = it$:

$$ds^2 = V_\kappa(r)d\tau^2 + \frac{dr^2}{V_\kappa(r)} + \frac{r^2}{l^2}dK^2_{n-1} \tag{2.18}$$

Now we expand around the horizon $r = r_+$ obtaining:

$$ds^2 = V'^2(r_+)(r - r_+)d\tau^2 + \frac{dr^2}{V'(r_+)(r - r_+)} + \dots \tag{2.19}$$

To see explicitly the conical singularity we make the following change of coordinates:

$$\rho = 2\sqrt{\frac{(r - r_+)}{|V'(r_+)|}} \qquad \chi = \tau\frac{V'(r_+)}{2} \tag{2.20}$$

In these coordinates the metric near the horizon is:

$$ds^2 = \rho^2 d\chi^2 + d\rho^2 + \dots \tag{2.21}$$

These coordinates are like polar coordinates but χ is not restricted to vary in $(0, 2\pi)$. To avoid the conical singularity we have to impose $\chi \in (0, 2\pi)$ and, therefore, τ must be:

$$\tau \in \left(0,\ \frac{4\pi}{V'(r_+)}\right) \Rightarrow \beta_{BH} = \frac{4\pi}{|V'(r_+)|} = \frac{4\pi l^2 r_+}{n{r^2}_+\kappa(n-2)l^2} \tag{2.22}$$

Where we have finally found the temperature of the black hole by identifying its inverse with the period of the imaginary time, as it is usually done in statistical physics.

If we invert the relation between β and r_+ we find a very important feature of black holes in an asymtotically AdS spacetime:

$$r_+ = \frac{2\pi l^2}{n\beta}\left(1 \pm \sqrt{1 - \kappa\frac{n(n-2)\beta^2}{4\pi^2 l^2}}\right) \tag{2.23}$$

Where we see that, if $n \neq 2$, given a temperature β there are two solutions for r_+. The minus branch corresponds to what is called small black holes, and the other one

to large black holes. Although they have the same temperature, its thermodynamics is totally different. We can see this in Figure(2.4), where we compare the dependence of T with μ for the Schwarzschild black hole and the AdS one.[6] In that plot, we can already see that the thermodynamic of small black holes (given a temperature, the ones with smaller mass) is like the thermodynamic of a black hole in Minkowski spacetime, namely, they have negative specific heat and are unstable. Contrary, large black holes have positive specific heat and are stable. These are the ones that are dual to thermal states in the CFT. Although we are not going to make the explicit computations, we could check that, except for a 3/4 global factor, the thermodynamics of large black hole coincides with the one of a thermal state in the CFT side. This is the expected result if we identify large BH with thermal states: when we change the coupling the only thing that can change in these quantities is a global factor.

Small black holes are not stable objects (due to its negative specific heat they cannot be in equilibrium with their Hawking radiation), so they will evaporate as in Minkowski spacetime. Nevertheless, we will be working in the limit where gravity is classical, namely G_N is very small, and, therefore, the Hawking radiation is so suppressed that the evaporation process does not affect the time scales that we are interested in.
In the microcanonical ensemble, which is the one where we will be working in the last two chapters, both small and large black holes are possible final configurations.

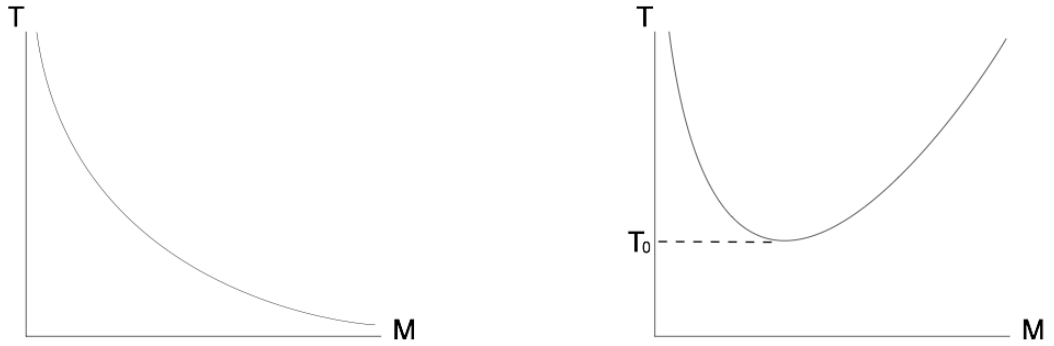

Figure 2.4: Scheme of the dependence of the temperature with the mass (proportional to μ). In the left a Schwarzschild black hole, in the right an AdS Schwarzschild one. Extracted from [49].

[6] As we already know the function $\beta(r_+)$, to find $T(\mu)$ we need the relation between r_+ and μ, which is obtained from the condition $V(r_+) = 0$.

Notice that for the all AdS_d spacetimes, with $d \geq 4$, there are two solutions for r_+ and, therefore, we can differentiate between large BH and small BH (this will be important in the last section, where we will work in an AdS4 spacetime).
In the AdS_3 case there is only one type of BH but, also, the possibility of having naked singularities[7]. To see this let us write explicitly the metric:

$$ds^2 = -\left(1 - \mu + \frac{r^2}{l^2}\right) dt^2 + \frac{dr^2}{1 - \mu + \frac{r^2}{l^2}} + \frac{r^2}{l^2} d\theta^2 \tag{2.24}$$

The singularity is at $r = 0$ and the horizon would be placed at:

$$r^2 = l^2(\mu - 1) \tag{2.25}$$

Which does not have a solution for $\mu < 1$. Therefore, in AdS3, we will have naked singularities if we choose $\mu < 1$.

The $\kappa = 0$ spacetime would be analogous, in the previous sense, to the Poincaré patch of AdS (which just covers half of the hyperboloid). Notice that, in this case, we just have one type of BH.
The $\kappa = -1$ case corresponds to an hyperbolic conformal boundary that, as the $\kappa = 0$ choice, does not cover, asymptotically the whole hyperboloid.

[7]Which are singularities not covered by a horizon.

Chapter 3

Entanglement Entropy

We are interested in monitoring the time evolution of entanglement after a perturbation in a QFT, for this purpose we will use the Holographic Entanglement Entropy, but before going through it let us introduce some concepts that are not related to holography.

3.1 Introduction: Quantum Mechanics

Entanglement is an intrinsically quantum property that was first formulated to describe the non local information stored in the wave functions of systems of identical particles [50]. As an easy example we can consider a system of two identical particles of spin 1/2 that we will call A and B. If the wave function of the system is

$$|0_S, 0_{Sz}\rangle = \frac{1}{\sqrt{2}} \left(|\uparrow_A, \downarrow_B\rangle - |\downarrow_A, \uparrow_B\rangle \right) \tag{3.1}$$

and we place the particles A and B as far away as we want, we can still see that the measure of the spin $(\uparrow, \downarrow)$ of the B particle determines the spin of the A particle (and vice versa). This is an entangled state (particles A and B show a quantum correlation).
If we now place the same system in the state:

$$|1_S, 1_{Sz}\rangle = \frac{1}{\sqrt{2}} \left(|\uparrow_A, \downarrow_B\rangle - |\uparrow_A, \uparrow_B\rangle \right) \tag{3.2}$$

the measure of one spin does not affect the value of the other, there is no correlation, and therefore no entanglement between A and B.

If we restrict to pure states (which are the ones we are going to be dealing with) we can use entanglement entropy as a measure of quantum entanglement. We will

define it in the following lines.

Let be $|\Psi\rangle$ the pure quantum state of a general physical system Σ. As in the previous example, we consider a partition of Σ in two subsystems A and B such that $\Sigma = A \bigcup B$ and $A \bigcap B = \emptyset$. Now we can define the reduced density matrix for A tracing over the degrees of freedom in B:

$$\rho_A = Tr_B \rho \tag{3.3}$$

Where ρ is the density matrix of all the system $\rho = |\Psi\rangle\langle\Psi|$. Notice that ρ_A is the density matrix an observer restricted to A would see. In general, it will be the one of a mixed state. As an example, we can compute ρ_A for the state defined in expression (3.1):

$$\rho_A = Tr_B \left(|0_S, 0_{Sz}\rangle\langle 0_S, 0_{Sz}|\right) = \frac{1}{2}\left(|\downarrow_A\rangle\langle\downarrow_A| + |\uparrow_A\rangle\langle\uparrow_A|\right) \tag{3.4}$$

In general, we define the entanglement entropy of the subsystem A as the Von Neumann entropy of ρ_A:

$$S_A \equiv -Tr_A(\rho_A \log \rho_A) \tag{3.5}$$

Before applying this definition to the previous examples let us se that, indeed, S_A measures entanglement in pure states.
Given a pure quantum state $|\Psi\rangle$ we can write its Schmidt decomposition:

$$|\Psi\rangle = \sum_{n=1}^{D} \lambda_n |\Psi_n^A\rangle |\Psi_n^B\rangle \tag{3.6}$$

Where it is assumed that the physical system admits a partition of the form $\Sigma = A \bigcup B$; $A \bigcap B = \emptyset$, where we can split the total Hilbert space as $H_\Sigma = H_A + H_B$. In addition $D = \min(dim(H_A), dim(H_B))$.
With this expression it is easy to compute S_A:

$$\rho_A = \sum_{n=1}^{D} |\lambda_n|^2 |\Psi_n^A\rangle\langle\Psi_n^A| \Rightarrow S_A = -\sum_{n=1}^{D} |\lambda_n|^2 |\log |\lambda_n|^2 \tag{3.7}$$

At first sight we realize that $S_A = S_B$, meaning that A is as entangled with B as B is with A. If this property would not hold, our observable would be measuring something different than entanglement. This is what happens in mixed states, where this quantity has also statistical contributions.
However, to see that S_A is actually a measure of entanglement, we can see that S_A only vanishes when ρ_A is itself a pure state, meaning that the state Ψ is a product

state on $A \bigcup B$, namely, A and B are not entangled at all.
The entanglement entropy fulfills two more properties that we show here without proof:

- Subadditivity. Given two regions A and B:
  $S_{A\cup B} \leq S_A + S_B$
- Strong Subadditivity. Given three regions A, B and C:
  $S_{A\cup B\cup C} \leq S_{A\cup B} + S_{B\cup C} - S_B$
  $S_A + S_C \leq S_{A\cup B} + S_{B\cup C}$

3.2 Entanglement entropy in a QFT

Given a QFT in $d+1$ dimensions that lives in a $R \times N$ manifold, where R is the time direction, we can define the d dimensional subsystem A, as a subset of N when the time is fixed at $t = t_0$. B is the complement of A such that $A \bigcup B = N$ at $t = t_0$.
The definition of S_A is given, as in the previous section, by Eq(3.5). Nevertheless, notice that, as a QFT in the continuum has infinite degrees of freedom in any infinitesimal spatial region, S_A is always a divergent quantity. To regularize it we introduce a lattice of spacing a (an ultraviolet cutoff).
In most of the physical systems, we obtain the area law for the entanglement entropy[51, 52, 37]:

$$S_A = \gamma \frac{Area(\partial A)}{a^{d-1}} + \dots \tag{3.8}$$

Where ∂A is the boundary of A in N and γ is a non universal coefficient. The area law can be intuitively understood by thinking that correlations between points decrease with the distance, so entanglement between A and B should be stronger in the boundary ∂A. Therefore, it is reasonable to think that the leading term of S_A should be proportional to the area of ∂A, as the area law states.

Nevertheless, as advanced, there are cases in which this law does not hold. A simple case is a 2D CFT living in an infinite line in its ground state, where the entanglement entropy of a single interval is given by:

$$S_A = \frac{c}{3} \log \frac{l}{a} \tag{3.9}$$

Where c is the central charge of the CFT and l the length of the interval. This result generalizes to all 2D CFT in their ground states. Namely, the EE of a single interval

in the ground state of a 2D CFT has a universal behavior (notice that it only depends on c and l) [53, 54, 55, 56].
We will see that this result for S_A is reproduced holographically.

Another important result that we are going to use in the following sections, is the entanglement entropy, in the same kind of theories (2D CFT), of an interval at thermal equilibrium [56]:

$$S_\beta(l) = \frac{c}{3} \log \left(\frac{\beta}{\pi\epsilon} \sinh \frac{\pi l}{\beta} \right) \tag{3.10}$$

where β is the inverse of the temperature.

3.2.1 Entanglement entropy after a quench. Propagation model.

In this section we focus on the results that Cardy and Calabrese obtained when they studied the time evolution of the Entanglement Entropy after a quench in a CFT in 1+1 dimensions [1, 57, 58]. A quench is a way to start a non trivial evolution in a system: at the beginning the QFT is in an eigenstate of the hamiltonian, then, a parameter of this hamiltonian is suddenly changed, and, as a consequence, a non trivial evolution of the system starts (it is non trivial because the old eigenstate is not an eigenstate of the new hamiltonian).
In the quench they performed, the system was initially in the ground state of a given hamiltonian with a mass gap m. Suddenly, a parameter of the hamiltonian was changed so that the dynamics after the quench was conformal. In this setup, they found that for large enough times and intervals ($t, l \gg 1/m$) the evolution of the EE was given by [1, 57, 58] :

$$S(l,t) \approx \frac{c}{3} \ln \frac{2\tau_0}{\pi} + \begin{cases} \dfrac{\pi c t}{6\tau_0}, & t < l/2 \\ \\ \dfrac{\pi c l}{12\tau_0}, & t > l/2 \end{cases} \tag{3.11}$$

Where τ_0 is of the order of $1/m$.
The EE grows linearly with time until it achieves a maximum[1] at $t = l/2$, where it coincides with the thermal equilibrium value of Eq(3.10). Identifying $\beta = 1/T$ with $4\tau_0$, allows us to define an effective temperature for the long wavelength modes. Therefore, we can say that the EE at a given time t, reaches thermal values for regions

[1]Notice that the sharp change in $t = l/2$ is expected to smooth out over a region of order $1/m$.

of size $t > l/2 \gg 1/m \approx \beta$. Notice that this system never equilibrates globally: for all times t we can always find a region $t < l/2$ which has not reached equilibrium.
Surprisingly, even if this theory is not diagonalizable in terms of free particles, Cardy and Calabrese managed to give a phenomenological interpretation of the behavior of the EE in terms of "excitations" or "pesudoparticles". They realized that, if they thought about the energy density created after the quench as distributed in pairs of excitations that move clasically, at the speed of light and without scattering, they could reproduced the behavior of the EE with time. The time evolution of a pair of these excitations is shown in Figure (3.1), where a particular example is discussed in detail. We will say that there is entanglement between points x_1 and x_2 if we can find two entangled excitations in those points (in the Figure (3.1) the black excitations are entangled among themselves and the same for the grey ones). As the state previous to the quench was the ground state of a hamiltonian with a mass, it will have a finite correlation length τ_0 and therefore we will not find entanglement at lengths $l > \tau_0$. That is why in Figure (3.1), where we have chosen an infinite mass gap, at $t = 0$ (just after the quench) entangled excitations are shown at the same point. Then, these excitations just spread all over the space so that, as the time passes, we will have entanglement at larger and larger scales.
These excitations are a pictorial way of monitoring the time evolution of entanglement after the quench. The relation with the entanglement entropy is straightforward: the EE of a given region of size l is proportional to the number of excitations inside the interval that are entangled with the outside (see Figure (3.1)). It is important to mention that this pictorial way of explaining the time evolution of the EE, does not apply to the mutual information [59] which, also, monitor the evolution of entanglement.

3.3 Holographic Entanglement Entropy

Until now we have not said anything about the holographic computation of the entanglement entropy. Although some results can be obtained using QFT tools, computations become harder when we deal with theories at strong coupling, in time dependent situations and in $2 + 1$ dimensions. The AdS/CFT correspondence offers a straightforward way to obtain the EE which, when is computed holographically, is called Holographic Entanglement Entropy[52].

Let us suppose that we have a QFT_{d+1} living in a $N \times R$ (where R is the time direction) spacetime whose holographic dual is known (it would be a gravity theory

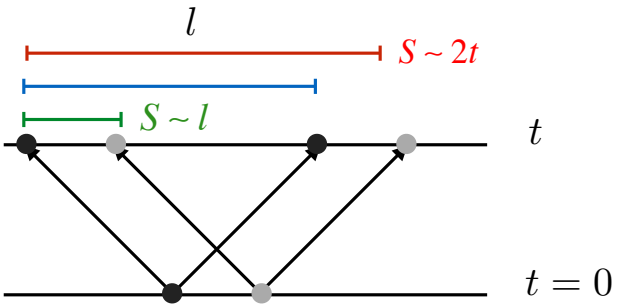

Figure 3.1: Scheme of the kinematical propagation of entanglement proposed by Cardy and Calabrese. The quench is performed at $t = 0$ where we find entanglement at a very short scale. In the figure this is signaled with two entangled pair of excitations (in black and grey) whose evolution in time is shown with arrows. After a time t the excitations will have moved and now we will find entanglement at a larger scale (signaled in blue). Regarding the entanglement entropy of an interval of size l, we find that for the green interval the EE has thermalized because all the excitations that we find inside it are entangled with the outside. This is not the case for the red interval, where the EE is still proportional to l.

in $d+2$ dimensions). As in the previous sections, we want to compute the entanglement entropy of a region $A \subset N$ such that $A \cup B = N$ and $A \cap B = \varnothing$. To do so we would need to extend the division between A and B into the bulk spacetime, and the natural way to do it would be to notice that, at least in static spacetimes, there is a timelike Killing vector field that induces a foliation of the whole bulk spacetime, and its boundary, into spacelike surfaces. Therefore, as we have already divided the spacelike surface of the boundary in the regions A and B, we would have to divide the corresponding time slice spacetime M, which is an euclidean manifold of dimension $d+1$, with a curve γ_A, of dimension d, such that $\gamma_A \in M$. The intuitive way to do so, is to choose γ_A so that it anchors, at the boundary of the spacetime, to the boundary of the region A (see Figure(3.2)).

But, with this intuition, we still have infinite possible choices of the curve γ_A. The claim is to choose the one with minimal area (in the following lines we will give an intuitive idea of why is this).

With this setup the entanglement entropy of a region A in the dual CFT_{d+1} is given by:

$$S_A = \frac{\mathrm{Area}(\gamma_A)}{4G_N^{d+2}} \tag{3.12}$$

Where G_N^{d+2} is the Newton constant of the AdS_{d+2} spacetime with gravity.

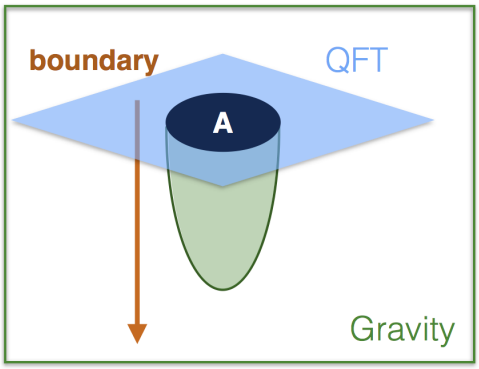

Figure 3.2: Scheme of the computation of the HEE.

However, it is not straightforward to apply this reasoning to time dependent situations because, in this case, there is no natural choice of time slices (in fact, we have infinitely many different options) and the assumption of a well defined time slice with euclidean signature, where we have to find a minimal surface, is not correct. In time dependent situations, we have to take into account all the AdS spacetime, and find γ_A with the same boundary conditions that we used before, but now, it has to be an extremal surface (which is the natural generalization of a minimal surface, in an Euclidean manifold, to a Lorentzian one). We can summarize this in the formula:

$$S_A(t) = \frac{\text{Area}\left(\gamma\left(t\right)\right)}{4G_N^{d+2}} \tag{3.13}$$

Which is called Covariant Holographic Entanglement Entropy[41]. Notice that t is the time on the time slice in the spacelike boundary (that we cannot extend to the entire bulk spacetime).

To gain some intuition about the two previous formulas of the HEE, we can relate them to the area law in Bekenstein-Hawking expression, where the entropy of a black hole S_{BH} is computed:

$$S_{BH} = \frac{\text{Area}(\Sigma)}{4G_N} \tag{3.14}$$

Where Σ is the event horizon. In fact, the formula of the HEE can be thought as a generalization of Eq(3.14) in the following intuitive sense. We have defined the EE of a region A by smearing out the rest of the spacetime B. Therefore, we can consider S_A as the entropy an observer restricted to the region A would measure. In the holographic part this would be equivalent to hide part of the bulk spacetime inside a horizon γ_A. Using the entropy bound, which roughly speaking tell us that

the entropy contained in a given region is always bounded by the area of its surface, we can understand the condition of minimization imposed on γ_A: it implies we are imposing the severest entropy bound so that we may saturate it and actually find S_A.

3.3.1 Holographic Entanglement Entropy with Black Holes: homology condition

There is still another condition for the choice of the surface γ_A in the computation of the HEE that we have to explain. It becomes crucial when we are dealing with black hole backgrounds, both when the BH is eternal and when it has been formed by collapse.

Let us focus on some particular cases where it is explicitly shown that the condition we asked for the γ_A surface (that it anchored at the boundary of the region A and it is extremal) is not enough to uniquely define it.

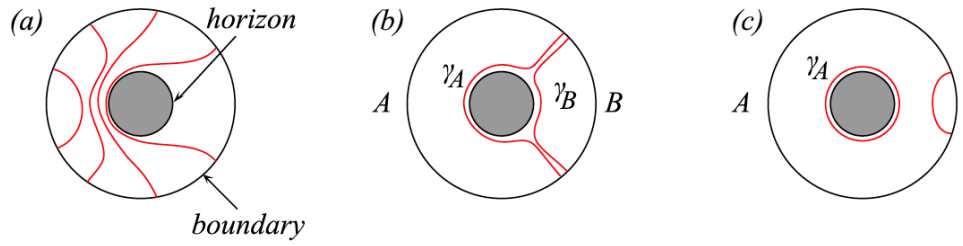

Figure 3.3: Scheme of the computation of the HEE in a background with an eternal BH. Extracted from [52]

The first case we analyze is the **eternal black hole in global coordinates**[52]. In Figure(3.3) we see how there are two curves that fulfill the asked conditions: both γ_A and γ_B are extremal and anchor at the boundary of A. We could argue that, as the eternal black hole is not a time dependent metric, we have to choose the γ curve with minimal area. However, notice that with this reasoning we will choose the same curve γ_A to compute the entanglement entropy of both regions, A and its complement B. They will have the same entanglement entropy. But we know that this is not true in a mixed state, which is precisely the holographic QFT dual of an eternal black hole. The condition we have missed is that γ_A must be homologous to A. With this condition the previous problem is solved, because it is clear that the EE of A and B is given by different curves γ_A and γ_B with different areas.
Another consequence of the homology condition is that when the region A becomes

very large, the curve γ_A with minimal area will not be the one shown in Figure (3.3.b) but the one in the same figure, part (c). Notice that this curve, that is actually split in two curves (one that wraps the horizon and the another one anchored in the boundary) fulfill the three asked conditions: it is homologous to A, its boundary anchors at the boundary of A and it has minimal area.

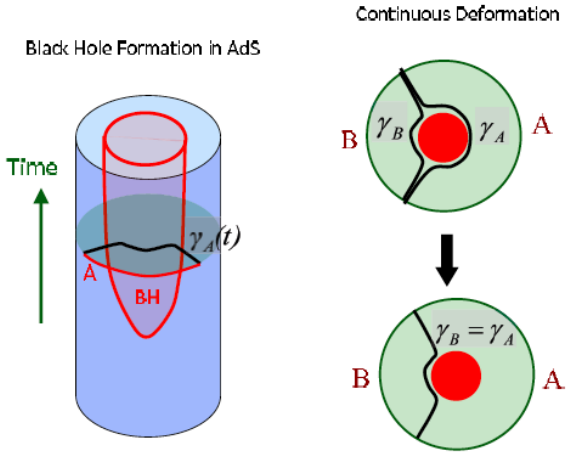

Figure 3.4: Scheme of the computation of the HEE in a background where a BH is being formed. Extracted from [60]

Once we have analyzed the eternal black hole we may ask if the homology condition has similar consequences in the case of a **black hole formed by gravitational collapse** [61, 60]. Let us suppose we are working in global coordinates and we want to compute the EE of region A, shown in the left part of Figure(3.4). We may think, as in the previous case, that the homology condition will force us to take the γ_A curve because, as before, γ_B is not homologous to A. Nevertheless, this is not the case in a black hole formed by gravitational collapse, because the horizon has not always been there, it has been formed at some point (this is explicitly shown in the left part of Figure(3.4)) and, as a consequence, we can continuously deform the γ_A curve until it coincides with γ_B. Therefore, the minimal curve we have to choose to compute the EE of A in this background is γ_B.
Notice that, as γ_A can be deformed until it coincides with γ_B, both regions, A and its complement B, have the same entanglement entropy. Although this condition is not enough to say that the dual state in the QFT is pure, it is a necessary condition for it. Let us comment a little bit more using a particular example developed in [61].

There, the evolution starts in empty AdS which is a pure state in the dual QFT. As the evolution after the quench is unitary, the state remains pure the whole time evolution and, therefore, both regions A and its complement B must have the same entanglement entropy. However, it is found that, during this evolution, the EE of A reaches its thermal value. This is because, although the state is pure, the rest of the system acts as a thermal bath for A and, locally, we can see results which are typical of a mixed state.

Chapter 4

Holographic model for a quench in a compact spacetime

In this chapter we present one of the main results of this thesis, namely, a holographic model for revivals in a strongly coupled QFT. As an observable, we computed the holographic entanglement entropy for time dependent backgrounds, and using our results we managed to give, from the gravity side, a reasonable interpretation of the dynamics of entanglement.

To this aim, we studied geometries that model gravitational evolution with a massless scalar field [24, 25, 27, 28, 29, 32, 34]. It was already seen in [20, 19], that the holographic representation of a relaxation process on the field theory side is the gravitational collapse of a certain matter distribution.

4.1 Bouncing geometries

4.1.1 Description of AdS_4 and AdS_3 geometry

The geometries that, under some conditions, lead to "bouncing geometries" were, in the AdS_4 case, originally studied by Bizon and Rostorowski in [24], where they were trying to answer the question "Is AdS stable?". Contrary to Minkowski and de Sitter spacetimes, which were known to be stable under small perturbations [62, 63], not much was known about the AdS case. The main difference is the presence, in the AdS spacetime, of a timelike boundary at spatial and null infinity where boundary conditions must be specified. For no-flux conditions, the energy is conserved on an effectively bounded domain. Bizon and Rostorowski placed, in empty AdS and with these no-flux conditions, small perturbations that were well localized in space and propagated in time as a narrow wave packet. They found that, no matter how

small the perturbation was, a black hole was always formed after enough bounces of these perturbations against the timelike boundary of AdS. These kind of geometries is what, in this thesis, we will be calling "bouncing geometries".

The gravitational action Bizon and Rostorowski studied in [24] was given by:

$$S = \int d^{d+1}x\sqrt{g}\left(\frac{1}{2\kappa^2}\left(R - 2\Lambda\right) - \frac{1}{2}\partial_\mu\phi\partial^\mu\phi\right) \tag{4.1}$$

where $\kappa^2 = 8\pi G$, $\Lambda = -d(d-1)/2l^2$ and d is the dimension of QFT dual spacetime. We will study this action in two cases[1]: $d = 2$, where the QFT lives in $S^1 \times R$, and $d = 3$, where the QFT lives in $S^2 \times R$.
As we are interested in modeling global quenches and, therefore, we do not want to break spatial symmetries, we only focus on solutions that are spherically symmetric. An ansatz for the line element which fulfills this condition is:

$$ds^2 = \frac{1}{\cos^2 x}\left(-A(t,x)e^{-2\delta(t,x)}dt^2 + \frac{dx^2}{A(t,x)} + \sin^2 x d\Omega_{d-1}^2\right) \tag{4.2}$$

Where $x \in [0, \pi/2]$ is a compact radial coordinate and $d\Omega_{d-1}$ is the differential solid angle of dimension $d-1$. From this ansatz we know two important things, that the static pureAdS solution corresponds to:

$$A(t,x) = 1 \qquad\qquad \delta(t,x) = 0 \tag{4.3}$$

and that a zero in $A(t, x_h)$ signals the formation of an apparent horizon in x_h. Notice that, as we are interested in the dynamical formation of a black hole, we will be tracking during the whole evolution the apparent horizon and its growth.

Before going on with the equations of motion, it may be useful to keep in mind an image of what is going on in this geometry. To do so we notice that, with the coordinates we are using, we can think about the geometry as a sphere that evolves in time: the radius would be the coordinate $x \in [0, \pi/2]$ and the angular coordinates would appear in $d\Omega_{d-1}$. The kind of narrow perturbations Bizon and Rostorowski analyzed in [24], can be identified with the shell that in Figure(4.1) is falling from the boundary towards the origin. If this perturbation is massive enough, a black hole will be formed in the first fall of this shell towards the origin. If not, the shell will come back to the boundary, bounce there, and fall again towards the origin repeating this bouncing process until an apparent horizon is formed.

[1]Notice that, in both cases, we have chosen global coordinates.

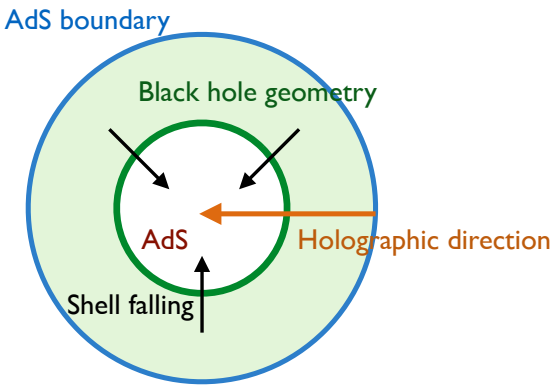

Figure 4.1: Scheme of the bouncing geometries described in the text.

Due to Birkhoff's theorem, observables that lie between the boundary and the shell itself at a given time[2], will not distinguish between the fall of the shell and a BH of the corresponding mass. Therefore, we can find observables (in particular the EE) that, for some time, can reach thermal values much before the BH is formed.

In a more quantitative way, we will characterize the bounces of the geometry with the function $A(x,t)$, that has a characteristic behavior when the shell is located at the boundary and at the origin:

- When the shell is located at the boundary the back reaction is minimized by the inverse cosine in the metric, so that the resulting metric is almost pureAdS. As a result $A(x,t) \approx 1$.

- When the shell is localized enough while it travels from the boundary to the origin, the minimum in x of $A(x,t)$ decreases, until reaching a minimum that signals the moment at which the shell is mainly located at the origin. If the apparent horizon is formed in this fall towards the origin, the minimum in x of $A(x,t)$ drops to zero (see Figure(4.3)).

Therefore we can define the function:

$$A_m(t) = \min_x A(t,x) \tag{4.4}$$

as a way to follow the "bounces" of the geometry (see Figure(4.2)).

[2]Here by time we mean the time t at the boundary.

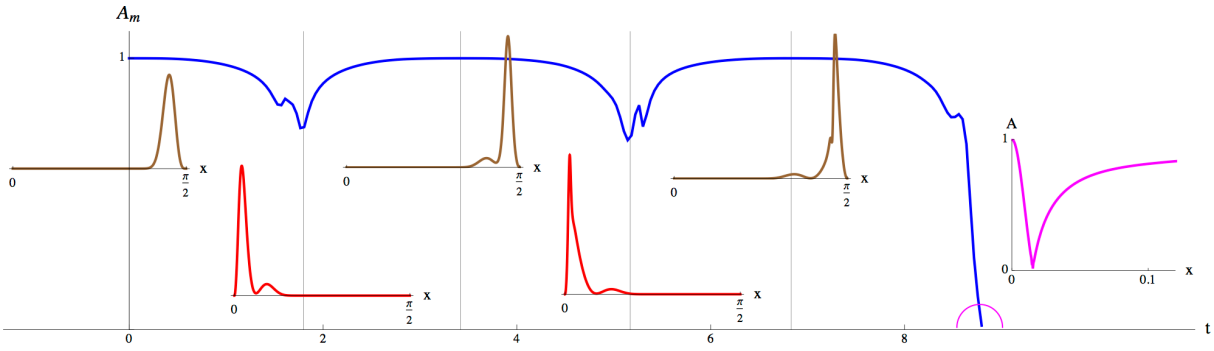

Figure 4.2: In blue, evolution of $A_m(t)$ for a typical thin shell in AdS_4. It needs two bounces with the AdS boundary for collapse. In brown and red, the radial energy distribution of the shell (see Eq(4.10)) at the times indicated by the vertical lines. In magenta, A develops a zero signaling black hole formation.

To solve the EOM we will express the scalar field in terms of its derivatives as $\Phi = \phi'$ and $\Pi = A^{-1}e^{\delta}\dot{\phi}$ (where $'$ represents derivatives with respect to the radial coordinate x and the dot with respect to time t). Therefore [24]:

$$\dot{\Phi} = \left(Ae^{-\delta}\Pi\right)' \quad , \quad \dot{\Pi} = \frac{1}{\tan^{d-1} x}\left(\tan^{d-1} x\, Ae^{-\delta}\Phi\right)' , \tag{4.5}$$

$$A' = \frac{d-2+2\sin^2 x}{\sin x \cos x}(1-A) - \sin x \cos x\, A\left(\Phi^2+\Pi^2\right), \tag{4.6}$$

$$\delta' = -\sin x \cos x \left(\Phi^2+\Pi^2\right). \tag{4.7}$$

Using these equations we can obtain the "momentum constraint":

$$\dot{A} + \frac{2}{d-1}(\sin x \cos x)A^2 e^{-\delta}\Pi\Phi = 0 \tag{4.8}$$

This equation tells us that $A(t,0)$ is constant. As we are interested in modeling an isolated system in the QFT side, we choose the non normalizable mode of the scalar field to be zero, so that the total mass of the gravity system is conserved. A variation of this mode, would imply a variation of a coupling in the hamiltonian of the dual QFT and, therefore, an injection of energy which can model a quench. However, as Bizon and Rostorowski in [24], we did not introduce the perturbation in this way, but we directly start the simulation by imposing a profile in the scalar field (see Eq(4.12)).

For the forthcoming analysis it is useful to define $\mathcal{M}$, which is proportional to the total mass M (see Eq(4.15)):

$$\mathcal{M} = \int_0^{\pi/2} (\tan x)^{d-1}(\Phi^2+\Pi^2)A dx \tag{4.9}$$

Fulfillment of the "momentum constraint", together with constancy of the mass, have been used as a quality check of our numerical simulations.

It is interesting to define $\rho(t,x)$, which integrated over all the space gives us $\mathcal{M}$:

$$\mathcal{M} = \int_0^{\pi/2} dx \rho(t,x), \qquad \rho(t,x) = (\tan x)^{d-1}(\Phi^2 + \Pi^2)e^{-\delta} \tag{4.10}$$

This quantity gives us the radial energy distribution of the shell. However, notice that the first equality does not uniquely determines $\rho(t,x)$. There is another option $\overline{\rho}(t,x)$ whose definition is:

$$\mathcal{M} = \int_0^{\pi/2} dx \overline{\rho}(t,x), \qquad \overline{\rho}(t,x) = (\tan x)^{d-1}(\Phi^2 + \Pi^2)A \tag{4.11}$$

Nevertheless, both functions $\rho(t,x)$ and $\overline{\rho}(t,x)$, give quite similar results and do not alter the holographic interpretation.

We ask for regularity at the origin, which implies $A(t,0) = 1$. Besides, there is a gauge freedom left over by the ansatz of Eq(4.2): the system is invariant under reparametrizations of the form $t' = f(t)$. To fix this gauge freedom we have chosen in both spacetimes the condition $\delta(t,\pi/2) = 0$. That is, we have required t to be the proper time at the boundary, which is a natural choice from the QFT perspective.

As initial data we set the derivatives of the scalar field Π, Φ at time $t = 0$. The profile we have chosen is a gaussian profile located at the boundary for $\Pi(0,x)$, while $\Phi(0,t)$ is set to zero (in the following sections we will see some other initial profiles we also used):

$$\Phi(0,x) = 0\,, \qquad \Pi(0,x) = \epsilon \exp\left(-\frac{4\tan^2(\pi/2 - x)}{\pi^2\sigma^2}\right)\cos^{d-1} x\,. \tag{4.12}$$

Under all these conditions, the expansions of the fields close to the origin are:

$$\phi(x,t) = \phi_0(t) + \mathcal{O}(x^2), \qquad A = 1 + \mathcal{O}(x^2), \qquad \delta = \delta_0(t) + \mathcal{O}(x^2) \tag{4.13}$$

Near the boundary:

$$\phi(x,t) = \phi_\infty(t) y^d + \mathcal{O}(y^{d+2}), \qquad A = 1 - \mathcal{M} y^d + \mathcal{O}(y^{d+2}), \qquad \delta = \mathcal{O}(y^{2d}) \tag{4.14}$$

Where we have defined $y = \pi/2 - x$.

With this information, we can find different kinds of solutions depending on the broadness of the pulse and the mass:

- Formation of the BH in the first infall towards the origin.
- Formation of the BH after some bounces of the shell with the boundary.
- No formation of the BH.

There is an important difference between AdS_3 and AdS_4 that we have already studied in Chapter 2 and is sketched in the next table. In spacetimes that are asymptotically AdS_4 we can have both, large and small black holes, depending on the value of the mass. This is not the case in an asymptotically AdS_3 spacetime, where, for $0 < \mathcal{M} < 1$, we can only find naked singularities that are not expected to be formed dynamically. This difference changes the thermalization pattern that we find in both spacetimes.

AdS_4 spacetime		**AdS_3 spacetime**	
$\mathcal{M} < \mathcal{M}_{th}$	$\mathcal{M} > \mathcal{M}_{th}$	$\mathcal{M} < 1$	$\mathcal{M} > 1$
Small BH	Large BH	Naked Singularity	Black Hole

In the forthcoming sections we will keep on with the comparison between these two spacetimes and its effects in the QFT interpretation.

At this point, let us make some comments about what we understand by mass. First, we have to distinguish between the mass of the black hole, that we denote by M_{BH} and the $\mathcal{M}$ we have been using and explicitly appears in the metric of an AdS-Schwarzschild black hole (see Eq(2.16)). They are related by the inverse of G_N, and a volume factor that we write here in global coordinates:

$$M_{BH} = \frac{(d-1)}{16\pi G}\text{Vol}(S^{d-1})\mathcal{M} \tag{4.15}$$

Although we will analyze it in more detail in the next sections, we can already explain what is this $\mathcal{M}$ in the dual QFT. In holography, the mass of the black hole M_{BH} corresponds to the energy of the CFT, and the central charge on the QFT side is dual to the inverse of G_N [64]. Therefore, we can identify $\mathcal{M}$ with the energy density per species in the field theory.

4.1.2 Pre-horizon dynamics

In this section we focus on the analysis, until the first emergence of the apparent horizon, in the four dimensional case ($d = 3$) where the spacetime is asymptotically AdS_4. Obviously, we have not analyzed all the possible initial conditions for the evolution (see [31, 30] for different initial conditions), but we have restricted to gaussian type profiles that we have localized both at the boundary and at the origin of AdS. Explicitly, the initial profile located at the origin is given by [24]:

$$\Phi(x) = 0, \qquad \Pi_c(x) = \frac{2\epsilon}{\pi} \exp\left(-\frac{4\tan^2(x)}{\pi^2\sigma^2}\right) \tag{4.16}$$

and the profile located at the boundary:

$$\Phi(x) = 0, \qquad \Pi_b(x) = \frac{12\epsilon}{\pi} \exp\left(-\frac{4\tan^2(\pi/2 - x)}{\pi^2\sigma^2}\right) \cos^3 x \tag{4.17}$$

Let us analyze how a horizon is formed in this setup.

As was sketched in the previous section, a zero in the $A(x, t)$ function signals the appearance of a horizon. However, we will never see $A(x_h, t) = 0$, not only because of the numerical computations, but also because when this function approaches zero, the relative redshift factor with respect to the boundary becomes very large, and the dynamics near the horizon gets frozen. Therefore it is not possible to see exactly the equality $A(x_h, t) = 0$, we will just see how this functions gets smaller and smaller until reaching a value that is almost zero.

In the previous section we have introduced what we understand by bounces in this geometry, but we have not talked about the conditions for this to happen. If the mass $\mathcal{M} > \mathcal{M}_{th}$ (as defined above) we will form a large black hole by trapping all the mass in the first infall of the pulse towards the origin. As the total $\mathcal{M}$ is lowered, the number of bounces before the formation of the apparent horizon increases. Interestingly, in these cases the horizon is formed with just a fraction of the total pulse. This is because, in each of the bounces, the part of the pulse that will end up forming a black hole sharpens, and the energy density increases. While this part of the pulse sharpens, the rest increases its broadness (see Figure(4.3)).

However, this is not a totally generic procedure, and depends also on the initial broadness of the pulse. In [24, 25, 26] it was shown how always narrow enough profiles of arbitrary small initial $\mathcal{M}$, end the evolution forming a black hole after enough bounces against the boundary. As we have just advanced, this happens because of the transfer of energy from long to small wavelengths, and it is clearly related to the sharpening of part of the pulse. In fluid dynamics [65] this is known as **weak turbulence**.

As it is shown in Figure(4.3) and due to this weak turbulence effect, the pulse suffers a change of shape mainly at the origin. It happens there because is where the fields reach bigger values and, therefore, the effect of nonlinearities is enhanced. Notice how the rest of the pulse increases its radial dispersion in each bounce at the origin. As expected, the first apparent horizon is formed with the mass of the small spiky front in the brown profile.

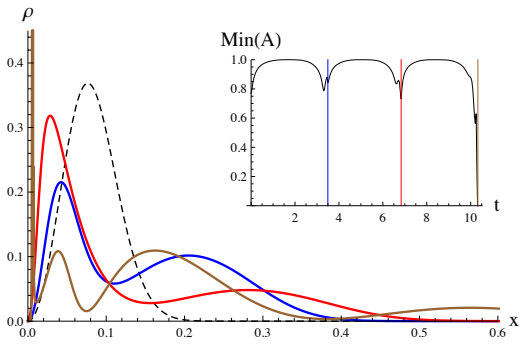

Figure 4.3: In blue, evolution of $A_m(t)$ for a typical thin shell in AdS_4. It needs two bounces with the AdS boundary for collapse. In brown and red, the radial energy distribution of the shell at the times indicated by the vertical lines. In magenta, A develops a zero signaling black hole formation.

Let us now analyze what happens with profiles with a **mass $\mathcal{M} < \mathcal{M}_{th}$ but with a broad initial shape**. In general, when a pulse evolves in time it suffers two competing effects. One of them is weak turbulence, which, as we have already shown, dominates gravitational collapse in narrow pulses and it is related with the gravitational interaction which tends to localize the pulse. The other effect is the scattering among subpulses which, contrary to weak turbulence, tends to scatter the pulse. It was already shown in [32] that, in broad pulses, the dominating effect is the last one: the profile develops a subpulse structure with infalling and outgoing components which scatter among themselves. Let us point out the main characteristics of these evolutions:

- Contrary to narrow profiles, broad pulses do not sharpen during the evolution and they keep delocalized the major part of it. Besides, the broader they are, the stronger the dispersion effect is.

- The periodicities of these solutions are determined by a subpulse structure and, therefore, they are not so well defined as the ones of narrow profiles (see Figure

(4.7)).

- Related to the fact that, in broad pulses, the weak turbulence is not the leading effect, the formation of the apparent horizon is achieved with a finite fraction of the pulse mass (in narrow profiles this fraction can be infinitesimally small).

The last point requires further comments. Contrary to narrow profiles, broad pulses can only form an apparent horizon if their masses are above 40% of the threshold mass $\mathcal{M}_{th}$. What is actually seen in numerical computations is that, as we lower the mass, a point is found where the time for the formation of a horizon abruptly increases [32, 33], namely, no black hole seems to be formed for masses below 40% of the threshold $\mathcal{M}_{th}$. In these last cases, our results join previous work supporting the establishment of a regular quasi-standing wave [30, 31, 32, 33].

As we have argued that, in broad pulses, the scattering among subpulses is essential for the evolution, we found interesting to analyze a different initial configuration: a linear combination of the gaussian profiles described in Eq(4.16, 4.17).

$$\Phi(x) = 0, \qquad \Pi(x) = \Pi_c(x) + \Pi_b(x) \tag{4.18}$$

Namely, as initial data we combined, simultaneously, a pulse at the origin with one at the boundary in two different cases (see Figure(4.4)). In one of these cases the two profiles do not have any overlap, while in the other the pulses are broad enough to have some overlap in their tales. As a result we found:

- When the subpulses that we combine have some overlap, the time of the horizon formation is delayed with respect to the independent evolution of the pulse that would collapse first.

- When the subpulses that we combine do not have any overlap, they are practically transparent to each other, their evolution is almost independent.

As a consequence of these results, it seems that scattering tends to work against weak turbulence.

4.1.3 Post-horizon dynamics

In this section we will talk about the **post horizon evolution**. Until now we have analyzed the evolution of different initial conditions until the the first emergence of apparent horizon. Both, from the point of view of the gravity theory and from the

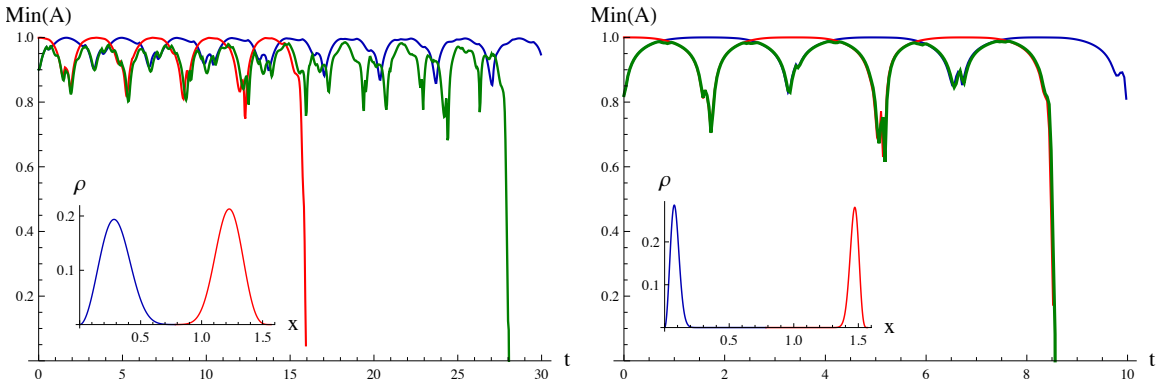

Figure 4.4: Evolution of the initial data 4.16 (blue), 4.17 (red) and the combined profile 4.18 (green) for the following subpulse data. Left: $\sigma = 0.25$ and $M = 0.012$. Right: $\sigma = 1/16$ and $M = 0.029$. In the inset, the initial mass density function. The left initial data have more overlap than the right ones. The horizon formation time for the fast collapsing pulse (red curve) gets affected and delayed (green curve), whereas it remains unaltered in the non-overlapping case on the right.

QFT interpretation by the AdS/CFT correspondence, it is interesting to understand what happens after the first emergence of the horizon.

After the first emergence of the horizon, let us say at position x_h, the dynamics around this position gets practically frozen as expected. Nevertheless, part of the pulse is able to scape the gravitational potential, come back to the boundary and fall again towards x_h. In this "second" fall the process repeats and part of the pulse is swallowed by the horizon while the rest goes back to the boundary. In principle, this bouncing process will continue until the formation of a final black hole with all the mass available in the system. We have been able to simulate several examples of this post horizon dynamics using grids of 10^5 points. To check that our simulations where good enough to analyze this part of the evolution, we have verified that the momentum constraint remained under control during the evolution, that the total mass kept constant up to few percent, and that all functions converge smoothly under variations of the resolution.

As we may expect from results presented in previous lines, post horizon dynamics also depends on the initial broadness of the pulse. To show our results on this matter, we will start by presenting on detail the post horizon evolution of a narrow pulse. Then, we will comment on results of broad pulses and we will compare its main differences.

Let us show in detail one of these post horizon evolutions whose initial gaussian

profile has $\sigma = 0.1$ and $M = 0.021$, namely, a **narrow profile** for which the first appearance of the horizon happens in its second fall towards the origin. For this purpose we have included several plots in Figure(4.5). In the inset of the plot on the left we show the evolution of the Min(A) together with the percentage of mass lost. We have used three vertical lines to signal the three different times where we have plotted the mass density function (see expression (4.10)) on the left, and the A(x,t) function on the right. By using these vertical lines we separate the evolution in three steps:

1 As was commented in previous lines and can be seen in the evolution of Min(A), the first appearance of the horizon happens in the second fall towards the origin. Immediately after this (at a time signaled with a blue vertical line in the inset) we have plotted, on the left, the mass density function $\rho(t, x)$, and on the right the $A(x, t)$ function. With these two plots, we can see how part of the pulse has formed an apparent horizon and is trapped at the origin, while the rest is moving towards the boundary again. Notice how the $A(x, t)$ function drops to zero at the radial position where the first appearance of the horizon happens. In the same plot, we can also see the numerical noise around this point, that we consider under control as commented before.

2 The second vertical line in the inset, signals the moment when the pulse that escaped the first formation of the horizon, is just being partially absorbed in its second fall. As before, we can see in the $\rho(t, x)$ function how part of the pulse escapes the horizon. On the plot on the right we see how the $A(x, t)$ function develops a new zero at a larger radial position, this is due, as expected, to the growth of the horizon.

3 We have been able to follow this process until a third bounce where, again, the pulse is partially absorbed by the horizon and the $A(x, t)$ function drops to zero at a larger value of the radial position. However, we are still far away from the final black hole whose $A(x, t)$ function is shown on the plot on the right.

Let us comment about the numerical precision of this simulation. As shown in the figure in the inset, in every post-collapse cycle the mass suffers a 2% loss, while the grid that we used for this particular case was of 5×10^4 points. We linked the numerical noise that can be seen in the minima of $A(x, t)$ with this small mass loss.

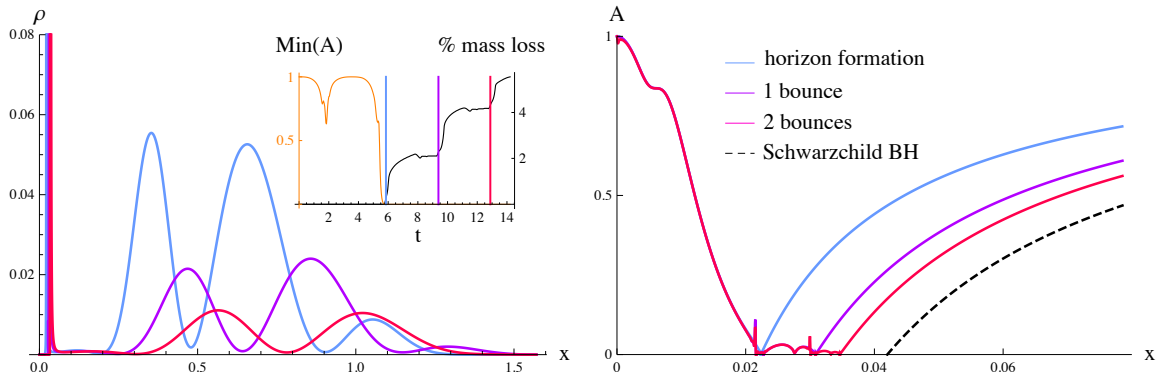

Figure 4.5: Evolution of a narrow pulse with $\sigma = 0.1$ and $M = 0.021$. Left: leftover scalar pulse after horizon formation and two post-collapse bounces. Right: horizon growth.

In general, for narrow pulses, weak turbulence dominates the two stages of the evolution and, as a consequence, some degree of radial localization is always conserved by some part of the pulse. In forthcoming sections, we will relate this effect with a stepwise relaxation process in the dual QFT.

At this point, let us begin with the analysis of **pulses of intermediate broadness**: although they are able to keep some degree of localization before the first appearance of the horizon, after it emerges, the pulse looses its radial localization and a damped quasi-standing wave sets in. Namely, while weak turbulence dominates in the pre-horizon stage, scattering among subpulses tends to control the post-horizon evolution.

As an example of a pulse of intermediate broadness, we have used an initial profile with $\sigma = 0.25$, whose results are shown in Figure(4.6). In this simulation, we saw how the first formation of the horizon occurred after two well defined bouncing cycles, in which the pulse was localized in the radial direction. Nevertheless, we see how, on the plot on the left, the $\rho(t, x)$ function (plotted in different times after the first formation of the horizon) remains delocalized in the radial direction. To see the growth of the horizon, we included the $A(x, t)$ function for the same times in the inset of this plot: new zeroes at larger values of x appear as more pulse is swallowed by the horizon. Notice that in this case we have been able to follow the simulation until the formation of the final black hole, whose horizon is given by the radius of a Schwarzschild black hole of the total mass.

Numerical simulations are more demanding for narrow pulses than for broad pulses.

That is why in this example, we where able to reach a horizon radius up to within 3% of the final value while keeping the mass loss around 0.1% using a grid with 2×10^4 points.

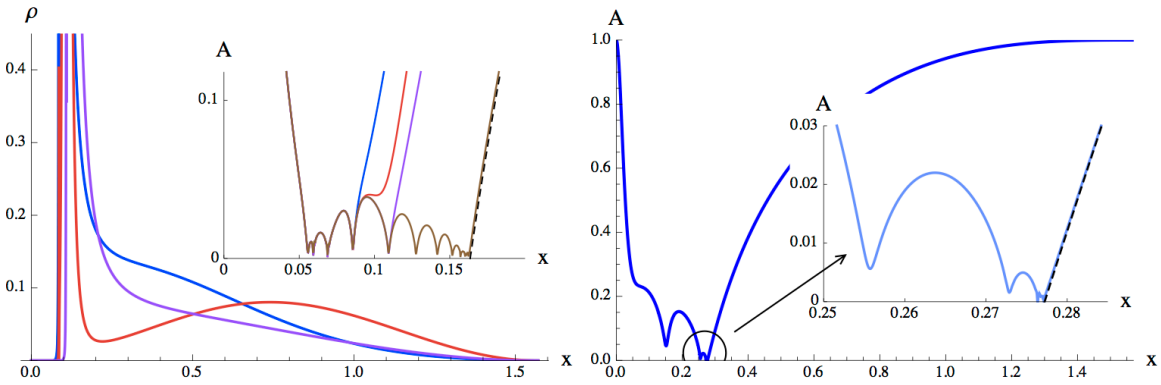

Figure 4.6: Left: cycle of the post-horizon damped wave for a profile with $\sigma = 0.25$ and $M = 0.085$. In the inset we have plotted $A(t, x)$ when the collapse process is nearly completed. The dashed black line shows $A(x)$ for a Schwarzschild BH of the total mass. Right: same plot as in the inset for a profile with $\sigma = 0.6$ and $M = 0.1538$.

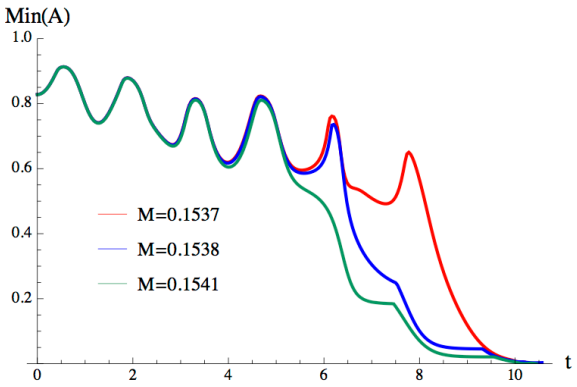

Figure 4.7: Broad initial profiles with $\sigma = 0.6$.

Now, let us comment what happens with the post-horizon dynamics of a **broad pulse**. As was advanced in the previous section, the formation of the horizon in these cases is different from narrow profiles because scattering among subpulses dominates over weak turbulence. In Figure(4.6) in the right, we see how when the $A(x, t)$ function drops to zero, it does it at a radial position very close to the final horizon radius. This is a general feature of broad pulses: contrary to narrow profiles, the horizon tends to be formed with all the mass of the pulse. Besides, in Figure(4.7),

we can see how the Min(A) of broad pulses does not abruptly drop to zero. In these cases, the horizon is formed slowly as the Min(A) decreases. This regime, where the Min(A) starts decreasing, is similar to the post-horizon dynamics of pulses of intermediate broadness we have just described. Namely, a quasi-standing wave like the one in Figure(4.6) but with a stronger damping is stablished while the horizon is slowly being formed.

4.1.4 Periodicities

In this section we will talk about the different periodicities that emerge in narrow and broad pulses during the evolution.

We have seen that only narrow pulses preserve a degree of localization during the whole evolution. This localization allows us to talk about the propagation of the pulse through the radial direction and, linked to this feature, we found well defined periodicities. Namely, narrow pulses have always a period bigger but close to π. We have checked that this periodicity increases with the mass and the broadness of the scalar profile. This period will become important in the next section, where we will relate it to "seudo particles" separating at the speed of light, without scattering, in a sphere of radius one.

When the pulse is broad enough and, therefore, it keeps delocalized the whole evolution, a shorter periodicity of $\pi/3$ emerges. It can be seen in the post-horizon stage in Figure(4.6), and in the pre-horizon part in Figure(4.7). As we have already commented, broad pulses do not present radial localization but an oscillatory pattern similar to standing waves, which seems to be the origin of this shorter periodicity. Somehow, contrary to narrow pulses, the internal dynamics of these delocalized scalar pulses determine a period of $\pi/3$. However, an immediate question arises: *Why a periodicity of $\pi/3$?*. As it is shown in Figure(4.8), broad pulses have a large overlap with the regular periodic solution found in [29], which branches out from the lowest linear "oscillon" (with constants a and α):

$$\phi^{osc}_{j=0}(t,x) = a\cos(3t+\alpha)\cos^3 x \tag{4.19}$$

Although the periodicity of this oscillon is $2\pi/3$, if we take into account the backreaction of this configuration on the metric, where the field derivatives appear squared, the resulting period is $\pi/3$.

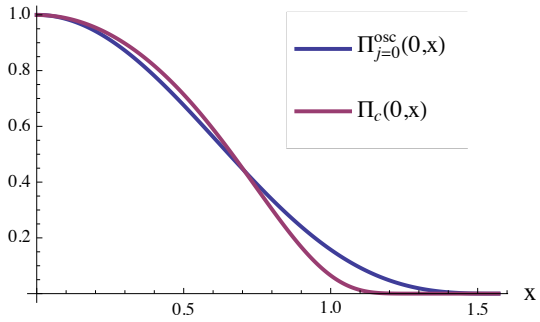

Figure 4.8: Initial data for $\Pi_c(0,x)$ with $\sigma = 0.6$ and $\Pi^{osc}_{j=0}(0,x)$ for the lowest linear "oscillon", chosen to have the same height. The overlap is susbtantial, supporting the argument that their posterior evolutions, for small amplitudes, are in the same island of stability around the (close to) $w_0 = 3$ periodic nonlinear solution constructed in [31].

4.1.5 AdS_4 vs AdS_3

In this section, we are going to compare some features of the evolution of narrow profiles in the two spacetimes described in the first section of this chapter: bouncing geometries in AdS_3 and AdS_4. Basically, we are going to analyze, for narrow pulses and for both spacetimes, if the first formation of the horizon happens at the first infall of the pulse towards the origin (direct collapse) or if in this first infall, the pulse bounces, at least once, at the origin.

As we explained in that section, there is an important difference between these two spacetimes that totally constrains the formation of the first horizon. In AdS_4 static black holes can exist with any mass (depending on the mass we will have a large or a small black hole), but in AdS_3, there is a mass threshold below which the singularity is not covered by a horizon [66], namely, we have static solutions that are naked singularities. For the choice of unit circle we made in previous sections, this mass threshold for AdS_3 static solutions is:

$$\mathcal{M} = 1 \tag{4.20}$$

The existence of this naked singularities in AdS_3 has an important effect in the collapse process. If the initial condition that we choose has a total mass below this threshold, then the eventual collapse could only end up forming a singularity that is not hidden by a horizon. We did not see this in our simulations. In fact, no matter how far we pushed our programs, we never saw any chance of a dynamic formation

of a naked singularity. Instead, when we chose an initial profile of this type, what we saw was a series of bounces that did not seem to end. These results are in agreement with the singularity analysis of [34] which point towards excluding the formation of these singularities in finite time.

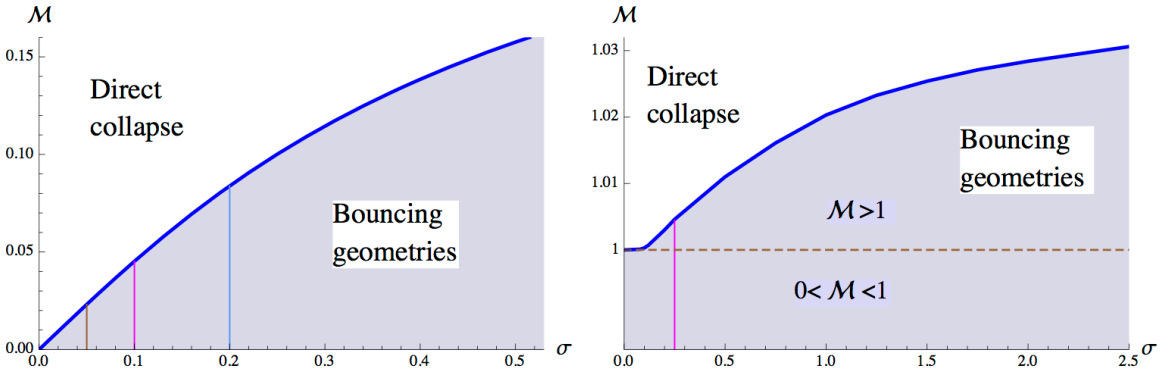

Figure 4.9: Left: Phase diagram for scalar collapse with gaussian initial data in AdS4. The shaded region signals processes requiring at least one bounce for collapse. Right: Phase diagram for scalar collapse with gaussian initial data in AdS3.

This threshold for the direct formation of a black hole in AdS_3 can be explicitly seen in Figure(4.9). If we compare the curve separating direct collapse from bouncing geometries in AdS_3 and AdS_4, we clearly see how bouncing geometries exist in AdS_3 for much higher energy densities[3].

4.2 QFT interpretation: Revivals

With all this information we have given about the gravity side, let us now move to the interpretation in the dual QFT. In this section, we will explain how to understand these dynamics from the dual side, and in the next section, we will support this interpretation with the behavior of the entanglement entropy.

Before directly starting with the QFT explanation, we need to gain some intuition from previous works. In particular, we are going to briefly comment the results of [61] where the behavior of the entanglement entropy obtained by Cardy and Calabrese in [1] (where they studied a quantum quench from a gapped to a critical system in 1+1 dimensions) is, essentially, holographically reproduced.

[3]This is related to the mass threshold below which collapse has not been found.

To summarize, what was done in that work, was to compute the HEE in a grav-

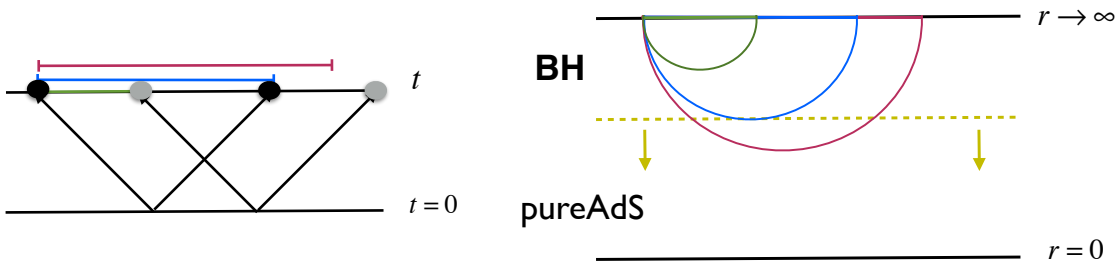

Figure 4.10: In the right a schematic picture of the geodesics in the gravity spacetime while the shell is falling from the boundary, in the left the regions for which the EE is given by the length of the corresponding geodesics in the right. Two pairs of entangled excitations are shown in the left.

ity background where a black hole was formed by the collapse of a null dust shell in an asymtpotically AdS_3 spacetime (Vaidya model). The entanglement entropy of an interval in the QFT side (which was an infinite spacetime of dimension $1+1$), was given by the length of the bulk geodesic that anchors at the AdS boundary on the interval endpoints. A very schematic picture of what goes on in that model is given in Figure(4.10). Notice that for small enough intervals or late enough times, geodesics lie outside the infalling shell [61]. Since this part of the geometry is that of a BTZ black hole, the entanglement entropy for such intervals will be the same as that of a thermal state. The bound $t = l/2$ (when the EE saturates, see Section(3.2.1)) corresponds to geodesics whose central point just reaches the infalling shell [61, 67]. We are thus led to propose a meaning for the position of the pulse in the radial direction: it captures the typical separation of entangled components of the QFT wavefunction. When the pulse is close to the boundary entanglement is to be stronger between nearest neighbors, whereas the pulse falling towards the origin of AdS should represent entangled excitations flying apart. Analogous arguments were used in [70] to construct a holographic model for a local quench.

With this recently gained intuition about the relation between the position of the shell and the minimal scale at which we find entanglement, it is much easier to move to the QFT interpretation of the bouncing geometries we have just studied. As in the previous works we have commented, the observable we have monitored in these geometries is the entanglement entropy, and we will see in the next chapter how, from

its behavior, we can deduce the presence of revivals in the system. Besides, we will also define the revival time t_{rev} that depend on the energy and the dimension of the space[4].

4.2.1 Propagation model for entanglement

We have just commented how the propagation model for entanglement, proposed by Cardy and Calabrese, was successfully reproduced holographically. While there, the QFT was living in an infinite spacetime, in our case the system is finite size. A natural question would be: *Can the propagation model still be applied to Finite Size Systems?*. This is analyzed in this section where we study the particular case of a CFT living in a circle (and a sphere, in the higher dimensional case) that evolves in time.

We have a compact system like the one in Figure(4.11), suddenly we perturb it creating a non zero energy density. As before, this energy density can be thought as distributed in excitations all along the QFT space. Accordingly to the simplified model of Cardy and Calabrese, these excitations would move at the speed of light and without scattering. For simplicity, we focus just on two of these excitations and describe its evolution in three steps (a pictorial representation of the steps is shown in Figure(4.11)):

1 At the beginning, these excitations start to separate without noticing that they are living in a compact space, this corresponds to an uniform increase of the EE. In the gravity side this maps to the fall of the shell towards the origin, everything as in the non compact case.

2 When the excitations achieve their maximal separation, the situation is very different from the infinite case where they always move apart. If the simple propagation model would apply to the compact case, these excitations will start to join again in the circle (or sphere). However, we have seen that this only happens at low energies[5]: if the energy is high enough, fast thermalization will occur as we may intuitively expect in an interacting quantum field theory. In the gravity description, the moment at which these excitations are maximally separated, corresponds to the pulse being localized at the origin and, consequently, fast thermalization maps to the formation of the black hole, with all

[4]We will focus on narrow profiles.

[5]In previous sections we have seen that for $\mathcal{M} \gg 1$ direct collapse occurs.

the mass, in the first infall of the shell towards the origin. The formation of a horizon can be understood, in the QFT part, as an irreversible dephasing of some degrees of freedom.

3 As we have already advanced, we will see that if the energy is small enough, the simple propagation model applies and the transition between step two and three is smooth: excitations keep moving at the speed of light until reaching again its initial position (1), where the Revival occurs. Notice that with the propagation model, we would have an infinite series of revivals happening always with a difference of time $\Delta t = L/2c$, where L would be the length of the circumference and c the speed of light. If we choose the radius of the sphere to be one and set $c = 1$, then we would have $\Delta t = \pi$. Besides, we have seen that excitations moving apart correspond, in the holographic side, to the shell falling towards the origin, therefore, it is natural to propose that excitations joining again is dual to the shell coming back from the origin to the boundary. As advanced, bounces of the shell in the origin are, in this setup, necessary to have Revivals in the QFT side. As it is shown in Figure(4.11), in this step the EE decreases until reaching its initial value.

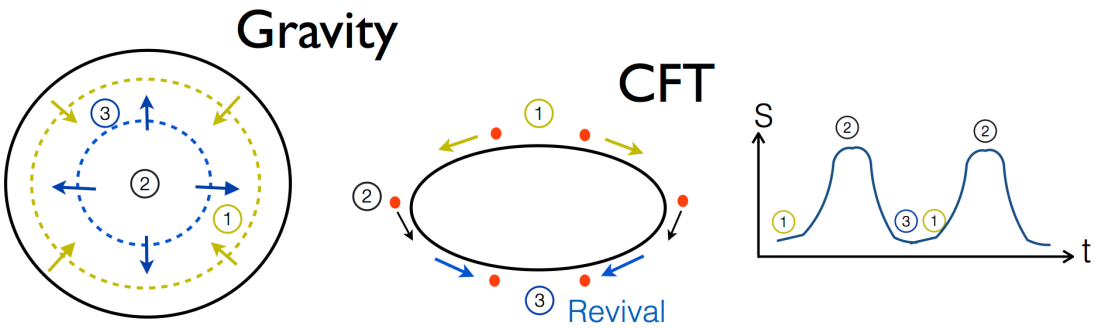

Figure 4.11: Scheme in three steps of the relation between the dynamics in the gravity side, the kinematics of the entangled excitations in the CFT, and the time evolution of the entanglement entropy.

In the forthcoming sections, we will see what is the scenario that occurs and how it depends on the energy density of the perturbation. We will also study how the broadness of the shell affects the evolution of the system, and how we can interpret it in the QFT side.

Although, as advanced, the simple propagation model will apply only for very small energies, we will also show that, for narrow shells, the variations of the entanglement

entropy can always be explained with this simplified model.

At this point, let us remember that, in the gravity side, the initial data for the time evolution was set by defining a gaussian profile in the time derivative of the scalar field, and setting to zero its spatial derivative. To translate this perturbation to the QFT language, we can use the quantity $\rho(t, x)$ which, in the gravity side, was the radial energy distribution of the shell. We will see that, for narrow pulses, this relation can give some insight about the kind of perturbation done in the QFT.

First, let us propose to relate the broadness of $\rho(t, x)$ to the scales at which we simultaneously find entanglement in the QFT (see Figure(4.12)). Let us imagine the initial profile of $\rho(t, x)$ at $t = 0$ as made of many very narrow profiles in the way it is signaled in Figure(4.12). The blue and red shaded regions would be two of these very narrow profiles. In the propagation picture of entanglement we have just described, the blue/red shaded profile is indicating, in the QFT side, some amount of entangled excitations at the blue/red scale (see picture on the right of the same figure). In this way we picture how, in this model, the broadness of the profile is connected with the different scales at which we find entanglement in the dual theory. A very narrow profile would be understood as having one dominating scale that changes in time.

The connection with the time span of the perturbation is also understood along these lines. If we have entangled excitations at the blue/red scale, is because they have been created in a previous time $t < 0$ and they have been moving since then. This is shown in the picture on the right of Figure(4.12). As we are assuming that these excitations move at the speed of light, we can conclude that the time at which they were created is:

$$t \sim x - \pi/2 \leq 0 \tag{4.21}$$

where x is its radial position at $t = 0$. Notice that if all of them are located at the boundary, namely we have an initial very narrow profile located $x = \pi/2$, the excitations must have been created at $t \sim 0$, meaning that the time extent of the perturbation in the QFT side is almost zero.

Notice that in this simplified model, we have connected propagation of entanglement in the QFT with propagation of the profile in the radial direction. However, as we have studied before, this relation can be applied to narrow pulses of low mass, but it is not a good description for broad pulses which behave as standing waves. That

is why this connection between broadness of $\rho(t,x)$ and timespan of the perturbation in the QFT, can give some intuition only when the profile propagates in the radial direction (one case would be narrow profiles of low mass).

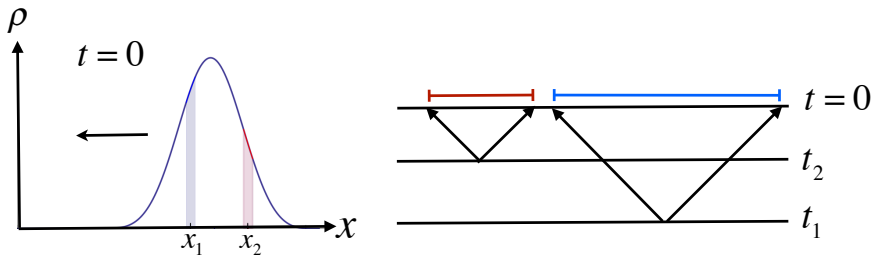

Figure 4.12: Scheme of the relation between the broadness of the profile ρ and two related parameters in the CFT: time span of the perturbation and the scales at which there is entanglement.

To check in a quantitative way the connection between the time span of the perturbation in the QFT side and the broadness of the profile we are going to use the Vaidya geometry in AdS_4, where we actually have control on the time extent of the perturbation in the gravity side. The metric we are going to use is:

$$ds^2 = \frac{1}{\cos^2 x}\left(-\left(1 - m(v)\frac{cos^2 x}{\tan x}\right)d^2v + 2dvdx + \sin^2 x d\Omega_2^2\right) \tag{4.22}$$

where v is an Eddington-Finkesltein infalling coordinate.
As explained in previous sections the mass function $m(v)$ that we defined as:

$$m(v) = \begin{cases} 0 & v < -\Delta t \\ M & v > 0 \end{cases} \tag{4.23}$$

generates an energy density $\mathcal{M}$ in a time span Δt. To see the growth of the broadness of the pulse in the x,t coordinates, we can use Figure(4.13) on the left, where we see how the t = cte slices intersect the shell (which is signaled in yellow in the figure). Namely, as the pulse enters from the boundary into the bulk, it acquires a certain broadness. In Figure(4.13) on the right, we can directly see the evolution of the pulse in the x,t plane for $t \geq 0$.

4.3 Time evolution of Holographic Entanglement Entropy

As was explained in the corresponding section, to compute the HEE of a given region A in the QFT space, we have to find the extremal surface γ_A which anchors at the

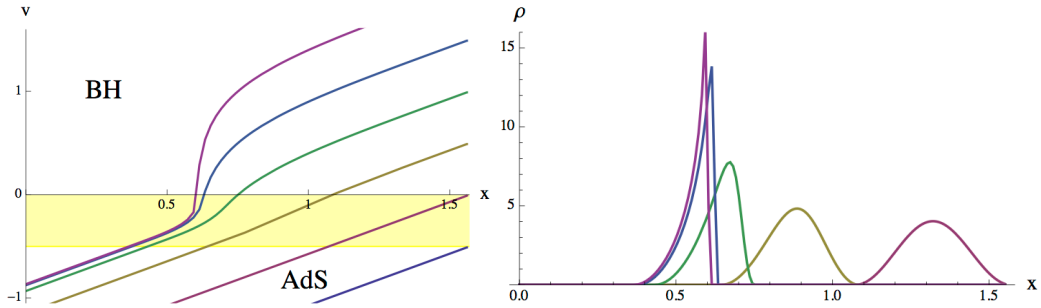

Figure 4.13: Left: intersection a null dust shell with $\Delta = 1/2$, signaled in yellow, with the lines of constant $t = -0.5, 0, \ldots, 2$ in the (v, x) plane. Right: mass distribution function at the same t slices.

boundary of A and lives in the AdS spacetime [37, 39]. Then, the EE is given by the area of this surface divided by a factor $4G_N$, where G_N is the Newton constant.

4.3.1 Computation of Holographic Entanglement Entropy

In the particular case of the asymptotically **AdS4** spacetime we have been using, the initial data and the full time evolution respect spherical symmetry. To simplify the computations we focused on finding γ_A surfaces that preserve this symmetry, so that they could be found as surfaces of revolution parametrized by just one coordinate θ (notice that θ is a polar angle in the boundary of the spacetime, that in this case is $R \times S^2$).

Therefore, with this setup, we just have to find the functions $x(\theta), t(\theta)$ that extremize the length functional and fulfill the boundary conditions:

$$x(\theta_0) = \pi/2, \qquad t(\theta_0) = t_0, \qquad x'(0) = t'(0) = 0 \tag{4.24}$$

where θ_0 is the angular aperture of the spherical cap in the boundary. In other words (and in the QFT side), we are computing the EE of spherical caps of angular aperture θ_0.

As we have already seen, the EE is a divergent quantity that we have to regularize. In this case we do it just by substituting the area of γ_A, namely Area(γ_A), by:

$$L_A = \text{Area}(\gamma_A) - \text{Area}(\gamma_A^{pureAdS}) \tag{4.25}$$

Where we have substracted to the infinite quantity Area(γ_A) the area of the surface $\gamma_A^{pureAdS}$, which is a surface with the same boundary conditions as γ_A but in the pureAdS spacetime. By doing this we obtain the finite quantity L_A. [6]

[6] This is because both spaces are asymptotically AdS, namely, they are equal near the boundary where the divergence happens (the divergence in the EE is a UV divergence)

The area of the surfaces $\gamma_A^{pureAdS}$ has been computed analytically [71]:

$$\text{Area}(\gamma_A) = 2\pi \left(\frac{\sin\theta_0}{\epsilon} - 1 \right) \tag{4.26}$$

Where $\epsilon = \cot x_M$ with $x_M \lesssim \pi/2$, is a radial cutoff to regularize the divergence. Therefore the regularized entanglement entropy is given by [68]:

$$S(t,\theta_0) = \frac{\pi}{2G_4} \left(\frac{\text{Area}(\gamma_A)}{2\pi} - \frac{\sin\theta_0}{\epsilon} \right) \tag{4.27}$$

In the case of the asymptotically **AdS3** spacetime we have studied, we follow a similar approach. Now, the QFT lives in a $S \times R$ spacetime and the surfaces A for which we have computed the EE are segments in the circle parametrized by the angular coordinate $\theta \in [0, \pi]$ (where $\theta = \pi$ corresponds to the semicircle).

Now that we know how to regularize the areas and which surfaces we have used to compute the EE in the QFT side, we can analyze the results in the two spacetimes we have been working on.

4.3.2 Universal fall of the pulse

In this section we analyze the early time dynamics of the EE, namely, its evolution during its first infall towards the origin (the pulse always stars at the boundary). We will see that, both in AdS_4 and AdS_3, narrow pulses have a universal behavior in the sense that its first infall seems to be well described with the propagation model of entanglement.

First, let us analyze the **time evolution of $S(t,\theta)$ in the first fall of the pulse towards the origin in the AdS4**[7] case. To this aim, we have selected an initial configuration with a quite narrow profile, with $\sigma = 1/16$, and we have studied it for different initial masses (Figure(4.14)). It seems that our results are consistent with the propagation model of excitations we explained. Let us see it explicitly.
In this figure, in the picture on the left, we compare the evolution of one pulse that creates a BH in the first fall towards the origin ($M = 0.3$), and one that bounces three times before forming a horizon ($M = 0.012$). To compare the time evolution of the EE we have rescaled one of them so that they coincide at its maximum. Notice that, although we have changed the mass by one order of magnitude, both evolutions are

[7]Here, by AdS we mean asymptotically AdS.

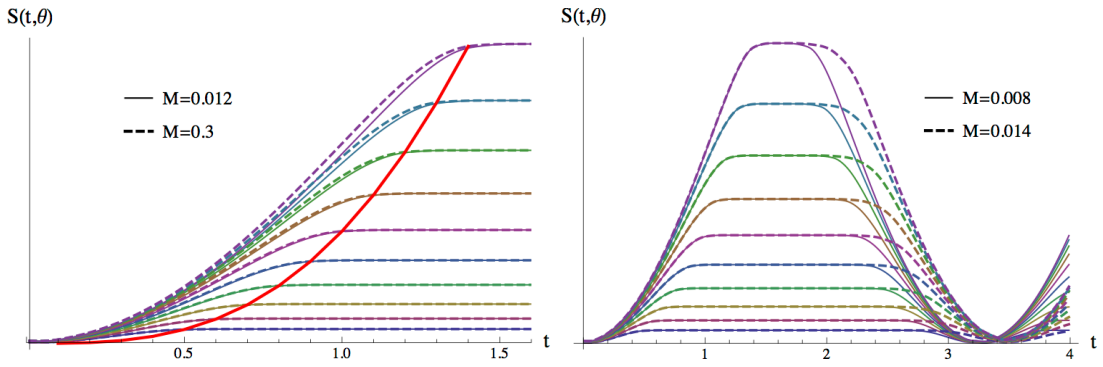

Figure 4.14: EE evolution for several pulses with $\sigma = 1/16$ in AdS4. Different colors correspond to caps with $\theta = .5, .6, .., 1.4$. In each graph, the EE values for the lower mass pulse have been rescaled to coincide with those of the larger mass one at their maxima for the sake of comparison. The red line on the left figure gives, for the pulse with larger mass, the EE at $t = \theta$.

quite similar. Besides, they reach its maximum at $\theta = t$ (see red line in the graph), as corresponds to excitations flying at the speed of light (notice that $c = 1$ and the radius of the sphere has been set to one).
In the same figure but in the picture on the right, we compare an initial configuration that bounces just once ($M = 0.014$) with one that bounces many times before forming a horizon ($M = 0.008$). In this case the agreement of both evolutions (taking into account that, as in the previous case, we have rescaled the EE to make them coincide at its maximum) is very good, in fact, it is difficult to distinguish both curves.

A similar behavior is obtained in AdS_3 (see Figure(4.15)). Notice that, in this dimensionality, the pattern is sustained over long cycles.

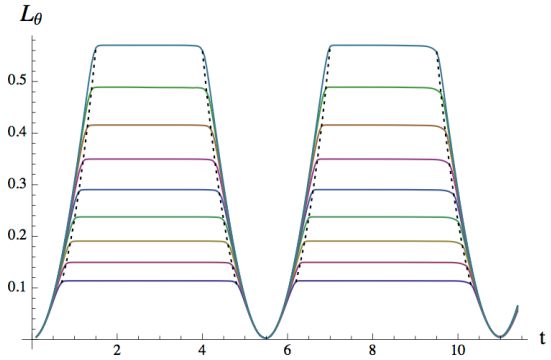

Figure 4.15: Same as in Fig(4.14) for an AdS_3 shell with $\sigma = 0.05$ and $\mathcal{M} = 0.68$.

4.3.3 Revival and Dephasing Time

Let us begin this section by talking about the **plateau** that can be seen in the EE in Figures (4.14) and (4.15). It is formed because, when a narrow pulse reaches the origin, it does not instantly leave it but it can spend there a time δt. Notice that, this time, cannot be explained with the intuitive propagation model for entanglement we described in previous sections. In Figures (4.14), (4.15) and (4.18), both in AdS_3 and AdS_4, it can be seen that δt grows with the mass allowing us to identify it with an interaction effect. As was explained in previous sections, the propagation model for entanglement only applies for small energy densities, namely, when $\delta t \to 0$.

Related to this plateau effect, let us analyze the time at which the initial value of the EE is recovered. In the QFT side, we interpret this time as a **revival time** that we denote by t_r. If the simple propagation model would apply for all energy densities, t_r should be always equal to π, because $R = 1$ and the propagation velocity is $c = 1$, so that $t_r = 2\pi R/2c = \pi$. In both cases, AdS3 and AdS4, we found that this revival time was always above π as expected from Section 4.2.1: as we increase the energy density, the narrow pulse spends more time at the origin, the plateau of the EE grows and, as a consequence, t_r grows. Therefore, as we did with the plateau, we can relate the delay in t_r with the presence of interactions in the system. In Figure(4.16), in the upper part, we show several examples where we have computed the variation of t_r with $\mathcal{M}$ at a fixed σ for both dimensions. In Figure(4.16), down, we show a similar plot but in this case we maintain fixed the mass and vary σ. We find four remarkable features, the first two of them confirming what we have just described:

1. $t_r \gtrsim \pi$.
2. We observe that, as the mass is increased, t_r grows.
3. If we do not vary the mass, we can see that, as the broadness of the pulse grows, t_r decreases.
4. In AdS3 we can reach much longer revival times than in AdS4.

We actually found that point four is a general result: while in AdS4 t_{rev} is always of the order of π, in AdS3 we can reach much longer revivals times. What actually happens in the AdS4 case is the following: we already know that to have bounces we need very low masses in comparison with the AdS3 case (see Figure(4.9)), therefore, when we try to reach larger revival times by choosing larger masses, we just destroy

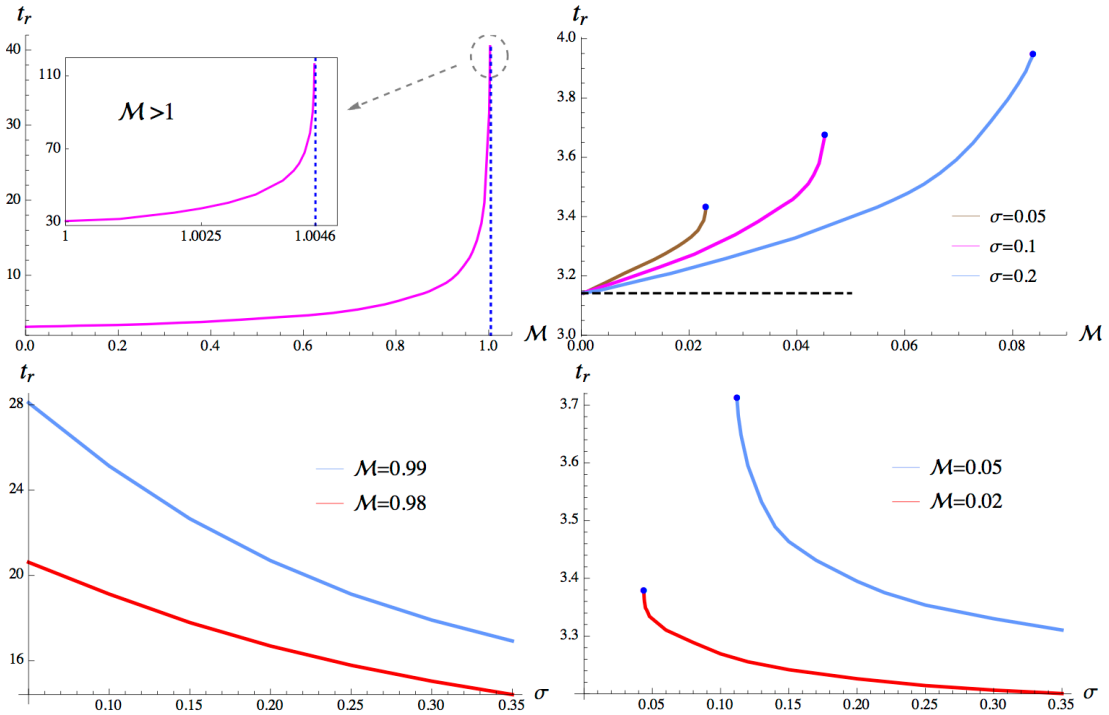

Figure 4.16: Left Up: Mass dependence of t_r for initial pulses (4.12) with $\sigma = 0.25$ in AdS_3. In the inset, detail of the plot in the small window above threshold compatible with bounces. The apparent change of slope is due to the rescaling of the vertical axes. Right Up: Dependence of the bouncing period with the mass for fixed $\sigma = 0.05, 0.1, 0.2$. The blue dots signal the threshold value for direct collapse. The dashed line is $\tau = \pi$. Left Down: Variation of t_r with σ for AdS_4 pulses of fixed mass $\mathcal{M} = 0.02, 0.05$. The blue dots signal the threshold value for direct collapse. Right Down: Variation of t_r with σ for AdS_3 pulses of fixed mass $\mathcal{M} = 0.98, 0.99$.

the bounces pattern and find a direct collapse. The other option would be to try to increase the broadness of the initial profile. What happens when we try with this option is shown in Figure(4.17), where we see how, although the revival pattern is somehow conserved, the oscillation pattern gets complicated and the plateau is no longer well defined.

Although we have already talked about the universal behavior of the EE in the first fall of the pulse towards the origin, we can stress more in this direction and analyze the universality, in both dimensions, of the time that the relativistic excitations take to reach their maximum separation (step 2 of Figure(4.11)). We call this time the **dephasing time** t_{deph} and, as we are dealing with a relativistic model, it should be

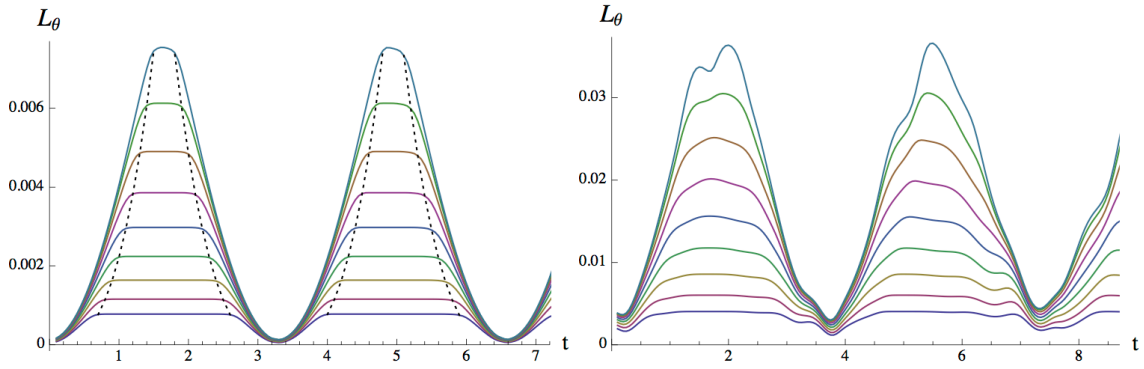

Figure 4.17: EE evolution of spherical caps with $\theta = 0.7, .., 1.5$ in two AdS_4 processes which bounce twice before collapse. Left: Scalar profile with $\sigma = 0.05$ and $M/M_* = 0.02$. The dotted lines signal $t = \theta, \tau - \theta, \tau + \theta, 2\tau - \theta$. Rigth: $\sigma = 0.5$ and $M/M_* = 0.12$.

equal to $\pi/2$:

$$t_{deph} \approx \frac{\pi}{2} \tag{4.28}$$

In the QFT part the dephasing time would be the time at which the system seems thermal to the observable we are computing, namely, the entanglement entropy reaches its thermal value at t_{deph}.

Although t_{deph} is equal for AdS3 and AdS4, there is a very different feature that we can just see in the first case: t_{rev} and t_{deph} can be so different that we can talk about an emergence of two different scales. This is not the case in AdS4 where $t_{rev} \sim 2t_{deph}$. Notice that this difference can be understood by relating it with the symmetries of each system. In the AdS3 case they are stronger, and therefore, the dynamics is more constrained.

In Figure(4.18) we show the emergence of these two scales in the AdS3 case. How tunable is t_{rev} is explicitly shown in this graph, where we see how the plateaux grows with the mass. There, we can also see the universality of t_{deph} by noticing how the EE reach the thermal value at the same time for all configurations. From the gravity side the time extent of the plateaux is related to the time the pulse spends at the origin trapped in its own gravitational potential.

The fact that t_{deph} is a universal magnitude for narrow pulses, means that, in these cases, the propagation model for entanglement describes quite well the evolution until the excitations reach its maximal separation (see Figure(4.11)). In fact, in Figure(4.19) we see that, not only t_{deph} is universal but that the time Δt in which the EE varies (leaving its thermal value, reaching the vacuum result, and coming back

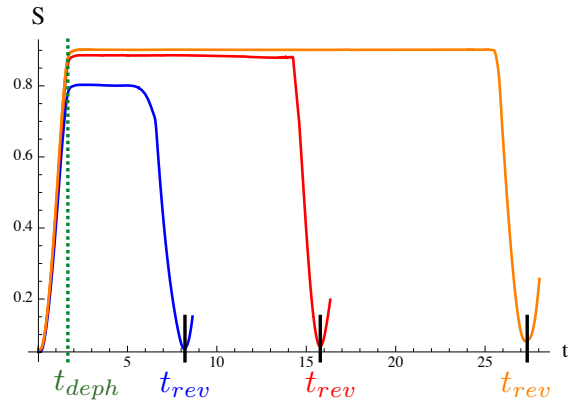

Figure 4.18: Entanglement entropy of an interval with $\theta = 3.14$, almost a semicircle, along the first bouncing cycle of AdS_3 shells with $\sigma = 0.25$ and $\mathcal{M} = 0.88, 0.98, 1, 1.003$.

again) maintains along time. We have checked with other simulations that this time Δt is always equal to π.

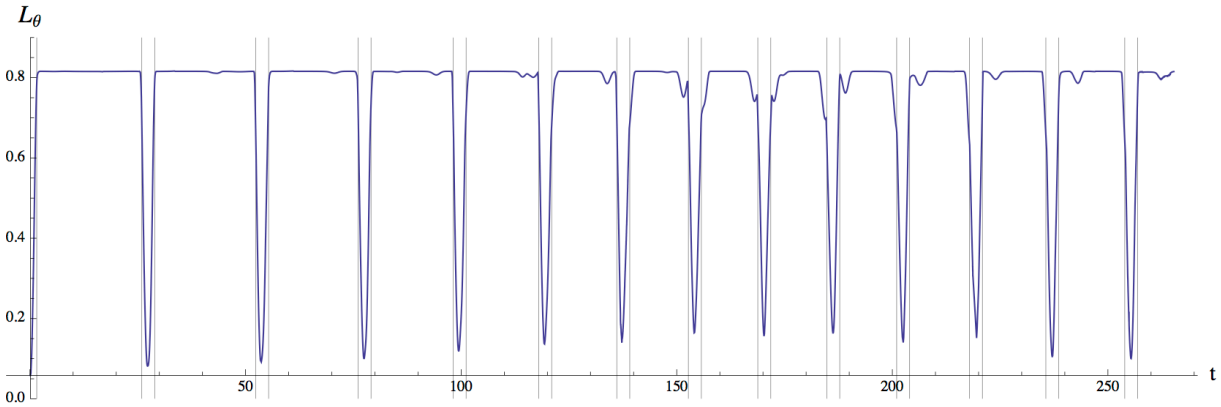

Figure 4.19: Entanglement entropy evolution for $\theta = 3$, in a AdS_3 process with $\sigma = 0.25$ and $\mathcal{M} = 1$. The vertical lines mark equal intervals whose extent is $\Delta t = \theta$, except for the first line that is located at $t = \theta/2$.

4.3.4 Collapse and Revival in Quantum Systems

In the previous section we have shown how, in the low dimensional case and for narrow pulses, t_{rev} grew with the energy density of the system and t_{deph} was a universal magnitude. In this subsection we present two QFT systems that have a similar phe-

nomenology.

First, let us comment about a **Bose-Einstein condensate of atoms in an optical trap**. We focus on [72], where the behavior of a condensate of atoms with repulsive interactions trapped in a 3-dimensional confining potential, was studied experimentally. There, the repulsive interactions where reasonably described by the simplified hamiltonian:

$$H = \frac{1}{2}U\hat{n}(\hat{n}-1) \tag{4.29}$$

where $\hat{n}$ counts the number of atoms.
If the system is prepared in the following coherent state (where α is a complex number):

$$|\alpha(t)\rangle = e^{-\frac{|\alpha|^2}{2}} \sum_n \frac{\alpha^n}{\sqrt{n!}} e^{-\frac{1}{2}Un(n-1)t}|n\rangle \tag{4.30}$$

it is easy to see that the state is reconstructed at every $t_{rev} = 2m\pi/U$, where m is an integer.
Now that we know that the system has revivals, let us see how we can define the dephasing time t_{deph}.
The matter wave field of the condensate is defined by $\Psi(t) = \langle\alpha(t)|a|\alpha(t)\rangle$, its mean value represents the fraction of individual atoms that are coherent over the total number of atoms in the trap. If we compute it in the previous state we obtain:

$$\Psi(t) = \alpha e^{-|\alpha|^2(1-\cos Ut)} e^{i|\alpha|^2 \sin Ut} \tag{4.31}$$

As it is shown in Figure(4.20) this observable is exponentially suppressed at $t_{deph} \approx \pi/U|\alpha|$. This is how, in this setup, we define the dephasing time: the time at which the state almost does not have individual atoms coherently related.
The quotient between the revival time and the dephasing time is given by:

$$\frac{t_{rev}}{t_{deph}} = 2\sqrt{\overline{n}} \tag{4.32}$$

where $\overline{n} = |\alpha|^2$, which is the average number of atoms.
This results is qualitatively similar to the one we have obtained in the holographic setup, in the low dimensional case.

Another model that shows similarities with our holographic computation is the **Jaynes-Cummings** model [73], that describes the behavior of a two level atom in a cavity

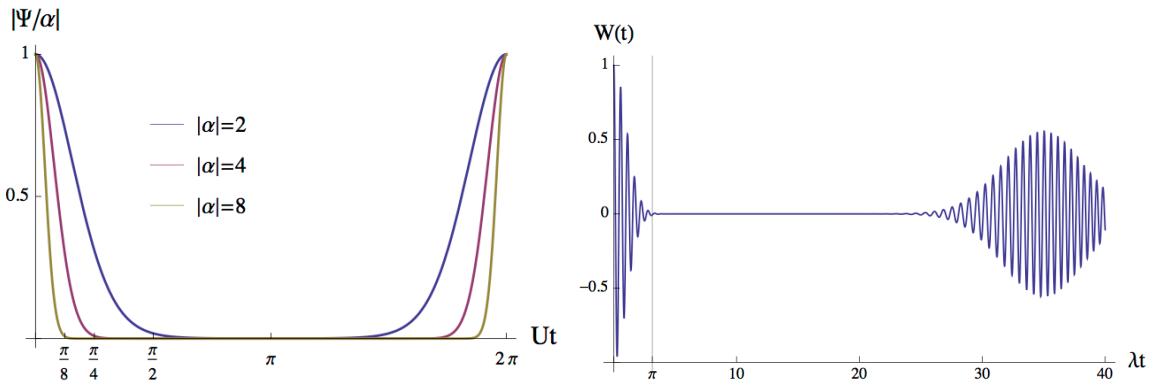

Figure 4.20: Left: Evolution of the matter wave field along a revival cycle for several values of α. Right: Evolution of $W(t)$ for $\alpha = 30$. The vertical line signals the collapse time $\lambda t_c = \pi$.

coupled to quantized radiation. The hamiltonian of this system is:

$$H = w(\sigma_3/2 + a^\dagger a) + \lambda(\sigma_+ a + a^\dagger \sigma_-) \tag{4.33}$$

where $a^\dagger, a$ are the photon creation and destruction operator, and $\sigma_{3,\pm}$ the Pauli matrices referring to the two level atom. The state that we analyze here, is the one where the radiation field starts in a coherent superposition of states of different number of photons, and the atom is in the excited state $|+\rangle$. Namely:

$$|\Psi(t)\rangle = e^{\frac{-|\alpha|^2}{2}} \sum_n \frac{\alpha^n}{\sqrt{n!}} \left(\cos(\lambda\sqrt{n+1}t)|+\rangle|n\rangle - i\sin(\lambda\sqrt{n+1}t)|-\rangle|n+1\rangle\right) \tag{4.34}$$

In this case, both the revival time, t_{rev}, and the dephasing time, t_{deph}, are defined on the observable $W(t) = |\langle+|\Psi(t)\rangle|^2 - |\langle-|\Psi(t)\rangle|^2$, that is the probability of finding the atom in the excited state minus that of finding it in the ground level. Although it starts being one, it becomes exponentially suppressed at $t_{deph} \approx \pi/\lambda$, and it is not until $t_{rev} \approx 2\pi|\alpha|/\lambda$ that we find the initial value partially reconstructed (see Figure(4.20)).

In this model the similarities with the holographic computation are deeper, not only Eq(4.32) is fulfilled[8], but also t_{deph} is a universal value determined by the properties of the system (it does not depend on the initial state), and t_{rev} grows with the energy.

[8]As before $\overline{n} = |\alpha|^2$ is the average number of photons in the system.

4.3.5 Evolution of EE along several cycles

In this section, we show a detailed analysis of the EE behavior in the asymptotically AdS_4 spacetime we have explained in previous sections. Basically, we compare the specific features of the evolution before the first appearance of the horizon (pre-horizon evolution) with what happens after that (post-horizon evolution). We present this last analysis for three pulses of different broadness.

Pre-horizon evolution

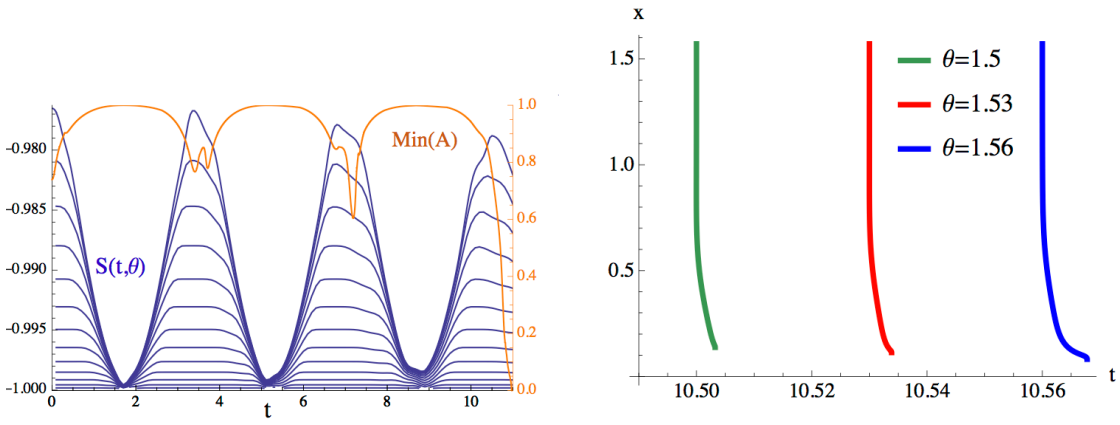

Figure 4.21: Scalar profile with $\sigma = 0.1$ and $M = 0.012$. Left: Evolution of the EE for caps with $\theta = .5, \ldots, 1.5$. We have superposed in orange the minimal radial value of $A(t, x)$. Right: Projection on the (t, x) plane of the surfaces responsible for the EE maxima of large caps in the last bouncing cycle before de horizon forms.

Let us start by explaining the results of the **pre-horizon stage** of the narrow pulse. To this aim we have included Figure(4.21) on the left, which exemplifies quite well the features we are going to comment.

One of the first things that we notice, is that the maxima of the EE shown in Figure(4.21) on the left, decrease in each bouncing cycle. Although this EE was obtained for a particular narrow pulse, we found that this **decreasing of the EE maxima** is a general feature of narrow pulses. To understand this effect, we have to recall the dynamics of narrow pulses: in each bouncing cycle, part of the profile sharpens while the rest increases its radial dispersion, constraining the shape of the extremal surfaces that we need to compute the EE. What happens is that, at each successive bounce, these surfaces intersect a growing and more spread fraction

of the scalar pulse, causing a decreased in the area which is what we clearly see in Figure(4.21). The fact that the maxima of the EE decrease in the way we have described, do not seem to agree with the proposal of [60] where the EE was understood as a croase grained entropy. We may have expected that, in spite of the oscillations, at least the maxima of the EE monotonically increase during the evolution, conserving some notion of coarse grained entropy. We found that not even this is true for narrow pulses.

The next effect we are going to comment can also be seen in Figure(4.21) on the left, and is related to the subtle **lack of synchronization between the minima of A and the maxima of the EE**. First, notice that the surfaces that we used to compute the EE do not necessary lie in slices of constant t, therefore, to talk about "synchronization" we first need to know how deep in t the extremal surfaces have reached. In Figure(4.21) on the right, we see that these surfaces hardly move in t, namely, "synchronization" has a meaning in this situation. Once we have solved this issue, we can come back to the original question. The reason for the lack of synchronization between the minima of A and the maxima of the EE is that the t slice at which the EE surface maximizes its area is not synchronized with the moment at which the localized part of the shell is at its closest approach to the origin, which is what the minima of $A(x,t)$ measures. Notice that the EE surfaces, look for an extremal area by a competition of two contrary effects: reaching deep in the bulk and keeping outside the traveling and well localized part of the shell.

For the sake of completeness, we can comment some more features about the EE extremal surfaces with respect to the t slicing. We stress three points:

- As long as the extremal surfaces do not touch the scalar shell, they live on constant t slices.
- If the pulse is falling towards the origin, and a part of the extremal surface intersects it, then this part deviates from constant t to smaller values of this coordinate.
- If the pulse is coming back to the boundary, and a part of the extremal surface intersects it, then this part deviates from constant t to bigger values of this coordinate.

Post-horizon evolution

At this point, we move to analyze the **post-horizon dynamics of narrow pulses**. To this aim we include Figure(4.22) where we show the evolution of the EE before and after the first formation of the horizon (notice that the case we show in this figure is the same of Figure(4.21)). In order to complete the five post-horizon cycles with a total mass loss below 3%, we had to use a grid up to 7×10^4 points.

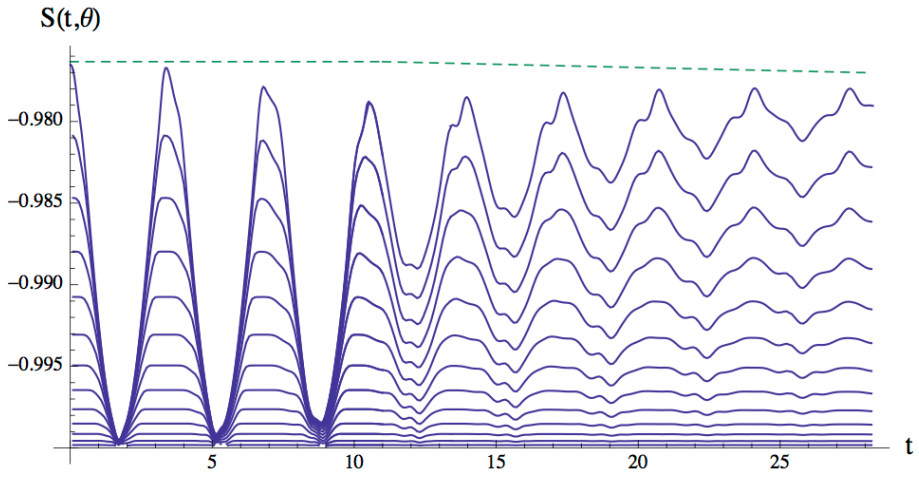

Figure 4.22: Post-horizon evolution of the EE for the same case plotted in Fig.4.21. The time for the first collapse is $t_h \sim 11$, and at around $t = 28$ the horizon radius is 83% of its final value. The green line gives $S(\theta = 1.5)$ for a static black hole of the total mass, where we did have into account the numerical mass loss along the evolution.

In this second stage, the horizon is already formed and it grows by trapping a fraction of the scalar pulse in each cycle. This growth is reflected in the **decreasing of the oscillations amplitude**, as there is less scalar profile bouncing. Besides, **the minima of the EE grow in each cycle**, approaching the thermal value of a static black hole with all the mass[9]. Contrary to what happens in the pre-horizon stage, after the formation of the horizon the maxima of the EE monotonically increase towards the final thermal value. This value is shown with a dotted green line in Figure(4.22) for EE of a $\theta = 1.5$.[10]

Besides, although this pulse keeps a periodicity of π during the whole evolution, in the post-horizon stage, we can start to see a slight emergence of a $\pi/3$.

[9]We can understand this in this simplified version because the extremal surfaces we need to compute the EE, never crossed the horizon in this closed system.

[10]It decreasing its due to the mass loss in the numerical computation.

Notice that this pulse keeps radial localization along the first five post-horizon cycles. Following the argumentation of previous sections, this suggest that while part of the system dephases in correspondence with the appearance of an apparent horizon, part of it still retains quantum coherence. Moreover, a typical separation could be associated to the remaining entangled degrees of freedom, linked to the radial position of the pulse. Thus, a pattern emerges in which the system undergoes a **stepwise loss of quantum coherence**, triggered by the dephasing of a subset of the degrees of freedom.

Let us start with the analysis of the **intermediate broadness pulse** ($\sigma = 0.25$). From previous lines (see Figure(4.6)) we know that this pulse keeps radial localization during the pre-horizon stage, while in the post-horizon stage the dynamic is the one of a quasi-standing wave. This is clearly distinguished by the **entanglement entropy periods** (see Figure(4.23)), which change from approximately 4.5 units (above π) before the horizon formation at $t_h \approx 9.7$, to oscillations of a periodicity close to $\pi/3$ in the post-horizon part. But these are not the only periods we can differentiate in the evolution, it is interesting to notice the existence of a modulating period of $\pi/3$ in the pre-horizon stage, which is related to the emerging "broad part" of the pulse. These periods that we found in the EE are in one to one correspondence to the ones of the minA(t), Figure(4.6a). As happened for a narrow pulse, we found that the **EE oscillations amplitude decreases** after the formation of a horizon, and the **maxima monotonically increase** in this second stage. Notice that the approach

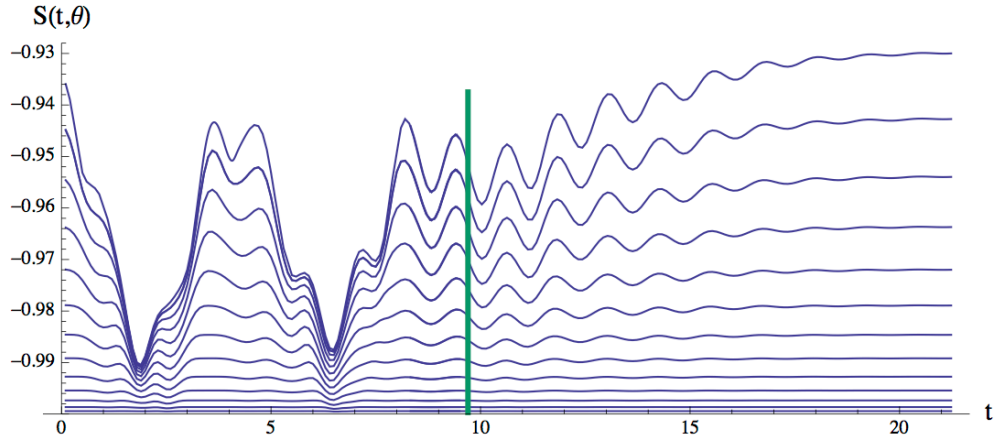

Figure 4.23: EE evolution to its equilibrium values for caps $\theta = .5, .., 1.5$ derived from an initial scalar profile 4.16 with $\sigma = 0.25$ and $M = 0.036$. The time at which $\min_x A(t, x) < 0.006$ has been signaled in green.

of this pulse to the formation of a black hole with all the mass is more efficient than in the narrow pulse of Figure(4.22). Namely, the intermediate broadness pulse needs less bounces with the boundary to form the final black hole.

Let us move now to the analysis of a **broad pulse** of $\sigma = 0.6$. Contrary to the previous case, this profile is radially delocalized along its complete evolution. In Figure(4.24) on the left, we show the mass density function for different times of the evolution. Notice that, as the total mass of this pulse is 40% of the threshold mass for large black holes, the subpulses this profile develops are very massive, and therefore they delay in climbing their gravitational potential. This favors the formation of a very broad peak that is what is observed in the first two snapshots of Figure(4.24) on the left. Arount $t \approx 7$ a damped oscillation is set (see the third snapshot in the previous figure) and at $t_h \approx 11$ a horizon is formed with almost all the mass available in the system.
The EE evolution is shown in Figure(4.24) on the right. As expected we found:

- Periods $\geq \pi/3$ because of the radially delocalized dynamics.
- Decreased on the amplitude oscillations when the damped quasi-stationary regime sets in.
- When the first horizon forms, the EE has almost reached is thermal value (because broad pulses collapse almost at once).
- EE maxima do not decrease along the evolution.

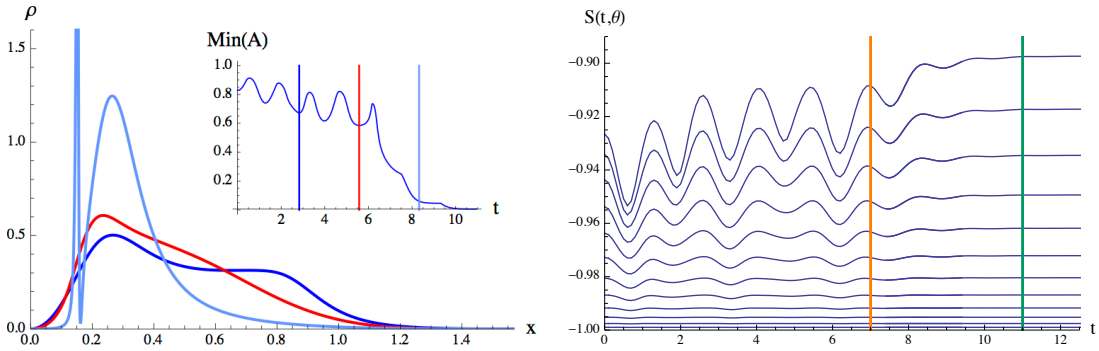

Figure 4.24: Initial profile 4.16 with $\sigma = 0.6$ and $M = 0.1538$. Left: three snapshots in the evolution of the scalar pulse. Right: EE for caps $\theta = .5, .., 1.5$. The time at which the quasi-stationary regime sets in has been signaled in orange and t_h in green.

Although it is difficult to give a QFT interpretation to all these items, we can give a qualitative interpretation to some of them.
First, let us comment about this $\pi/3$ periodicity. In previous sections, we proposed to relate the period of $\pi/3$ typical of broad pulses with the internal dynamics of the scalar profile in the gravitational side. From the QFT perspective, this hints towards having its root in the strong coupling dynamics of the out of equilibrium plasma.
Besides, when we were analyzing the EE evolution of narrow pulses, we argued that they described a stepwise relaxation process, triggered by the dephasing of a subsystem. However, what we see in broad pulses suggest a **thermalization process where all the system is involved**, and, therefore, this dephasing triggered by a subsystem is disfavored.

4.3.6 Behavior across critical points in AdS_4

We have seen in previous sections that the entanglement entropy is not totally correlated with the function MinA(t). However, we can try to push further this question and ask if the formation of a horizon leaves any imprint in the evolution of the EE. To this aim, we have computed the entanglement entropy along one of the critical points described in [24]. In this work, the relation between the radius of the horizon that first appears in the evolution and the amplitude ϵ (see expression (4.12)), which is obviously related to the mass $\mathcal{M}$, is explained for narrow pulses. They analyze how, when the pulse is very massive and, therefore, ϵ is big enough, the profile forms a horizon with radius x_h in its first fall towards the origin. As the mass is lowered, x_h becomes smaller and smaller until reaching a point where x_h vanishes for a critical amplitude ϵ_0. For amplitudes slightly below ϵ_0, the pulse comes back to the boundary, bounces there, and forms a horizon in its second fall from the boundary. If now we keep lowering the amplitude, we will find a new critical value ϵ_1 for which $x_h \to 0$. Namely, we know that, for narrow pulses, decreasing the mass of a pulse that collapses after n bounces, leads to a pulse that will collapse after $n+1$ bounces. Besides, we know that there are critical points in this process where an infinitesimal increased on the mass of the pulse will change the evolution: instead of another bounce we will have an infinitesimally small horizon which totally changes the causal structure of the gravity spacetime.

In Figure(4.25) we show some results that confirm what we observed in previous sections: the EE is not able to tell, in these cases, between the formation of an infinitesimally small horizon and a bounce at the origin. In this figure on the left we

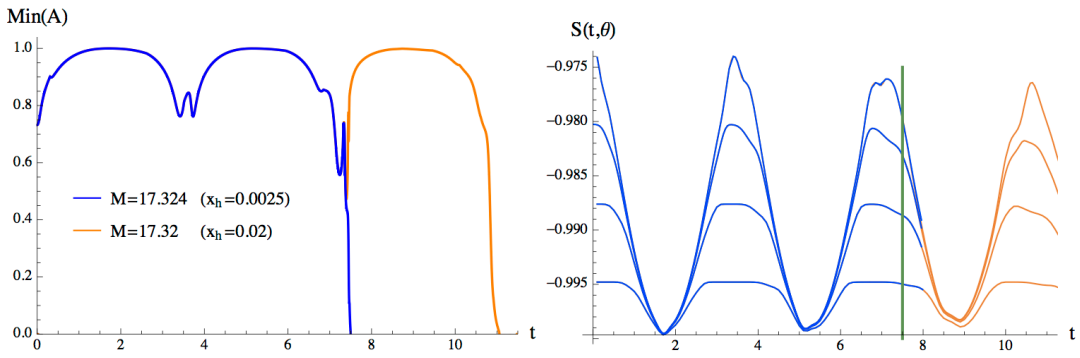

Figure 4.25: Two pulses with $\sigma = 0.1$ and masses slightly above (blue) and below (orange) critical collapse. Left: minimal radial value of $A(t, x)$. Right: EE evolution for caps with $\theta = 0.9, 1.2, 1.4, 1.56$. The green line marks horizon formation time for the above critical pulse.

have superimposed the evolution of the function MinA(t) for two narrow pulses of $\sigma = 0.1$ with masses of $M = 17.324$ and $M = 17.32$. Let us use the Table(4.1) to compare some features of these two pulses that lie so close to the corresponding critical point. If we look at this table, it is obvious that these pulses are very close

Mass	x_h	% x_{final}	Bounces
17.324	0.0025	4.4%	2
17.32	0.02	35%	3

Table 4.1: Comparison of the two pulses of Figure(4.25).

to the critical point that separates two bounces from three bounces before the first appearance of the horizon. To fully compare both evolutions, we had to push the two-bounces-simulation after the formation of a horizon at $t_h \approx 7.5$ (as can be seen in Figure(4.25)). Because this is a narrow pulse, pushing this simulation forward was numerically demanding, in fact we had to use a grid of 10^5 points to reach an acceptable precision. In the same figure on the right, we show the results of the EE for both simulations, both before t_h and shortly afterwards, even for spherical caps very close to the hemisphere. No difference between the EE evolutions was found. Namely, in this sense, the EE is not sensitive to the formation of a horizon.

Chapter 5

Holographic model for a quench in a gapped spacetime

The aim of this chapter is to holographically model a quench in a QFT living in $\mathbb{R}_{1,1}$ with a mass gap. To do so, we used the holographic model developed in [35, 36] where a hard wall was introduced to model the mass gap. This model leads easily to revivals, an important ingredient that we will use to compare with some specific QFT results. We studied the out of equilibrium dynamics of this holographic system by introducing new ingredients which allowed us to perform a new type of holographic quenches.

5.1 The hard wall model

The model we use in this chapter was described in [35, 36]. It is very similar to the bouncing geometries we already studied in AdS_3 but with two main novelties:

- To model an infinite $1+1$ theory in the QFT side, we followed the standard holographic dictionary, and we used an asymptotically AdS_3 spacetime with a Poincare slicing.
- To impose an infrared cutoff in the bulk geometry, namely a mass gap in the QFT side, we used a hard wall infinite in the x and t directions (see Eq(5.1)), where the spacetime ends.

As before, we coupled a massless scalar field to the metric and imposed translational invariance along the boundary spatial direction. We used the same parametrization of the previous chapter, but taking into account that, in this case, we were using the Poincare slicing and the holographic direction is no longer called x but z. The

boundary is located at $z = 0$ and the position of the infrared wall is denoted by $z = z_0$. With this conditions, the metric is explicitly written as:

$$ds^2 = \frac{1}{z^2}\left(-A(t,z)e^{-2\delta(t,z)}dt^2 + \frac{dz^2}{A(t,z)} + dx^2\right) \tag{5.1}$$

The equations of motion are:

$$\dot{\Phi} = \left(Ae^{-\delta}\Pi\right)' \quad , \qquad \dot{\Pi} = z\left(\frac{Ae^{-\delta}\Phi}{z}\right)' , \tag{5.2}$$

$$\delta' = \frac{z}{2}\left(\Phi^2 + \Pi^2\right) \quad , \quad A' = \frac{z}{2}A\left(\Phi^2 + \Pi^2\right) + \frac{2}{z}(A-1) \tag{5.3}$$

As before $\Phi = \phi'$ and $\Pi = A^{-1}e^{\delta}\dot{\phi}$. We also set the non-normalizable mode of the scalar field to zero so that there is no energy inflow from the AdS boundary. This is done by requiring the scalar field to vanish asymptotically. As a result, the total mass is conserved and is given by:

$$\mathcal{M} = z_0^{-2}(1 - A_0) + \frac{1}{2}\int_0^{z_0} y^{-1}(\Phi^2 + \Pi^2)A dy \tag{5.4}$$

A_0 is given by the value of the metric function $A(z,t)$ at the wall, which, in general, has to fulfill the momentum constraint:

$$\dot{A} = zA^2e^{-\delta}\Phi\Pi \tag{5.5}$$

In the setup we used, we assumed that the position of the wall is not varied along the evolution. Therefore, if $z_0 = cte$, then A_0 will be constant only if the scalar field satisfies Dirichlet or Neumann boundary condition at the wall[35, 36]. However, another possibility is to create a **time dependent profile for the scalar field at the wall** which allows A_0 to vary. In the following sections we will explore this possibility by choosing a particular time dependent profile for $\Pi(x,t)$ that we will denote by:

$$\Pi_0(t) = \Pi(t, z = z_0) \tag{5.6}$$

Notice that, although A_0 will no longer be constant along the evolution, due to the fulfillment of the momentum constraint the total mass will be conserved.

An important difference with previous models is precisely this freedom of varying A_0. If we recall the expression for the total mass $\mathcal{M}$, it is natural to separate it in two parts:

$$\mathcal{M}_0 = z_0^{-2}(1 - A_0) \quad ; \quad \mathcal{M}_\phi = \frac{1}{2}\int_0^{z_0} y^{-1}(\Phi^2 + \Pi^2)A dy \tag{5.7}$$

As $\mathcal{M}_0$ only involves parameters of the wall, it can be considered a property of it. In the following we will refer to it as mass of the wall. The $\mathcal{M}_\phi$ part can be thought as the contribution of the scalar profile to the mass[1].
A very interesting new phenomena associated to this model is precisely that, if we choose a time dependent profile $\Pi_0(t)$ for the scalar field at the wall, we find a **energy exchange between the wall and the scalar field**. The technical origin of this exchange is easy to find: the time variation of the profile at the wall $\Pi(t) = \Pi(t, z = z_0)$ causes A_0 to change in time and, therefore, $\mathcal{M}_0$ also varies. As the total mass is conserved, $\mathcal{M}_0$ and $\mathcal{M}_\phi$ must exchange energy during the evolution.

Let us now understand what is the geometrical meaning of $M_0 = z_0^{-2}(1 - A_0)$. We see in this expression that M_0 depends only on two parameters: the position of the wall z_0, and the value of $A(z, t)$ at the wall that we have called A_0. Typically, this model has been studied taking $A_0 = 1$, which is what is obtained in empty AdS. However, more generic situations are allowed, we can classify them, basically, in three different cases:

- $0 < M_0 z_0^2 < 1 \Rightarrow 0 < A_0 < 1$ this relates to black holes geometries whose horizon lies behind the wall.
- $M_0 z_0^2 < 0 \Rightarrow A_0 > 1$ this relates to naked singularities covered by the hard wall.
- $M_0 z_0^2 = 0 \Rightarrow A_0 = 1$ which is the specific case of having pure AdS with a hard wall.

Before going on with the analysis, let us show a **consistency check on the backgrounds with negative wall mass**. We basically checked that they do not induce superluminical propagation at the boundary in two ways. First, we evaluated the dispersion relation for several normal modes on static backgrounds with negative $\mathcal{M}$, and always found group velocities smaller than one. Besides, a related check we thought about, is that light rays leaving the AdS boundary, after reflection on the hard wall, return to this AdS boundary within the light-cone of the starting point. For static solutions with a vanishing scalar profile, the distance travelled by such light ray verifies

$$\tanh \frac{\sqrt{\mathcal{M}_0}\Delta t}{2} = \cosh \gamma \tanh \frac{\sqrt{\mathcal{M}_0}\Delta x}{2} \tag{5.8}$$

[1]In the previous chapter the total mass $\mathcal{M}$ was equal to $\mathcal{M}_\phi$.

where γ determine its incidence angle with the AdS boundary: $\frac{dz}{dx}|_{z=0} = \sinh\gamma$. Hence $\Delta t \geq \Delta x$. Relation (5.8) extends with the same conclusion to backgrounds with negative wall mass as far as $\sinh\gamma \geq \sqrt{|\mathcal{M}_0|}z_0$. Smaller incidence angles give rise to null geodesics that get repealed towards the AdS boundary without reaching the wall. Independently of γ they verify

$$\Delta t = \Delta x = \frac{\pi}{\sqrt{|\mathcal{M}_0|}} \tag{5.9}$$

They return to the boundary on the light cone of the starting point, respecting thus causality.

The equations of motion (5.3, 5.2) with Dirichlet boundary conditions at the wall admit **static solutions** with a non-trivial scalar profile [36]. The time independent Klein-Gordon equation simplifies to:

$$z^{-1}Ae^{-\delta}\Phi = \alpha \tag{5.10}$$

where α is an integration constant. As in the previous geometries we studied, in the hard wall model we have the gauge freedom of reparametrizations along the time coordinate. To make easier the holographic interpretation we chose t to be the proper time at the boundary. With this choice, the integration constant α can be understood as the expectation value of the field theory operator dual to the scalar field, $\alpha = 2\langle O\rangle$.

We have included Figure(5.1) on the left as an example of these kind of solutions. There, we show the set of static solutions without horizons and vanishing wall mass (other values of M_0 behave similarly). We can see that static solutions exist up to a threshold for ϕ_0, and that, for a given value of ϕ_0 there exists two branches of solutions:

- The brach with higher mass, which is linearly unstable.
- The branch with lower mass is stable and, remarkably, it includes regular solutions whose Schwarzschild radius is above the wall position.

To describe the radial energy distribution of the scalar configuration we used, as in previous geometries, the integrand:

$$\rho = \frac{1}{2z}\left(\Phi^2 + \Pi^2\right)A \tag{5.11}$$

In Figure(5.1) on the right we show this function for several values of ϕ_0 along the stable branch.

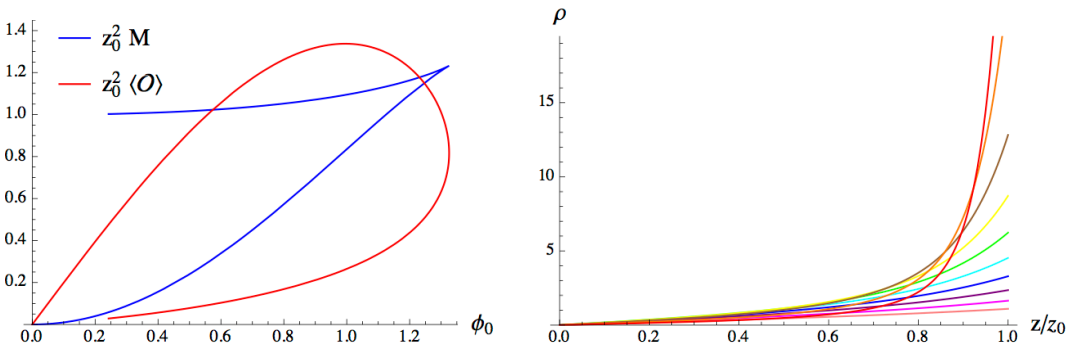

Figure 5.1: Left: Properties of static scalar configurations with vanishing wall mass and Dirichlet boundary conditions $\phi(z_0) = \phi_0$. Right: Radial energy profile of solutions along the stable branch for $\phi_0 = .5, .6, .., 1.3$ and the threshold value $\phi_0 = 1.32$ from bottom to top.

5.2 Infrared physics

It is interesting to analyze the infrared physics of the static solutions that were introduced in the previous section. To this aim, we worked with two quantities:

- The **correlation length**, that we define using the holographic entanglement entropy as the size of the interval for which the EE reaches its maximum.
- The **mass gap**, that we define as the lowest frequency of the normal modes spectrum over a static solution without horizon. This is because we know, from the holographic dictionary, that the spectrum of normal modes relates to the non-analyticities in the two point function of the dual field theory operator. Hence, it is reasonable to use the lowest normal frequency as a definition of the mass gap.

5.2.1 Computation of the Holographic Entanglement Entropy

From previous sections, we know that the entanglement entropy of an interval in the QFT side, is computed holographically by the length of the extremal curve which is homologous to the interval [74], and which anchors at the AdS boundary on the interval endpoints [37, 51, 41].

However, the hard wall model presents some peculiarities that forced us to slightly reformulate these conditions. In Figure(5.2) on the right we can see how, when we are dealing with a sufficient large interval, the corresponding geodesic unavoidable

intersects the infrared wall. Once we realize that geodesics can end in the infrared wall, it is easy to see that we have actually two possible configurations of geodesics (see Figure(5.2)), the connected or the disconnected one. Following the standard

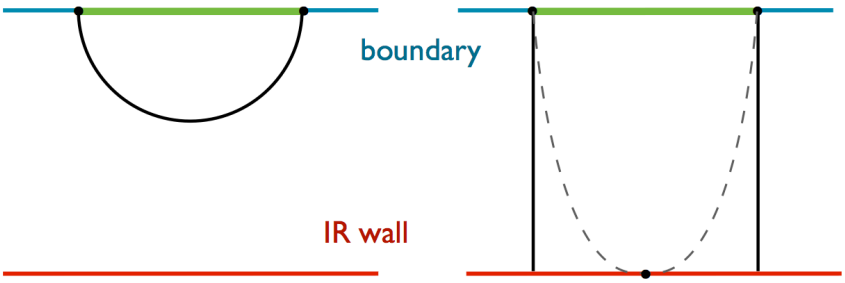

Figure 5.2: Connected (a) and disconnected (b) geodesic configurations anchoring at the endpoints of a boundary interval.

recipe, we have to choose the one with minimal length[2]. However, at this point a natural question arises: if we follow the homology condition, we are forced to consider, in the length of the disconnected geodesic configuration, the contribution of the infrared wall interval which would connect both geodesics. If we include it, we would have an extensive behavior of the entanglement entropy which is typical of a thermal state or a highly excited state which violates the area law. However, this possibility is not consistent with the fact that, in such field theory states, the eigenfrequencies of the laplacian in the dual geometries should have an imaginary part which would reflect the finite lifetime of excitations (this is what actually happens in the black hole backgrounds, which are dual to thermal equilibrium states). In the hard wall model setup, the frequencies of the harmonic modes with Dirichlet or Neumann boundary conditions are purely real. Therefore, the EE cannot be an extensive quantity and, as a result, the length of the interval in the infrared wall cannot be included.
But, if we do not include the interval in the infrared wall joining the disconnected geodesics, we cannot fulfill the standard recipe for the computation of the holographic entanglement entropy. We would be violating the homology condition. That is why, in this setup, we need to slightly reformulate the homology condition: *besides geodesics which satisfy the homology constraint, we also allow geodesics which, together with their associated AdS boundary interval, are homologous to an interval at the wall.* In a more formal and mathematical way, we now ask to the disconnected geodesics not to

[2]Actually, we have to choose the extremal one, and if we have several options, we have to choose the one with minimal length.

be homologous to the interval at the AdS boundary, but to be homologous to its associated interval in the relative homology defined with respect to the infrared boundary.

Notice that, with this slightly modified recipe for the HEE computation, the EE of an interval is equivalent to that of its complementary also in the geometries with $M_0 z_0^2 < 1$. This suggests that all these geometries describe pure states [60, 61].

5.2.2 Example of a correlation length computation

Let us show in a particular example how the EE holographically saturates and the correlation length is computed. We consider the simple case in the hard wall model of static solutions with vanishing scalar profile.
First, we need to compute the length of the extremal connected geodesic which anchors at the endpoints of an interval of size l. If we consider a wall mass M_0 such that the corresponding black hole with that mass would lie behind the wall position, the geodesics that we need to compute, as far as they do not reach the wall, are the same that we would need to compute in the black hole background. Therefore, the length is given by:

$$L_1 = 2\log\left(2\sinh\sqrt{M_0}l/2\right) - 2\log\sqrt{M_0}\epsilon \tag{5.12}$$

where we have regularized the divergence by cutting the bulk at a UV scale $z = \epsilon$.
To know if this is the configuration of minimal length we have to compare it with the the disconnected configuration. As was commented before, this configurations is given by the geodesics that start on the interval endpoints and extends radially to the wall. Its length is given by:

$$L_2 = 2\log\left(2z_0/\epsilon\right) - 2\log\left(1+\sqrt{1-M_0 z_0^2}\right) \tag{5.13}$$

Notice that, as expected, this quantity does not depend on l, the size of the interval. For small intervals, L_1 will be smaller and the connected option will be preferred. As l grows, we will reach an interval l^* where $L_1 = L_2$. For larger intervals $l > l^*$, the EE will be given by the length of the disconnected choice L_2 (this behavior was sketched in [36]). As this quantity does not depends on l, the EE saturates to a constant value that we have called the correlation length ξ. In this example it is given by:

$$\xi = \frac{2}{\sqrt{M_0}}\,\mathrm{arcsinh}\left(\frac{\sqrt{M_0}z_0}{1+\sqrt{1-M_0 z_0^2}}\right) \tag{5.14}$$

Let us analyze this expression as a function of M_0. First, it is easy to see that, if $M_0 = 0$, then $\xi = z_0$. If we now increase M_0, the correlation length ξ grows up to a finite value attained at the horizon threshold $M_0 z_0^2 = 1$. It is important to comment that this expression can be smoothly continued to negative values of M_0, this causes a monotonic decrease of the correlation length ξ. In fact, taking the limit of a very large negative wall mass, makes ξ goes to zero as:

$$\xi = \frac{\pi}{\sqrt{|M_0|}} \tag{5.15}$$

5.2.3 Correlation length vs. mass gap

We have commented in previous sections how, although we have used different definitions of the correlation length ξ and the mass gap, both of them should describe, in an equivalent way, the infrared physics of the system. In this subsection we analyze how and when this happens. To this aim, we include Figure(5.3), where we can compare both quantities and analyze if, as expected, they are of the same order[3].

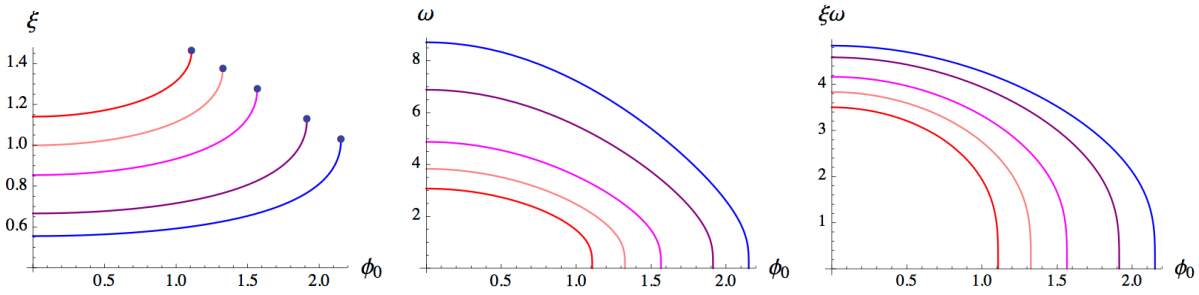

Figure 5.3: Correlation length (a), mass gap (b) and their product (c) as a function of ϕ_0 for $M_0 = 1/2, 0, -1, -4, -8$ from red to blue.

In the same figure on the left, we see how ξ and ω are of the same order for almost all values of ϕ_0. However, we find a mismatch close to the stability threshold, where ω vanishes and ξ remains finite. We can explain this by noticing that the computation of ξ has been done using the HEE on a classical geometry, which only takes into account the leading N contribution. However, the mode becoming unstable close to the threshold for horizon formation, reflects an order one effect which cannot be seen by the HEE. That is why, in this limit, ξ and ω are so different.

[3]In an interacting field theory we do not expect both quantities to coincide, but they should be of the same order.

5.3 QFT quench: boundary conditions at the wall

Now that we have explained the hard wall geometry, the possibility of having static solutions, and the two parameter we are going to use to measure the infrared dynamics (namely the mass gap and the correlation length), we can explain how we are going to perform the time evolution in the system. This is a main difference with the previous geometries we have studied in this thesis. In this case, we actually perform a quench by changing the couplings of the QFT and, then, we follow the whole time evolution.

Let us explain how we are going to perform the **modification of the QFT couplings** from the gravity side. M_0 and ϕ_0 are boundary values that cannot be changed by bulk dynamics. Therefore, using the standard holographic dictionary, we propose to understand them as couplings in the QFT.

Now that we understand M_0 and ϕ_0 as couplings in the dual field theory, we propose that the static configurations, when they exist with these boundary values, see Figure(5.4), are dual to the **ground state** for the corresponding couplings in the QFT. This identification is reasonable because the static solutions are the configurations with less energy. In Figure(5.4), the yellow area shows combinations of (ϕ, M_0) for which there are static solutions. Notice that, pure AdS with a cutoff, corresponding to $M_0 = \phi_0 = 0$, respects Lorentz invariance while non-zero values of M_0 and ϕ_0 in general break it. These backgrounds represent pure states with order N^2 expectation values of the stress tensor and the operator O, dual to the scalar field. These features are typical of **condensates**, which are the states in the QFT side we propose as duals to the static solutions.

At this point, we can describe **the quench we performed** on the system. We chose a time dependent boundary condition for ϕ_0 of the form:

$$\Pi_0(t) = \frac{\epsilon}{\alpha} \frac{1}{\cosh^2 \frac{t}{\alpha}} \tag{5.16}$$

As initial state we used the corresponding static background. Notice that, in the QFT side, what we are doing is:

1. We start in the ground state of a system with a coupling g_0 (a condensate if we are not in pureAdS with a cutoff) corresponding to ϕ_0.

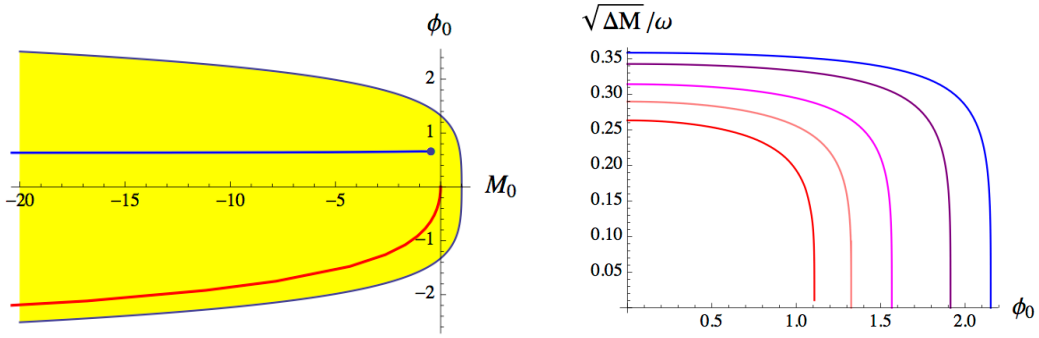

Figure 5.4: Left: In yellow, couplings which admit stable solitonic solutions. Final couplings after an action (5.16) which starts at $M_0 = \phi_0 = 0$: as a function of α for $\epsilon = 0.3$ (blue), and as a function of negative ϵ for $\alpha = .8$ (red). Right: Relation (5.19) as a function of ϕ_0 for fixed M_0, with the same color code as in Fig.5.3.

2. We change the coupling g_0 to g_1 in a more or less smooth way depending on α.

3. We let the system evolve.

In the gravity side the change of couplings (driven by $\Pi_0(t)$), generates a scalar pulse which enters from the wall into the bulk. The energy of this scalar pulse is taken from the wall (as the total mass is conserved), so that the value of $\mathcal{M}_0$ changes during the process. In fact, its final value can be even negative.[4] We have also checked that, if the starting point is a geometry with any $\mathcal{M}_0$, including $\mathcal{M}_0 < 0$, no irregularities are found in the evolution.

Once we know the kind of perturbation we are producing in the system, let us analyze its behavior with the parameters α and ϵ (Eq(5.16)). In Figure(5.4) we have included two lines (red and blue) to illustrate this dependence. Both lines show us the final couplings (M_0, ϕ_0) after a perturbation from pureAdS with a cutoff. The blue one keeps $\epsilon = 0.3$ fixed and varies α (the dot indicates the limit $\alpha \to \infty$). What we observe in the evolution as α is decreased can be summarized in four items:

- Pulses became more and more localized on the radial direction.
- The part of the mass that we associate to the scalar field, namely $\mathcal{M}_\phi$, increases and, as the total mass is conserved, the final value of $\mathcal{M}_0$ decreases.
- The value of ϕ_0 keeps practically constant showing that it is mainly determined by ϵ.

[4]This certainly happens if the starting point is pure AdS with a cutoff.

The red line in Figure(5.4) shows the same setup but now keeping constant $\alpha = 0.8$ and varying ϵ.

In the geometries we studied before the hard wall, we were drawing our attention to the bounces of the scalar profile, and to how these bounces where related to the existence of **revivals**. A natural question would be: Have we seen something similar in the hard wall setup? The answer is yes, and is basically due to the infrared boundary we have introduced[5]. If the starting point of our evolution has a total mass whose Schwarzschild radius is below the wall position, it will never be possible to form a black hole (as the spacetime ends in the infrared boundary) and the scalar pulse will bounce forever back and forth (it can also form a standing wave) between the AdS boundary and the infrared one [35]. In the dual QFT we will never reach a thermal state. We will see an explicit example of this behavior in the following lines. It is important to mention that, although this reasoning is very intuitive and roughly speaking correct, it has some subtleties related to the fact that we can actually have static solutions with a total mass whose Schwarzschild radius lies above the position of the hard wall. We will take this into account in the forthcoming explanations.

Another question that we can ask is: Are these bounces (or oscillations of a standing wave) that we find in the gravity part and we interpret as revivals in the QFT side, actually, **compatible with what we would expect in an strongly interacting QFT?** We can partially answer this question by analyzing the regime of energies where we expect to have revivals in a QFT.
Notice that, in this case, the AdS/CFT correspondence tell us that we are dealing with a strongly interacting quantum fiel theory (because its dual theory, the gravity theory, is classical). However, strongly interacting field theories usually exhibit a fast approach to a thermal state, which prevents revivals. It seems that we should not find any reconstruction of a state but just a fast approach to a thermal state. An exception to this can be found in out of equilibrium states where the scale set by the energy density is smaller than the infrared gap. Namely, revivals in d-dimensional field theory might happen only when:

$$(E/n)^{1/d} < m_{gap} \tag{5.17}$$

[5]Notice that in this setup we are dealing with a noncompact AdS3 spacetime (we are in the Poincare patch).

where E is the energy density, n the number of elementary fields, m_{gap} a measure of the gap and d the dimension of the QFT.

We found that the bounces/oscillations of the scalar profile, partial revivals in the dual field theory, are compatible with this expression (we will show it in the forthcoming lines). In the holographic setup the central charge plays the role of n, and the mass gap is set by the inverse of the boundary sphere radius. As $n \sim 1/G$, and taking into account how we have defined the total mass $\mathcal{M}$, we know that the energy density per species E/n, is given by $\mathcal{M}$ in the gravity setup.
Now, let us see how to translate the condition of Eq(5.17) to the hard wall model and how it is fulfilled. First, we have to set $(\mathcal{M}_0, \phi_0)$ in order to set the couplings of the QFT we are dealing with. The next step is to know in which regime of energies we expect to find revivals. In order to do this we define the magnitude $\mathcal{M}^{th}$ by the condition that any configuration with $\mathcal{M} > \mathcal{M}^{th}$ leads to horizon formation by direct collapse. An estimate for this magnitude consists in requiring the associated Schwarzschild radius to lie at the wall, $\mathcal{M}^{th} = z_0^{-2}$. We have seen however that there are stable solitonic solutions whose Schwarzschild radius lies above the wall. Thus a better estimate is provided by:

$$\mathcal{M}^{th} \lesssim \overline{\mathcal{M}} \tag{5.18}$$

where $\overline{\mathcal{M}}$ is the mass of the static solution with a Schwarzschild radius bigger than the position of the hard wall (actually we choose the one with biggest mass for a given $\mathcal{M}_0$, it would correspond to the border of the yellow area in Figure(5.4)). At this point, we know that the energy density that we need to have revivals in this model must be[6] $\mathcal{M} < \mathcal{M}^{th} \lesssim \overline{\mathcal{M}}$. If we choose that the zero energy level is the ground state, then the condition (5.17) is translated to:

$$\sqrt{\overline{\mathcal{M}} - \mathcal{M}_{gs}} \lesssim m_{gap} \tag{5.19}$$

Where we have taken $d = 2$ (the dual QFT lives in two dimensions). The quantity inside the square root is the minimal energy density per species over the ground state which will always lead to fast thermalization. Energies below this quantity lead to bounces/oscillations that are understood as revivals in the QFT side.

At the beginning of this chapter, we defined the mass gap as the lowest frequency of the normal modes spectrum over a static solution without horizon. Following

[6]This is just a necessary condition.

this definition, we have checked that, fixing $\mathcal{M}_0$ to different values and varying ϕ_0, expression(5.19) is fulfilled. This is clearly seen in Figure(5.4) right. Notice that, to make this plot, we have not performed any quench.
We complement the previous test by analyzing (5.19) for asymptotical large negative M_0 and vanishing scalar profile. If we identify $m_{gap} = 1/\xi$, we use expression (5.15), and we realize that $\overline{\mathcal{M}}\ /|\mathcal{M}_0| \to 0$, we have:

$$\sqrt{\overline{\mathcal{M}} - \mathcal{M}_{gs}} = \sqrt{\overline{\mathcal{M}} + |\mathcal{M}_0|} \lesssim m_{gap} \Rightarrow \xi\sqrt{\overline{\mathcal{M}} + |\mathcal{M}_0|} \to \pi \tag{5.20}$$

which agrees with the expected result.

5.4 The holographic dual of a quench?

We have just seen that the oscillating geometries of the hard wall model satisfy the basic requirement to be interpreted in terms of quantum revivals. In the following we want to explore what is the field theory state associated with an oscillating geometry and the physical mechanism for the revivals it represents.

The time parameter α has a major influence on the properties of the scalar pulse resulting from (5.16). We have chosen t to be the proper time at the boundary. Hence α should be corrected by a redshift factor:

$$\overline{\alpha} = \frac{\alpha}{z_0}\sqrt{A_0}e^{-\delta_0} \tag{5.21}$$

As before, A_0 and δ_0 are the metric functions evaluated at the wall on the solitonic configuration chosen as initial state. Although in previous sections we have already commented the effect of varying α on the quench, we are now going to analyze $\overline{\alpha}$ by giving more results and showing explicitly the profile of the pulse resulting from this quench.
What we observed can be summarized as:

- $\overline{\alpha} < 1$ generates radially localized pulses.
- $\overline{\alpha}$ very large generates adiabatic evolutions where the system moves along the space of solitonic solutions without generating a dynamical profile.
- $\overline{\alpha} \sim 1$ mostly excites the lowest normal mode over the soliton determined by the final boundary conditions at the wall (the oscillating component is a standing wave).

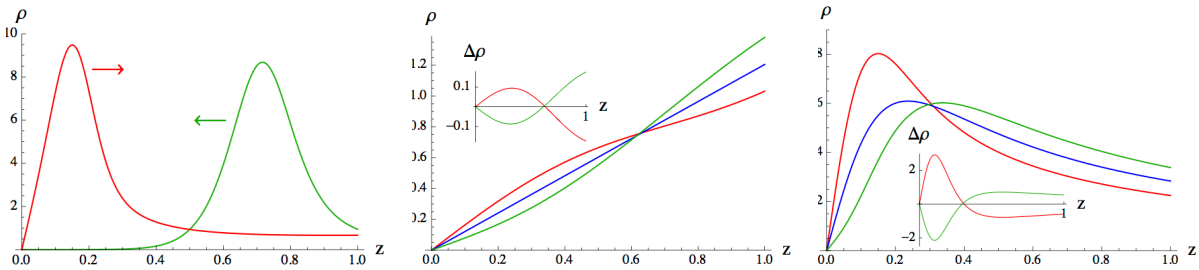

Figure 5.5: Scalar pulses resulting from (5.16) with initial state $\{M_0, \phi_0 = 0\}$: a) $\alpha = .2,\ M_0 = 0$; b) $\alpha = .8,\ M_0 = 0$; c) $\alpha = .2,\ M_0 = -18$. The final values of the couplings are: a) $M_0 = -1.15,\ \phi_0 = 0.66$, b) $M_0 = -0.3,\ \phi_0 = 0.52$, c) $M_0 = -20.17,\ \phi_0 = 0.58$. Inset: scalar pulse after subtracting the soliton profile associated to the final couplings.

This summary is illustrated with what we see in Figure(5.5). Let us comment a little bit these results so that we can also understand the importance of working with $\overline{\alpha}$ instead of α. All this figures have $z_0 = 1$. The first two have an initial state which is pure AdS with a cutoff, for which $\overline{\alpha} = \alpha$. The one in the left has $\overline{\alpha} = 0.2$ and, as expected, generates a localized profile that bounces back and forth between the hard wall and the boundary. The one in the center has a bigger $\overline{\alpha}$ which is of order one ($\overline{\alpha} = 0.8$), we can see how it induces a standing wave over the corresponding solitonic state, plotted in blue. The figure on the right has a different initial state, it starts from $M_0 = -18$ with vanishing scalar profile. Notice that while its $\alpha = 0.2$, its $\overline{\alpha} = 0.87$. Consistently, its profile is not a traveling narrow pulse but a standing wave over the corresponding solitonic state.

Now that we have classified the types of profile we get as a function of $\overline{\alpha}$, let us do the same but using the energy. Following the analysis in the previous section, a natural option is to take the **energy density per species over the ground state, but normalized with respect to the infrared gap**. Namely:

$$e = \frac{M - M_{gs}}{\overline{M} - M_{gs}} \tag{5.22}$$

Where, as before, M is the total mass, M_{gs} is the mass of the static soliton associated to the final value of the couplings, and $\overline{M}$ was defined in (5.18).
In our simulations, we have seen that quenches with $\overline{\alpha}$ of order one, corresponds to the limit of small energy density (small e). This is consistent with the results in Figure(5.5), from left to right they have been generated with $\overline{\alpha} = 0.2, 0.8, 0.87$, the

corresponding energy density quotient is $e = 0.28, 0.001, 0.002$. Notice that while the two last pulses have $\overline{\alpha} \sim 1$ and $e \ll 1$, the first one reaches much bigger e with a quite smaller $\overline{\alpha}$. We have found this to be a general behavior, namely, actions with $\overline{\alpha}$ small lead in general to higher excited states.

Besides $\overline{\alpha}$ and e, we can also analyze the **periodicities** of the pulses we generate with this kind of quenches. For standing configurations, as the ones in the center and the left of Figure(5.5), the period is given by the frequency of the lowest normal mode.

$$\tau_{st} \approx \frac{2\pi}{\omega} \tag{5.23}$$

This is an expected result, because these standing configurations project, mostly, on the lowest mode.

For narrow pulses the period τ_{tr} is of the same order, but the numerical values do not coincide. We can see a comparison between both cases in Figure(5.6), where we have plotted the period of the lowest normal mode τ_{st}, and the one of thin traveling pulses of low mass, everything for $M_0 = 0$. Notice that for ϕ_0 small, the standing

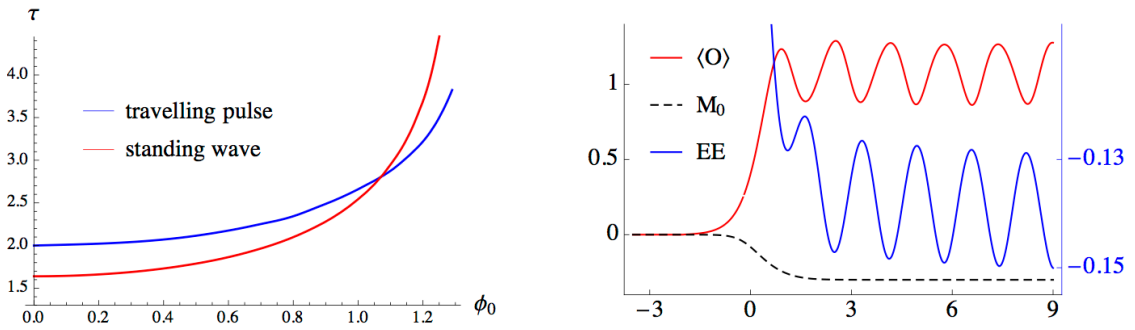

Figure 5.6: Left: Periodicity of oscillating geometries as a function of ϕ_0 for $M_0 = 0$. Right: Evolution of $\langle \mathcal{O} \rangle$, M_0 and the entanglement entropy of large intervals for the example in Fig.5.5b.

pulses have a smaller period than the travelling ones. However, when ϕ_0 approaches the instability threshold, $\omega \to 0$ and τ_{st} diverges while τ_{tr} stays finite. This is because localized pulses have almost no overlap with the lowest harmonic.

Until now, we have described the different post-quench profiles as a function of three parameters: $\overline{\alpha}, \tau, e$. With this information, let us try to connect with the out of equilibrium dynamics of known QFTs. In particular, we qualitatively compare to

the analysis done in [2], where the **quench dynamics of the massive Schwinger model, triggered by turning on abruptly an uniform background electric field** was explored. Notice that, in that analysis, the theory after the quench remained gapped.[7]

First, let us comment that in this massive Schwinger model, revivals occur for **small energies** as expected from the previous analysis. This is because, although switching on an electric field generically induces pair production of fermions, if the fermions are massive this requires an energy density of the order of the infrared gap. Below it, namely for small energies, there are revivals [2]. Notice that these revivals cause the periodic oscillation of the electric field itself and the particle number.

Let us now move to the periodicities of these revivals. In the limit of small quenches, revivals are almost perfect with **periodicity**:

$$\tau_{QFT} = \frac{2\pi}{m} \tag{5.24}$$

Where m is the mass of the lowest stable excitation of the final hamiltonian. This periodicity strongly recalls the one of standing pulses $\tau_{st} = 2\pi/\omega$. In fact, we propose that the dual of these kind of revivals in the massive Schwinger model, are the revivals we observe in the **standing pulses** of the hard wall model. To connect τ_{st} and τ_{QFT} we just have to remember that holography relates the frequencies of the normal modes with non-analyticities in the correlation functions. Therefore, it is natural to relate the frequency of the lowest harmonic in the hard wall model with the mass of the lowest stable excitation in the Schwinger model. Besides, in [2, 78] it is shown that Schwinger revivals with frequency τ_{QFT}, are coherent states of modes of the lowest excitation. This allowed us to go a step further, and relate standing configurations with this kind of coherent states.

The requirements for a QFT to have a classical gravity dual are strong coupling and large N. The first requirement is fulfilled by comparing our holographic results to the analysis done in [2], which uses tensor network techniques that are not limited by the strength of the interactions. However, the large N problem still remains. The Schwinger model does not have a **large number of elementary fields**. Nevertheless, notice that in the hard wall model revivals mostly depend on the ratio of energy

[7]The Schwinger model has been studied with these tensor network techniques in other works [75, 76, 77].

density per species, and N factors out in this quotient. Therefore, we believe that a qualitative comparison between both models can be sensible.

Let us complete the analysis of standing pulses by showing some results. In Figure(5.6) we show the time evolution of the expectation value of the operator dual to the scalar bulk field (red) and the entanglement entropy (blue). The quench that was performed in this example is the one shown in the center of Figure(5.5) (a standing pulse with $e = 0.001$). Notice that the oscillations of $\langle O \rangle$ are in opposite phase to those of the entanglement entropy. This is what also happens in the massive Schwinger model **if we put in correspondence the oscillations of $\langle O \rangle$ with the ones of the electric field**.

At this point, let us analyze what happens when we increase the energy e of these standing pulses. Generically, we start to see how structures with some **radial localization**, which are still compatible with revivals, emerge.
Following the previous reasoning, we propose that these more localized configurations holographically correspond to out of equilibrium states which include, besides momentum zero modes, an appreciable percentage of **finite momentum modes**. Therefore, with modes of finite momentum, it makes sense that propagation effects become relevant in the evolution of its entanglement pattern.

Let us now analyze in detail how these more localized configurations are generated. We have already mentioned that standing waves are produced after quenches with $\overline{\alpha} \approx 1$ and very small energy density. To generate narrow profiles we need to increase the value of e, which can only be done by lowering $\overline{\alpha}$ (see Figure(5.5a)). We have included Figure(5.7), where we have performed quenches from the pure AdS with a cutoff, to show the actual **relation between α and e**. To this aim we fixed three different values of α and plotted $\log e$ as a function of the final values of M_0. What we see at a first sight is that e does not vary much along a wide range of final negative wall masses, but strongly depends on α. An energy e smaller than 0.01 (and therefore a standing wave) is always obtained for $\alpha = 0.8$. Bigger e (of the order of 0.8) are obtained for $\alpha = 0.2$ and large negative M_0, very close to the threshold for gravitational collapse or, in the dual field theory, very close to fast thermalization.
Besides, we have noticed that the radial localization of the scalar profile grows with e even at fixed α. We can see this by comparing the $\alpha = 0.2$ examples in Figure(5.5a), with $e = 0.28$, and Figure(5.7) on the left, with $e = 0.7$.

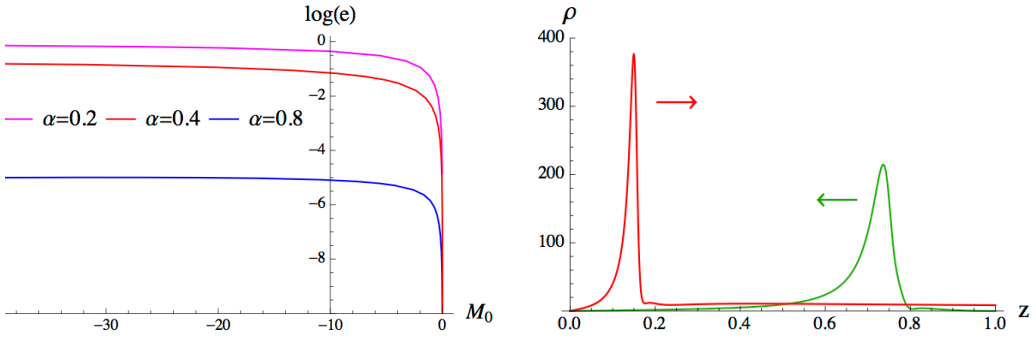

Figure 5.7: Left: Value of the quotient (5.22) for wall actions with initial state $\{M_0 = 0, \phi_0 = 0\}$ and fixed α, as a function of the final wall mass. Right: As in Fig.5.5a, with final couplings $M_0 = -10.09$, $\phi_0 = 1.27$

Let us perform an **additional check**. Following the reasoning we have done until now, if we put a high energy e on the lowest normal mode, we would expect to see, during the evolution, the emergence or more localized structures. This is what we actually observed in this additional test which is now explained in detail.
The initial profile we evolved is given by:

$$\Phi(z, t = 0) = \Phi_S(z) + \epsilon \frac{d\chi}{dz}(z), \qquad \Pi(z, t = 0) = 0 \tag{5.25}$$

where we kept the wall couplings fixed, Φ_S is the soliton solution associated to them, and χ is the radial profile of its lowest normal mode:

$$\Delta\phi(z, t) = \chi(z) \cos(\omega t) \tag{5.26}$$

Using what we have argued before, these initial data represent a field theory coherent state of zero modes of the lowest excitation with an average occupation number controlled by ϵ. We have shown in Figure(5.8) the radial profile minus its static component (as in the inset of Figure(5.5)) for a profile with $M_0 = -1, \phi_0 = 0.5$ and ϵ tunned to obtain $e = 0.5$. In this figure, it is easy to see the emergence of localized structures, as expected with a high e. Besides, we checked that radial localization and displacement is more pronounced the bigger the value of e, supporting the field theory interpretation we have given in this section.

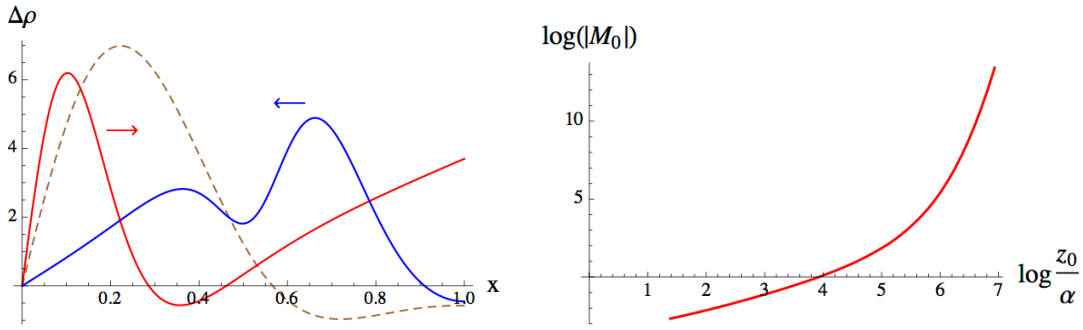

Figure 5.8: Left: Scalar profile minus its static component for the initial data (5.25) with $M_0 = -1$, $\phi_0 = 0.5$ and $e = 0.5$. We show two snapshots of the evolution and, with a dashed line, the initial profile. Right: Final value of the wall mass for increasingly abrupt wall profiles of fixed amplitude, starting at $\{M_0 = 0, \phi_0 = 0\}$.

5.5 Discussion

In this section we want to address at a more general level how to holographically model a quench protocol. The holographic dictionary maps the boundary value of bulk fields to field theory couplings. We have shown that this applies at the infrared wall as well as at AdS boundary. Time dependent boundary values provide therefore the natural playground to represent quantum quenches.

A quench is understood as a change of couplings faster than any response time proper of the system. For this reason a quench is usually described as an instantaneous action. A first guess is **identifying the time span for the variation of the boundary conditions with the time span of the quench**. This is however problematic [79, 80, 81, 82]. By dimensional arguments, varying the boundary value of a massless scalar field at the AdS_3 boundary generates a pulse with mass and width

$$M \propto \frac{\epsilon^2}{\delta t^2}, \qquad \Delta \propto \delta t, \tag{5.27}$$

where δt is the time span of the change and ϵ its amplitude. We wish to take the limit $\delta t \to 0$ keeping ϵ non vanishing, since otherwise no change of couplings is generated. A singular shell is then obtained carrying infinite energy and zero width. A related situations is obtained for the wall actions (5.16). Decreasing α leads to ever more negative wall masses. In Figure(5.8) we plot the final value of $|M_0|$ when the wall action starts in pure AdS with a cutoff. Its growth with $1/\alpha$ is much faster than a power law. Notice that is possible because two dimensionfull quantities are now involved, α and z_0. Relating the time span of a quench with α would lead again to a singular configuration.

We are interested in holographically simulating global quenches which induce a finite energy density. In order to achieve this in the context of gravity plus a massless scalar, we are forced to consider changes of boundary conditions with a finite time span. By comparing with the massive Schwinger model [2], we have seen that this crude modeling leads to reasonable results. A crucial condition was linking the radial thickness of the resulting scalar configuration, with the energy density of the quench state we want to describe. We expect this condition to be an important entry in the dictionary for holographic quenches. It is supported by two facts that go beyond the particular model considered in this paper. Namely, the different radial dynamics of broad and thin profiles, and the fact that increasing the mass of a broad profile leads to the appearance of localized structures as it evolves.

A closely related question is **what type of bulk configurations cannot be expected to represent typical out of equilibrium field theory states**. By typical we mean that no fine tuning was necessary to generate them. This is specially relevant in an initial data setup for the gravitational evolution as the one we studied in Chapter 4. We argue now that thin pulses of small e, which are the ones more studied in Chapter 4, are not typical in the above sense.
In the context of the hard wall model, let us consider a thin pulse whose mass is small enough for the associated Schwarzschild radius to be well below z_0. Following previous arguments, a thin pulse must correspond to a dual field theory state able to resolve scales much shorter than the correlation length. On the other hand, the assumed mass implies that there is not enough energy density to distribute it democratically between the N^2 field theory degrees of freedom and overcome, or even come close to the gap. In the language of the Schwinger model, this suggests the production of virtual pairs which do not produce an irreversible decay of the electric field. Virtual pairs cannot propagate further than the correlation length before recombining, what is consistent with the picture of a thin pulse traveling back and forth between wall and AdS boundary. It is unlikely that such a field theory state, which combines characteristics proper of high and low energies, can be produced without fine tuning.

Chapter 6

Conclusions / Conclusiones

Conclusions

In this thesis we have holographically studied the out of equilibrium dynamics in three different strongly coupled QFT scenarios: a compact spacetime in 1+1 and 2+1 dimensions, and an infinite spacetime in 1+1 dimensions with a mass gap. In order to model these dynamics, we used the AdS/CFT correspondence where, in the classical gravity side, we studied the dynamical formation of a black hole in asymptotically AdS spacetimes with a massless scalar field. As a black hole in the gravity side models a thermal state in the QFT dual system, the formation of a black hole models the dynamics towards equilibration. Interestingly, we also analyzed how to interpret, from the QFT side, the non formation of a black hole in these holographic models. One of the main results of this thesis is to have found, holographically, revivals in the strongly coupled QFT of the three models we analyzed.

In **Chapter 4**, we focused on the analysis and interpretation of the two first holographic cases we just mentioned. Namely, in the gravity side we analyzed an asymptotically AdS spacetime coupled to a massless scalar field in 2+1 and 3+1 dimensions in global coordinates. In the QFT side, this corresponds to a strongly coupled theory which lives in a compact spacetime $S^1 \times R$ and $S^2 \times R$, correspondingly.
In the gravitational analysis of AdS_4 and AdS_3, we found quite different behaviors between **broad and narrow pulses**. While the evolution of narrow pulses was mostly driven by weak turbulence, in the case of broad pulses, it was found that this effect was not as important as the scattering among subpulses, which is the one that finally dominated the evolution. Besides, a very important result of this thesis, was the achievement of simulating the evolution of these metrics in AdS_4 **after the first**

appearance of an apparent horizon. This result allowed us to observe different patterns of equilibration. Narrow pulses suffered a **stepwise relaxation** process triggered by the dephasing of a subset of the degrees of freedom. However, in the case of broad profiles, this mechanism seemed to be disfavored and a relaxation involving the whole system was observed.

In the **QFT interpretation** of these results, we related the partial reconstructions of the metric, called bounces in the text, to the existence of **revivals** in the dual field theory. Surprisingly, with narrow profiles, at very low energy densities and for some parts of the evolution, although the dual QFT was strongly coupled, we could relate the pattern of revivals to the propagation model of entanglement Cardy and Calabrese proposed in [1]. The main result which allowed us to make this link, was the matching of the **periodicities** we found.

The observable we computed was the **holographic entanglement entropy** which we analyzed during the whole time evolution of the metric. To this aim, we used the holographic prescription for the calculation of the EE in time dependent backgrounds given in [41]. Both in AdS_3 and AdS_4, we found that, for narrow pulses, no matter the mass, the EE showed a **universal behavior** when the pulse was in its first fall from the boundary towards the origin. Besides, we defined two quantities that allowed us to describe some new features in the evolution. First, the dephasing time t_{deph}, which was the time at which the system dephased, and, then, the revival time t_{rev}, that was the time at which the initial state was partially recovered. We always found, both in AdS_3 and AdS_4, that $t_{deph} \approx \pi/2$. However, for t_{rev} the result was quite different: while in AdS_4 $t_{rev} \approx 2t_{deph}$, in AdS_3 these two quantities were, in some cases so different, that previous to the reconstruction of the state we saw the emergence of a **plateau** where the EE remained constant. This plateau could delay t_{rev} so much that $t_{rev} \gg t_{deph}$, causing the emergence of two different time scales. We related this phenomena to the different group of symmetries in a CFT living in $1+1$ and $2+1$ dimensions.

Besides the QFT interpretation we commented in previous lines, we also managed to relate the phenomenology of t_{rev} and t_{deph} with two QFT systems: a Bose-Einstein condensate of atoms in an optical trap, and the Jaynes-Cummings model, that describes the behavior of a two level atom in a cavity coupled to a quantized radiation.

In **Chapter 5**, we holographically analyzed the out of equilibrium dynamics of a strongly coupled QFT with a **mass gap**, living in an infinite $1+1$ spacetime. The gravity model we used, consisted of an asymptotically AdS_3 spacetime with a **hard**

wall coupled to a massless scalar field.

The presence of a hard wall in this system, allowed us to have a whole new family of theories among which we could move by varying the value of the scalar field at the wall. In the dual theory, this is equivalent to actually **changing the couplings of the QFT** performing a quench. Besides, this new way of quenching allowed us to explicitly see an exchange of energy between the scalar field and the hard wall itself, while the total mass of the system was conserved. This way of quenching "at the wall", corresponds to a new entry of the holographic dictionary for time dependent setups.

To analyze the infrared physics of this holographic system we gave **two definitions**, one for the mass gap, that we defined as the lowest frequency of the normal modes spectrum over a static solution without horizon, and one for the correlation length, that we defined using the HEE as the size of the interval for which the EE saturates. We found both definitions to be consistent as expected.

This holographic setup with a hard wall is specially suited to have **revivals** in the dual QFT. Through the quenches we performed, we qualitatively compared our results to the quench dynamics of the **massive Schwinger model**, triggered by turning on abruptly an uniform background electric field [2]. Using this relation, we proposed the **standing waves** to be dual to coherent states of momentum zero modes of the lowest excitation. More localized structures, which were also compatible with revivals, would correspond in the QFT side to states with an appreciable percentage of finite momentum modes. Besides, we connected the broadness of these profiles to the energy of a typical state in the QFT side.

Conclusiones

En esta tesis, hemos estudiado holográficamente la dinámica de fuera de equilibrio en tres escenarios diferentes de teoría cuántica de campos a acoplo fuerte: por un lado un espacio tiempo compacto en 1+1 y 2+1 dimensiones, y por otro un espacio tiempo infinito con un "mass gap" en 1+1 dimensiones. Con el fin de modelizar estas dinámicas, usamos la correspondencia AdS/CFT dónde, en el lado de gravedad clásica, estudiamos la formación dinámica de un agujero negro en un espacio tiempo asintóticamente AdS con un campo escalar sin masa. Cómo un agujero negro en el lado de gravedad modela un estado térmico en el lado de la teoría cuántica de campos dual, la formación de un agujero negro modelará la dinámica hacia el equilibrio en ésta teoría dual. También analizamos cómo interpretar, desde el lado de la teoría cuántica de campos, la no formación de un agujero negro en estos modelos holográficos. Uno de los principales resultados de esta tesis es el haber encontrado, holográficamente, reconstrucciones de un estado dado en las teorías cuánticas de campos fuertemente acopladas que analizamos.

En el Capítulo 4 nos centramos en el análisis e interpretación de los dos primeros modelos holográficos que acabamos de mencionar. Es decir, en el lado de gravedad analizamos un espacio asintóticamente AdS acoplado a un campo escalar sin masa en 2+1 y 3+1 dimensiones en coordenadas globales. En el lado de la teoría cuántica de campos, esto corresponde a una teoría fuertemente acoplada que vive en un espacio compacto $S^1 \times R$ y $S^2 \times R$, respectivamente.
En el análisis gravitacional de AdS_4 y AdS_3, encontramos comportamientos diferentes entre pulsos anchos y estrechos. Mientras que la evolución de pulsos estrechos estuvo mayoritariamente liderada por el efecto de turbulencia débil, en el caso de pulsos anchos, encontramos que este efecto no era tan importante como la dispersión entre subpulsos, que fue el que finalmente dominó la evolución. Además, un resultado importante de esta tesis, fue el conseguir simular la evolución de estas métricas en AdS_4 después de la primera aparición del horizonte aparente. Este resultado nos permitió observar diferentes patrones de aproximación al equilibrio. Por un lado, los pulsos estrechos sufrieron un proceso de relajación escalonado, que fue desencadenado por el desfase de un subconjunto de grados de libertad. Por otro, en los pulsos anchos este mecanismo apareció desfavorecido y observamos una relajación que involucraba a todo el sistema.
En la interpretación de teoría cuántica de campos de estos resultados, relacionamos

las reconstrucciones parciales de la métrica, llamadas rebotes en el texto, con la existencia de reconstrucciones parciales del estado en la teoría de campos dual. Sorprendentemente, con pulsos estrechos, a muy bajas energías y para algunas partes de la evolución, aunque la teoría de campos dual estuviera fuertemente acoplada, pudimos relacionar el patrón de reconstrucciones del estado con la propagación de entrelazamiento cuántico que Cardy y Calabrese propusieron en [1]. El principal resultado que nos permitió establecer esta relación, fue el encontrar una periodicidad que coincidía con la propuesta por este sencillo modelo de propagación de entrelazamiento cuántico. El observable que calculamos fue la entropía de entrelazamiento holográfica, que analizamos durante toda la evolución de la métrica. En este cálculo, usamos la prescripción holográfica para el cálculo de la EE en espacio-tiempos dependientes del tiempo dada en [41]. Tanto en AdS_3 como en AdS_4, encontramos que, para pulsos estrechos, sin importar la masa, la EE mostraba un comportamiento universal cuando el pulso se encontraba en su primera caída desde la frontera al origen. Además, definimos dos cantidades que nos permitieron describir algunas nuevas características de la evolución. En primer lugar, el tiempo de desfase t_{deph}, que definimos como el tiempo al que el sistema se desfasaba, y, después, el tiempo de reconstrucción t_{rev}, que definimos como el tiempo al que el estado inicial se reconstruía parcialmente. Siempre encontramos, tanto en AdS_3 como en AdS_4, que $t_{deph} \approx \pi/2$. Sin embargo, para t_{rev} el resultado fue muy distinto: mientras que en AdS_4 $2t_{deph} \approx t_{rev}$, en AdS_3 estas dos cantidades eran, en algunos casos tan diferentes, que antes de la reconstrucción del estado observamos la emergencia de un plateau dónde la EE se mantenía constante. Este plateau podía retrasar tanto t_{rev} que $t_{rev} \gg t_{deph}$, causando la aparición de dos escalas diferentes de tiempo. Relacionamos este fenómeno con los diferentes grupos de simetría que una teoría conforme de campos tiene cuando vive en 1+1 y en 2+1 dimensiones.

Además de la interpretación desde la teoría cuántica de campos que hemos comentado en líneas anteriores, también conseguimos relacionar la fenomenología de t_{rev} y t_{deph} con dos sistemas cuánticos: un condensado de Bose-Einstein de átomos en una trampa óptica, y el modelo de Jaynes-Cummings, que describe el comportamiento de un átomo de dos niveles en una cavidad acoplada a radiación cuántica.

En el Capítulo 5, analizamos holográficamente la dinámica de fuera de equilibrio de una teoría cuántica de campos, fuertemente acoplada, con un "mass gap", y viviendo en un espacio tiempo no compacto en 1+1 dimensiones. El modelo de gravedad que usamos, consistió en un espacio tiempo asintóticamente AdS_3, acoplado a un campo

escalar sin masa, y con una pared rígida.
La presencia de esta pared rígida en el sistema, nos permitió disponer de toda una nueva familia de teorías entre las cuales nos movimos variando el valor del campo escalar en la pared. En la teoría cuántica dual, esto es equivalente a cambiar los acoplos de la teoría cuántica de campos realizando lo que se conoce en la literatura como un "quench". Además, esta nueva forma de realizar un "quench" en el sistema, nos permitió ver explícitamente un intercambio de energía entre el campo escalar y la pared rígida, mientras la masa total del sistema permanecía constante. Esta forma de realizar un "quench" en la pared, establece una nueva entrada en el diccionario holográfico en sistemas dependientes del tiempo.
Para analizar la física infrarroja de este sistema holográfico establecimos dos definiciones, una para el "mass gap", que definimos como la frecuencia más baja del espectro de modos normales sobre una solución estática sin horizonte, y otra para la longitud de correlación, que definimos usando la entropía de entrelazamiento holográfica como el tamaño del intervalo para el que la EE satura. Encontramos que ambas definiciones eran consistentes, tal y como esperábamos.
En este sistema holográfico con una pared rígida es especialmente sencillo tener reconstrucciones de estado en la teoría cuántica de campos dual. A través de los "quenches" que realizamos en el sistema, comparamos cualitativamente nuestros resultados con los de la dinámica posterior a diversos "quenches" realizados en el modelo de Schwinger masivo, provocados por encender de forma abrupta un campo eléctrico uniforme [2]. Usando esta relación con el modelo de Schwinger masivo, propusimos que las ondas estacionarias del sistema de gravedad eran duales a estados coherentes con modos de momento cero de la más baja excitación. Estructuras más localizadas, que son también compatibles con reconstrucciones del estado en la teoría dual, corresponderían, en el lado de la teoría cuántica de campos, a estados con un apreciable porcentaje de modos con momento finito. Además, conectamos la anchura de estos perfiles con la energía de un estado típico en la teoría cuántica de campos dual.

Bibliography

[1] P. Calabrese and J. L. Cardy, J. Stat. Mech. **0504**, P04010 (2005) doi:10.1088/1742-5468/2005/04/P04010 [cond-mat/0503393].

[2] B. Buyens, J. Haegeman, K. Van Acoleyen, H. Verschelde and F. Verstraete, Phys. Rev. Lett. **113**, 091601 (2014) doi:10.1103/PhysRevLett.113.091601 [arXiv:1312.6654 [hep-lat]].

[3] J. M. Maldacena, Int. J. Theor. Phys. **38**, 1113 (1999) [Adv. Theor. Math. Phys. **2**, 231 (1998)] doi:10.1023/A:1026654312961 [hep-th/9711200].

[4] E. Fermi, J. Pasta and S. Ulam, May 1955, Document LA-1940.
G. P. Berman and F. M. Izrailev, *The Fermi-Pasta-Ulam problem: Fifty years of progress* Chaos, Volume 15, Issue 1, pp. 015104-015104-18 (2005). arXiv:nlin/0411062

[5] A. Polkovnikov, K. Sengupta, A. Silva and M. Vengalattore, Rev. Mod. Phys. **83**, 863 (2011) doi:10.1103/RevModPhys.83.863 [arXiv:1007.5331 [cond-mat.stat-mech]].

[6] M. Rigol, V. Dunjko, V. Yurovsky and Maxim Olshanii. *Relaxation in a Completely Integrable Many-Body Quantum System: An Ab Initio Study of the Dynamics of the Highly Excited States in 1D Lattice Hard-Core Bosons*, Phys. Rev. Lett. 98, 050405 (2007).

[7] M. Gring, M. Kuhnert, T. Langen, T. Kitazgawa, B. Rauer, M. Schreitl, I. Mazets, D. A. Smith , E. Demler and J. Schmiedmayer, *Relaxation and Prethermalization in an Isolated Quantum System*, Science 337, 1318 (2012); DOI: 10.1126/science.1224953, arXiv:1112.0013.

[8] S. Trotzky, Y. -A. Chen, A. Flesch, I. P Mc Cullough, U. Schollwöck, J. Eisert and I. Bloch, *Probing the relaxation towards equilibrium in an isolated*

strongly correlated one-dimensional Bose gas, Nature Physics 8, 325-330(2012) doi:10.1038/nphys2232, arxiv:1101.2659.

[9] E. Jaynes, Phys. Rev *Information Theory and Statistical Mechanics* **106**, 620, 1957.

[10] M. Kollar, F.A. Wolf and M. Eckstein, *Generalized Gibbs ensemble predicction of prethermalization plateaus and their relation to nonthermal steady states in integrable systems*, Physical Review B **84**, 054304 (2011).

[11] Adu Smith, et. al., *Prethermalization revealed by the relaxation dynamics of full distribution functions*, New Journal of Physics, arXiv 1212.4645.

[12] Giuseppe Mussardo, *Infinite-time Average of Local Fields in an Integrable Quantum Field Theory after a Quench*, arXiv[1308.4551].

[13] R.W. Robinett, *Quantum wave packet revivals*. Physics Reports, 392 (2004) 1-119, doi:10.1016/j.physrep.2003.11.002,

[14] H. Rieger and F. Iglói, *Quantum relaxation after a quench in systems with boundaries*, Phys. Rev. Lett. **106** 035701 (2011);

[15] J. Häppölä, G.B. Halász, A. Hamma, *Revivals of a closed quantum system and Lieb-Robinson speed*, Phys. Rev. A **85**, 032114 (2012).

[16] John Cardy, *Thermalization and Revivals after a Quench in Conformal Field Theory*, [arXiv:1403.3040].

[17] R. Orus, Annals Phys. **349**, 117 (2014) doi:10.1016/j.aop.2014.06.013 [arXiv:1306.2164 [cond-mat.str-el]].

[18] E. Witten, Adv. Theor. Math. Phys. **2**, 253 (1998) [hep-th/9802150].

[19] U. H. Danielsson, E. Keski-Vakkuri and M. Kruczenski, JHEP **0002**, 039 (2000) doi:10.1088/1126-6708/2000/02/039 [hep-th/9912209].

[20] T. Banks, M. R. Douglas, G. T. Horowitz and E. J. Martinec, hep-th/9808016.

[21] J. Abajo-Arrastia, E. da Silva, E. Lopez, J. Mas and A. Serantes, JHEP **1405**, 126 (2014) doi:10.1007/JHEP05(2014)126 [arXiv:1403.2632 [hep-th]].

[22] E. da Silva, E. Lopez, J. Mas and A. Serantes, "Collapse and Revival in Holographic Quenches," JHEP **04** (2015) 038 [arXiv:1412.6002 [hep-th]].

[23] E. da Silva, E. Lopez, J. Mas and A. Serantes, JHEP **1606**, 172 (2016) doi:10.1007/JHEP06(2016)172 [arXiv:1604.08765 [hep-th]].

[24] P. Bizon and A. Rostworowski, Phys. Rev. Lett. **107**, 031102 (2011) doi:10.1103/PhysRevLett.107.031102 [arXiv:1104.3702 [gr-qc]].

[25] J. Jalmuzna, A. Rostworowski and P. Bizon, Phys. Rev. D **84**, 085021 (2011) doi:10.1103/PhysRevD.84.085021 [arXiv:1108.4539 [gr-qc]].

[26] O. J. C. Dias, G. T. Horowitz and J. E. Santos, Class. Quant. Grav. **29**, 194002 (2012) doi:10.1088/0264-9381/29/19/194002 [arXiv:1109.1825 [hep-th]].

[27] D. Garfinkle and L. A. Pando Zayas, Phys. Rev. D **84**, 066006 (2011) doi:10.1103/PhysRevD.84.066006 [arXiv:1106.2339 [hep-th]].

[28] D. Garfinkle, L. A. Pando Zayas and D. Reichmann, JHEP **1202**, 119 (2012) doi:10.1007/JHEP02(2012)119 [arXiv:1110.5823 [hep-th]].

[29] A. Buchel, L. Lehner and S. L. Liebling, Phys. Rev. D **86**, 123011 (2012) doi:10.1103/PhysRevD.86.123011 [arXiv:1210.0890 [gr-qc]].

[30] O. J. C. Dias, G. T. Horowitz, D. Marolf and J. E. Santos, Class. Quant. Grav. **29**, 235019 (2012) doi:10.1088/0264-9381/29/23/235019 [arXiv:1208.5772 [gr-qc]].

[31] M. Maliborski and A. Rostworowski, Phys. Rev. Lett. **111**, 051102 (2013) doi:10.1103/PhysRevLett.111.051102 [arXiv:1303.3186 [gr-qc]].

[32] A. Buchel, S. L. Liebling and L. Lehner, Phys. Rev. D **87**, no. 12, 123006 (2013) doi:10.1103/PhysRevD.87.123006 [arXiv:1304.4166 [gr-qc]].

[33] M. Maliborski and A. Rostworowski, arXiv:1307.2875 [gr-qc].

[34] P. Bizon and J. Jalmuzna, Phys. Rev. Lett. **111**, no. 4, 041102 (2013) doi:10.1103/PhysRevLett.111.041102 [arXiv:1306.0317 [gr-qc]].

[35] B. Craps, E. Kiritsis, C. Rosen, A. Taliotis, J. Vanhoof and H. b. Zhang, JHEP **1402**, 120 (2014) doi:10.1007/JHEP02(2014)120 [arXiv:1311.7560 [hep-th]].

[36] B. Craps, E. J. Lindgren, A. Taliotis, J. Vanhoof and H. b. Zhang, Phys. Rev. D **90**, no. 8, 086004 (2014) doi:10.1103/PhysRevD.90.086004 [arXiv:1406.1454 [hep-th]].

[37] S. Ryu and T. Takayanagi, Phys. Rev. Lett. **96**, 181602 (2006) doi:10.1103/PhysRevLett.96.181602 [hep-th/0603001].

[38] H. Casini, M. Huerta and R. C. Myers, JHEP **1105**, 036 (2011) doi:10.1007/JHEP05(2011)036 [arXiv:1102.0440 [hep-th]].

[39] A. Lewkowycz and J. Maldacena, JHEP **1308**, 090 (2013) doi:10.1007/JHEP08(2013)090 [arXiv:1304.4926 [hep-th]].

[40] X. Dong, A. Lewkowycz and M. Rangamani, JHEP **1611**, 028 (2016) doi:10.1007/JHEP11(2016)028 [arXiv:1607.07506 [hep-th]].

[41] V. E. Hubeny, M. Rangamani and T. Takayanagi, JHEP **0707**, 062 (2007) doi:10.1088/1126-6708/2007/07/062 [arXiv:0705.0016 [hep-th]].

[42] A. M. Polyakov, Nucl. Phys. Proc. Suppl. **68**, 1 (1998) doi:10.1016/S0920-5632(98)00135-2 [hep-th/9711002].

[43] A. M. Polyakov, Int. J. Mod. Phys. A **14**, 645 (1999) doi:10.1142/S0217751X99000324 [hep-th/9809057].

[44] S. S. Gubser, I. R. Klebanov and A. M. Polyakov, Phys. Lett. B **428**, 105 (1998) doi:10.1016/S0370-2693(98)00377-3 [hep-th/9802109].

[45] O. Aharony, S. S. Gubser, J. M. Maldacena, H. Ooguri and Y. Oz, Phys. Rept. **323**, 183 (2000) doi:10.1016/S0370-1573(99)00083-6 [hep-th/9905111].

[46] E. Witten, Adv. Theor. Math. Phys. **2**, 505 (1998) [hep-th/9803131].

[47] Christos Charmousis, "Introduction to Anti de Sitter black holes", Springer Berlin Heidelberg.

[48] S. W. Hawking and D. N. Page, Commun. Math. Phys. **87**, 577 (1983). doi:10.1007/BF01208266

[49] P. Zhao, "Black Holes in Anti de Sitter Spacetime".

[50] E. Fradkin, "Field Theories of Condensed Matter Physics," Addison-Wesley Pulishing Company. Second Edition. (2013)

[51] S. Ryu and T. Takayanagi, JHEP **0608**, 045 (2006) doi:10.1088/1126-6708/2006/08/045 [hep-th/0605073].

[52] T. Nishioka, S. Ryu and T. Takayanagi, J. Phys. A **42**, 504008 (2009) doi:10.1088/1751-8113/42/50/504008 [arXiv:0905.0932 [hep-th]].

[53] C. Holzhey, F. Larsen and F. Wilczek, Nucl. Phys. B **424**, 443 (1994) doi:10.1016/0550-3213(94)90402-2 [hep-th/9403108].

[54] G. Vidal, J. I. Latorre, E. Rico and A. Kitaev, Phys. Rev. Lett. **90**, 227902 (2003) doi:10.1103/PhysRevLett.90.227902 [quant-ph/0211074].

[55] J. I. Latorre, E. Rico and G. Vidal, Quant. Inf. Comput. **4**, 48 (2004) [quant-ph/0304098].

[56] P. Calabrese and J. L. Cardy, J. Stat. Mech. **0406**, P06002 (2004) doi:10.1088/1742-5468/2004/06/P06002 [hep-th/0405152].

[57] P. Calabrese and J. Cardy, J. Phys. A **42**, 504005 (2009) doi:10.1088/1751-8113/42/50/504005 [arXiv:0905.4013 [cond-mat.stat-mech]].

[58] P. Calabrese and J. Cardy, J. Stat. Mech. **0706**, P06008 (2007) doi:10.1088/1742-5468/2007/06/P06008 [arXiv:0704.1880 [cond-mat.stat-mech]].

[59] C. T. Asplund, A. Bernamonti, F. Galli and T. Hartman, JHEP **1509**, 110 (2015) doi:10.1007/JHEP09(2015)110 [arXiv:1506.03772 [hep-th]].

[60] T. Takayanagi and T. Ugajin, JHEP **1011**, 054 (2010) doi:10.1007/JHEP11(2010)054 [arXiv:1008.3439 [hep-th]].

[61] J. Abajo-Arrastia, J. Aparicio and E. Lopez, JHEP **1011**, 149 (2010) doi:10.1007/JHEP11(2010)149 [arXiv:1006.4090 [hep-th]].

[62] D. Christodoulou and S. Klainerman, Princeton University Press, Princeton, 1993

[63] H. Friedrich, Commun.Math.Phys., 107, 587-609, 1986

[64] J. D. Brown and M. Henneaux, Commun. Math. Phys. **104**, 207 (1986). doi:10.1007/BF01211590

[65] V.I. Yudovihc, *On the loss of smoothness of the solutions of Euler's equations with time* (Russian), Dinamika Sploshn. Sredy 16, 71 (1974).

[66] M. Banados, C. Teitelboim and J. Zanelli, Phys. Rev. Lett. **69**, 1849 (1992) doi:10.1103/PhysRevLett.69.1849 [hep-th/9204099].

[67] V. Balasubramanian *et al.*, Phys. Rev. Lett. **106**, 191601 (2011) doi:10.1103/PhysRevLett.106.191601 [arXiv:1012.4753 [hep-th]].

[68] T. Albash and C. V. Johnson, New J. Phys. **13**, 045017 (2011) doi:10.1088/1367-2630/13/4/045017 [arXiv:1008.3027 [hep-th]].

[69] V. Balasubramanian *et al.*, Phys. Rev. D **84**, 026010 (2011) doi:10.1103/PhysRevD.84.026010 [arXiv:1103.2683 [hep-th]].

[70] M. Nozaki, T. Numasawa and T. Takayanagi, JHEP **1305**, 080 (2013) doi:10.1007/JHEP05(2013)080 [arXiv:1302.5703 [hep-th]].

[71] C. V. Johnson, JHEP **1403**, 047 (2014) doi:10.1007/JHEP03(2014)047 [arXiv:1306.4955 [hep-th]].

[72] M. Greiner, O.Mandel, T.W. Hänsh and I. Bloch, *Collapse and revival of the matter wave field of a Bose-Einstein condensate* Nature **419**, 51 (2002).

[73] E. T. Jaynes and F. W. Cummings, IEEE Proc. **51**, 89 (1963). doi:10.1109/PROC.1963.1664

[74] D. V. Fursaev, JHEP **0609**, 018 (2006) doi:10.1088/1126-6708/2006/09/018 [hep-th/0606184].

[75] M. C. Bauls, K. Cichy, K. Jansen and J. I. Cirac, JHEP **1311**, 158 (2013) doi:10.1007/JHEP11(2013)158 [arXiv:1305.3765 [hep-lat]].

[76] E. Rico, T. Pichler, M. Dalmonte, P. Zoller and S. Montangero, Phys. Rev. Lett. **112**, 201601 (2014) doi:10.1103/PhysRevLett.112.201601 [arXiv:1312.3127 [cond-mat.quant-gas]].

[77] T. Pichler, M. Dalmonte, E. Rico, P. Zoller and S. Montangero, Phys. Rev. X **6**, no. 1, 011023 (2016) doi:10.1103/PhysRevX.6.011023 [arXiv:1505.04440 [cond-mat.quant-gas]].

[78] B. Buyens, J. Haegeman, F. Hebenstreit, F. Verstraete and K. Van Acoleyen, arXiv:1612.00739 [hep-lat].

[79] A. Buchel, R. C. Myers and A. van Niekerk, Phys. Rev. Lett. **111**, 201602 (2013) doi:10.1103/PhysRevLett.111.201602 [arXiv:1307.4740 [hep-th]].

[80] S. R. Das, D. A. Galante and R. C. Myers, Phys. Rev. Lett. **112**, 171601 (2014) doi:10.1103/PhysRevLett.112.171601 [arXiv:1401.0560 [hep-th]].

[81] S. R. Das, D. A. Galante and R. C. Myers, JHEP **1502**, 167 (2015) doi:10.1007/JHEP02(2015)167 [arXiv:1411.7710 [hep-th]].

[82] S. R. Das, D. A. Galante and R. C. Myers, JHEP **1508**, 073 (2015) doi:10.1007/JHEP08(2015)073 [arXiv:1505.05224 [hep-th]].